Max-Planck-Institut für Intelligente Systeme
(ehemals Max-Planck-Institut für Metallforschung)
Stuttgart

Thermodynamics and kinetics of the oxidation of amorphous Al-Zr alloys

Katharina Weller

Dissertation
an der
Universität Stuttgart

Bericht Nr. 254
November 2015

Thermodynamics and kinetics of the oxidation of amorphous Al-Zr alloys

Von der Fakultät Chemie der Universität Stuttgart zur Erlangung der
Würde eines Doktors der Naturwissenschaft (Dr. rer. nat.)
genehmigte Abhandlung

vorgelegt von
Katharina Weller
aus Backnang

Hauptberichter:	Prof. Dr. Ir. E. J. Mittemeijer
Mitberichter:	Prof. Dr. J. Bill
Prüfungsvorsitzender:	Prof. Dr. T. Schleid

Tag der Einreichung:	14.10.2015
Tag der mündlichen Prüfung:	25.11.2015

MAX-PLANCK-INSTITUT FÜR INTELLIGENTE SYSTEME, STUTTGART
(EHEMALS MAX-PLANCK-INSTITUT FÜR METALLFORSCHUNG)
INSTITUT FÜR MATERIALWISSENSCHAFT DER UNIVERSITÄT STUTTGART

2015

Contents

Chapter 1

Introduction

1.1 General background

Many surface-related properties of a metallic material are directly linked to the surficial oxide film, which inevitably forms in contact with an oxidizing gaseous or liquid environment. Hence tailoring of the microstructure of oxide films on metallic materials (e.g. the thickness, morphology, composition and defect structure [1]) by controlled variation of the oxidation conditions (e.g. oxidation temperature, oxygen partial pressure and oxidation time) is essential for adapting functional properties, such as the corrosion resistance, adhesion, electrical conductivity and thermal stability. Accordingly, a profound knowledge of the interrelationship of oxidation conditions and the oxidation behavior of a metallic material is required for optimizing specific material (surface) properties, as well as to assess the reactivity, durability and reliability of respective technological components during operation under real-life conditions (e.g. in liquids, in reactive gasses and/or under thermal or mechanical loading conditions at elevated temperatures). The oxidation behavior of a metallic material, and more specifically the microstructural evolution of the growing oxide film, can be influenced directly by alloying with specific elements [2, 3]. *Crystalline* metallic alloys usually form either solid solution alloys or specific intermetallic compounds over well-defined, relatively narrow, compositional ranges, as predicted by bulk thermodynamics and as displayed in a bulk phase diagram. Thus the possibilities to tailor the oxidation behavior and thereby the oxide properties by selective variation of *only* the alloy composition (i.e. without subsequent variation of the alloy microstructure) are generally severely limited for crystalline alloys. *Amorphous* alloys (or metallic glasses), on the other hand, can typically be prepared over a relatively wide compositional range, while fully preserving the amorphous state. Moreover, since grain boundaries are naturally absent in amorphous solids, the oxidation of amorphous alloys is expected to result in a compositionally and structurally much more homogenous (amorphous) surface oxide layer as compared to the respective (crystalline) oxide layers grown on crystalline alloys. Such compositionally and structurally homogenous amorphous oxide films are expected to exhibit superior properties, such as improved oxidation and corrosion resistance [4-6].

The binary alloy system Al-Zr exhibits excellent glass forming ability over a wide compositional range ($0.29 \leq x_{\mathrm{Al}} \leq 0.83$) [7], as well as a high thermal stability [8]; it thus represents an ideal model system for a systematic study of the sole effect of the alloy composition on the oxidation and corrosion behaviors of (amorphous) alloys.

1.2 Focus of this thesis

This thesis presents a systematic and comprehensive investigation of the thermal oxidation of amorphous $\mathrm{Al}_x\mathrm{Zr}_{1-x}$ (am-$\mathrm{Al}_x\mathrm{Zr}_{1-x}$) alloys over a wide compositional range under varying oxidation conditions (e.g. oxidation temperature, oxidation time). It comprises the investigation of the developing oxide phases, the oxide microstructure, the oxidation kinetics and the corrosion behavior of the alloys as function of the oxidation conditions.

To this end, 2 µm-thick am-$\mathrm{Al}_x\mathrm{Zr}_{1-x}$ coatings in a composition range of $0.26 \leq x \leq 0.75$ were prepared by magnetron-co-sputtering on 50 nm am-SiO_2/50 nm am-$\mathrm{Si}_3\mathrm{N}_4$/Si wafers and subsequently oxidized in a temperature range of T = 350 °C – 560 °C at $p_{\mathrm{O2}} = 10^5$ Pa for up to 10 h. The microstructural evolutions of the parent am-$\mathrm{Al}_x\mathrm{Zr}_{1-x}$ alloy and the oxide overlayer, as formed during thermal oxidation, were characterized by means of X-ray diffraction (XRD), cross-sectional (analytical) transmission electron microscopy (TEM), Auger electron spectroscopy (AES) depth profiling, X-ray photoelectron spectroscopy (XPS) and ex-situ spectroscopic ellipsometry (SE).

The experimentally-observed changes in the microstructure and composition of the developing oxide phases as function of the oxidation conditions are discussed from both thermodynamic and kinetic points of view and are rationalized by thermodynamic model calculations exposing the dominating role of thermodynamics in controlling the oxide phase composition, even for amorphous oxide overgrowths.

Furthermore, the oxidation kinetics of amorphous $\mathrm{Al}_x\mathrm{Zr}_{1-x}$ alloys were investigated as function of the alloy composition ($0.26 \leq x \leq 0.68$) and the oxidation temperature (350 °C ≤ T ≤ 400 °C) at a constant oxygen pressure ($p_{\mathrm{O2}} = 1\times10^5$ Pa). In order to elucidate the underlying oxidation mechanism, the oxidation-induced compositional changes in the parent alloy adjacent to the oxide/alloy interface were investigated by AES depth profiling analyses.

Finally, with respect to the practical application of oxide layers, it has been investigated whether the controlled pre-oxidation treatment of the am-Al_xZr_{1-x} alloys as done in this work offers a promising route for the development of a new generation of corrosion-resistant coating systems based on pre-oxidized amorphous alloys. To this end, the electrochemical behavior of untreated and pre-oxidized am-Al_xZr_{1-x} alloy coatings was investigated by employing an electrochemical microcapillary technique.

1.3 Background

1.3.1 Amorphous alloys

Due to their compositional homogeneity and absence of long-range order, amorphous metallic alloys show unique properties, such as pronounced resistance against oxidation and corrosion [4-6] and favorable mechanical and electronic properties (see [9, 10] and references therein), as compared to their crystalline counterparts. Hence amorphous metallic alloys have been investigated as promising candidates for e.g. biomedical materials, such as biodegradable implants made of Mg-based BMG, which show good biocompatibility and possess high mechanical strength and elasticity in comparison to crystalline Mg-based alloys [11]. Especially the family of Zr-based amorphous metallic alloys have attracted much interest, since they possess a high thermal stability, high strength, high ductility, low coefficient of thermal expansion and a good corrosion resistance [12]. For example, amorphous Zr-Al-Ni-Cu alloys find applications as pressure sensors with a high pressure endurance for automobiles or micro-geared motor parts with high torque for cellphones (see [13] and references therein).

Since the discovery of the first amorphous alloy (metallic glass) in the Au-Si system, prepared by a rapid quenching technique in 1959 [14], many more alloy systems capable to form an amorphous structure (i.e. without a long-range atomic order) have been discovered (see [15] and references therein). Traditionally, to obtain an amorphous structure high cooling rates were required. Hence, it was only possible to fabricate amorphous alloys in very small dimensional structures which allow a fast heat extraction [4], such as thin ribbons, wires and filaments. This severely constrained the possible fields of application of amorphous metallic materials. With time, special multi-component systems with high glass-forming ability, which require lower critical cooling rates, were discovered. The following development of so-called bulk metallic glasses (BMG) in centimeter-scale dimensions represents a milestone in the research of amorphous metallic alloys (see [13] and references therein). Since then, possible fields of application of amorphous metallic alloys rapidly expanded.

However, for some alloy systems it is either impossible at all to achieve the amorphous state by rapid quenching from the melt, or only possible in special concentration ranges, e.g. near the eutectics, due to the fact that a sufficient/critical cooling rate is required. This is especially the case for metallic alloy systems in which the alloy components have considerably different melting temperatures, as it is the case for e.g. Al (T_m = 660.4 °C [16]) and Zr (1852.0 °C [16]), or when the components are immiscible in their liquid state. For these alloy systems alternative processing routes, which involve higher effective cooling rates and/or do not require melting for alloy formation, have to be applied to obtain an amorphous structure [17]. Such alternative routes include, for example, atomic/molecular deposition techniques (chemical or physical vapor deposition such as magnetron sputtering) or external action techniques (e.g. ion beam mixing, ion implantation) [4]. With these techniques it is possible to obtain amorphous single phases over a wide composition range and even to expand the possible range of glass-forming alloy systems. For details of the formation of amorphous Al-Zr alloys, see Section 1.3.4.1.

1.3.2 Oxidation

1.3.2.1 Oxide phase formation

The fundamental understanding of the oxidation behavior of metals and alloys is of great scientific and technological interest, because the surficial oxide layer formation may lead to many improved materials properties which find numerous application in state-of-the-art technologies, such as in microelectronics with attractive electrical properties [18-20], protective coatings against corrosion processes [21, 22] or as gas sensors [23, 24]. While oxidation of crystalline metallic materials has been investigated for decades, the oxidation behavior of amorphous metals, which represent a relatively young class of materials, remains largely unknown.

Upon oxidation of a metallic element (Me), the thermodynamic driving force for the oxidation reaction,

$$x\cdot\mathrm{Me(s)} + y/2\cdot\mathrm{O_2(g)} \rightleftarrows \mathrm{Me}_x\mathrm{O}_y\mathrm{(s)},$$

is provided by the change in chemical Gibbs energy associated with the formation of the oxide phase(s). For most metals the Gibbs energy change of the corresponding oxidation reaction is strongly negative and thus a (native) oxide layer forms inevitably on top of a metallic material in contact with an oxidizing atmosphere. In first approximation, the chemical Gibbs energy of formation for given temperature and pressure conditions is decisive for which oxide phase is formed. However, not only bulk thermodynamics, but also surface and interface energies can play a crucial role in oxide formation behavior. For instance, during initial oxidation, a very thin amorphous oxide layer can be more stable up to a critical thickness than its crystalline counterpart due to their relatively low interface energy with the crystalline parental alloy or the ambient, which compensates the higher bulk Gibbs energy of the amorphous oxide, as it is the case for the oxidation of e.g. Al crystals [25] and Zr crystals [26].

In comparison to pure metals, metallic alloys generally undergo much more complex oxidation behaviors, since they may contain more than one oxidizable constituent [27]. Thus, several different oxide phases, with more or less extended solubility ranges (e.g. binary, ternary or multinary oxides), can be in thermodynamic equilibrium. Moreover, upon ongoing oxidation, the composition of the metallic substrate (and thus also the solubility of oxygen therein) can be changed by the preferential oxidation of specific components. This oxidation-induced compositional change of the substrate can induce formation of (inter-)metallic phases, or stabilization of different oxide phases during oxidation. The oxidation behavior is further complicated by kinetics, e.g. by the different mobilities of reacting species in the oxide or the alloy phase, which can favor or impede formation of certain oxide phases [27, 28]. All the before mentioned factors can influence and govern the oxide phase formation, microstructure and composition, upon thermal oxidation of metallic alloys.

The analysis of the oxidation behavior can be even more complex if the parental alloy has an amorphous structure, since the oxide phase formation in case of an amorphous alloy – which is a thermodynamically metastable state – cannot be described using classical bulk thermodynamics. Hence, a prediction of the oxidation behavior of amorphous alloys according to bulk thermodynamics is difficult. It is further emphasized that, due to the amorphous state of the parent alloy, growth stresses in the developing oxide overlayer due to lattice mismatch strain, and interfacial energies will differ from the case of oxide formation on the crystalline alloy counterpart of the parent alloy (and will probably be less influential) [26].

1.3.2.2 Kinetics of oxidation

Although the presence of a chemical driving force is a prerequisite for oxide formation, it contains no information about the kinetics of oxide formation, which is dependent on the reaction mechanism at the gas/oxide and/or the oxide/metal interface and the migration rate of ions/atoms/electrons across the oxide scale. To understand the oxidation reaction kinetics a closer consideration of the oxidation processes is given below.

The generally fast initial oxidation of a metal or alloy surface in contact with an oxidizing atmosphere begins with the physisorption of oxygen molecules on the metal surface and the dissociation of the adsorbed molecules (chemisorption), followed by oxide nucleation and growth to form a laterally-closed oxide film. This laterally-closed oxide film then constitutes a diffusion barrier separating the oxidizing atmosphere and the metal/alloy substrate. Further oxidation, i.e. growth of the oxide film, can only proceed by the migration of (charged) reactant species (i.e. cations, anions, electrons, holes and vacancies) through the 'barrier' oxide film [28, 29]. In Figure 1.1 a schematic illustration of an oxidation process is given.

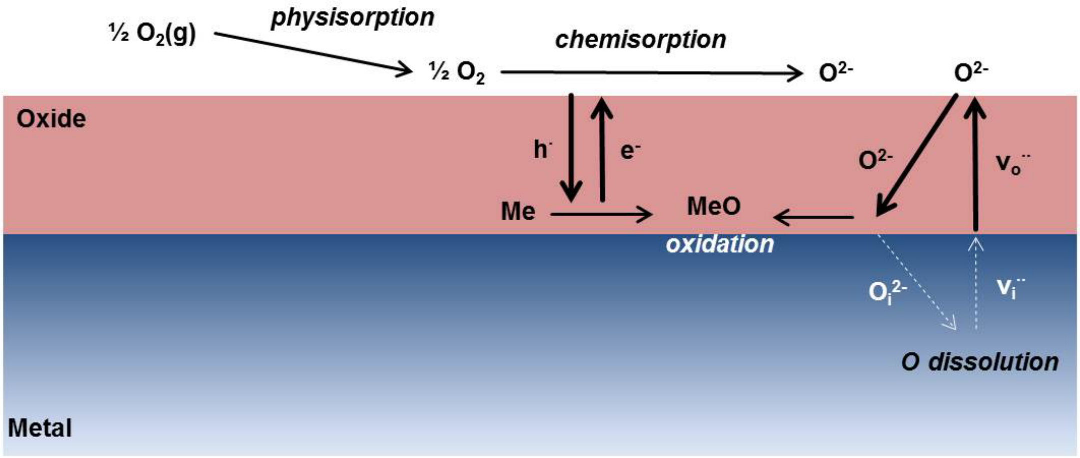

Figure 1.1: Schematic illustration of an oxidation process of a metallic material with high oxygen dissolution. The oxidation reaction takes place by inward diffusion of oxygen towards the reacting oxide/metallic material interface.

According to Wagner's theory of oxidation [28, 30], the oxide-film growth rate of an oxide scale at high oxidation temperatures is governed by the thermally-activated diffusional processes of reactant species across the growing oxide scale. Thereby opposing fluxes of metal ions and oxygen ions are established across the oxide scale as induced by chemical potential gradients, which are a result of thermodynamic equilibrium assumed to prevail both at the oxide/atmosphere and oxide/metal interfaces. The electric field built up by the charged ions migrating across the oxide scale, induces a transport of electrons across the oxide scale to maintain electroneutrality throughout the oxide scale [28, 30]. Hence the resulting oxide film growth kinetics is governed by the slowest-moving reactant species through the oxide film as it is the rate-limiting step for the oxidation process [28, 30].

1.3.3 Electrochemical behavior of amorphous alloys

The corrosion behavior of amorphous alloys is of peculiar interest since amorphous alloys can have superior corrosion resistance as compared to their crystalline counterparts. Unlike crystalline materials, amorphous alloys possess no lattice defects (e.g. grain boundaries, kinks, dislocations or stacking faults) or second-phase particles at which corrosion often preferentially occurs. Thus the improved corrosion resistance found in some amorphous alloys is often attributed to their structural and chemical homogeneity [4, 6, 31]. Also the ability of amorphous alloys to rapidly form a passive amorphous oxide film with minimized defect structure (e.g. no grain boundaries) can be responsible for an improved corrosion behavior by retarding the ionic movement through the passive film. Moreover the flexible bonding configurations in amorphous oxide might compensate lattice mismatch or strain between oxide and metal. Consequently, the film ductility and bond flexibility might lead to a highly protective passive film, which is more stable against cracking by stress. Furthermore, amorphous alloys have the ability to form a supersaturated solid solution in comparison to its crystalline counterpart (by exceeding equilibrium solubility). Hence alloying with a more corrosion resistant element can improve the corrosion behavior of the solid solution by incorporation into the (amorphous) oxide film or by retarding the dissolution rates of the underlying metallic substrate [4, 6, 31].

Al metal, for example, provides good corrosion resistance in neutral environments, due to the fact that Al is covered naturally with a stable continuous and uniform amorphous oxide layer which provides passivity. In acidic and basic solutions, however, Al metal actively dissolves (cf. the Pourbaix diagram in Figure 1.2) and is also very susceptible to pitting corrosion in chloride-containing solutions [32, 33]. By alloying with a transition metal (TM) like W, Ta, Mo Nb, Cr or Zr, the corrosion resistance of Al-based alloys in corrosive environments can be greatly improved due to the formation of a structurally and compositionally uniform, passivating amorphous (oxyhydr-)oxide film which contains cations of both the aluminum and the corrosion-resistant element [17].

According to the Graph-theory, which describes the corrosion behavior of binary alloys, a critical minimum concentration of the TM alloying element in the (oxyhydr-)oxide film is required to induce passivity. Thereby a continuous network of –TM-O(H)-TM- bridges establishes in the oxide film which is more stable than –Al-O(H)-Al- bridges in an aqueous solution and thereby improve the corrosion resistance by impede the transport of ions and defects through the passive film [34].

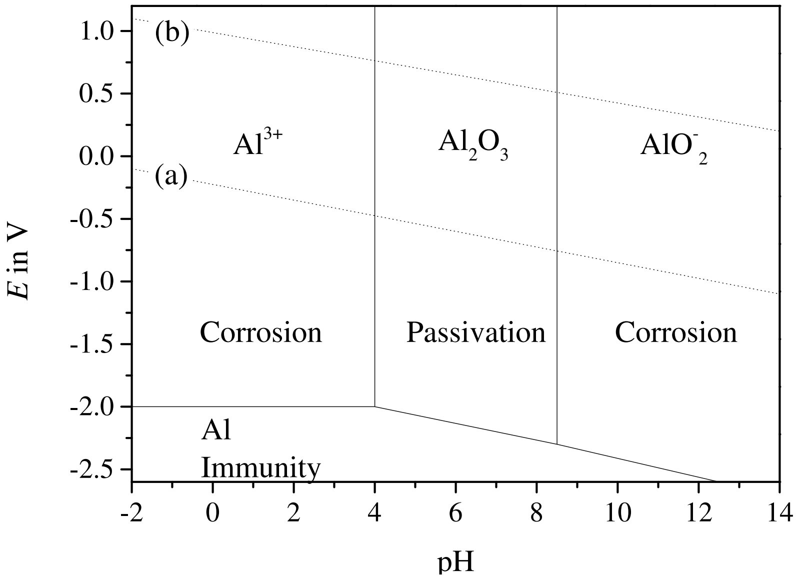

Figure 1.2: Pourbaix diagram (potential (*E*) – pH) of aluminum (adopted from Refs. [35, 36]).

1.3.4 The Al-Zr binary alloy system

Up to date, Al-Zr alloys have been used as hydrogen getter materials in vacuum systems [37-39]. Al-Zr alloys are also considered as potential candidates as fuel-element-cladding material in the nuclear industry, since Al-Zr alloys have low absorption cross sections for thermal neutrons [37]. Since corrosion damage in nuclear reactors occurs primarily by hydrogen and oxygen diffusion through grain boundaries, the high glass forming ability of the Al-Zr system to form an amorphous alloy, which can provide improved corrosion resistance due to its structural and chemical homogeneity (i.e. without grain boundaries), is of additional interest [40, 41].

Further, the oxidation of (amorphous) Al-Zr alloys to form an amorphous ZrO_2-Al_2O_3 phase has attracted interest in recent years, since amorphous oxides are promising candidates as high-*k* materials, because they have a uniform dielectric constant *k* and possess no grain boundaries serving as electric leakage paths [42]. The ZrO_2-Al_2O_3 binary system shows structural stability of the amorphous ZrO_2-Al_2O_3 phase at high temperatures, which makes it a promising material as high-*k* dielectric material [43].

1.3.4.1 Preparation of amorphous Al-Zr alloys

The binary alloy system Al-Zr is characterized by an excellent glass forming ability over a wide composition range. The preparation of amorphous Al-Zr alloys can be achieved by various techniques, such as mechanical alloying (e.g. ball milling) [44-46], ion beam mixing [47] and magnetron sputtering [7, 40, 48, 49]. Even the preparation of amorphous Al-Zr alloys by rapid quenching of Al-Zr melt was reported by Gudzenko in 1974 [50]. In this case amorphous Al-Zr alloys were achieved only in special concentration ranges near the eutectics (45 – 53 at.-% Zr, 63 - 74 at.-% Zr), whereas amorphous Al-Zr thin films formed by sputtering can be achieved over a wide concentration range from 17 to 71 at.-% Zr [7].

1.3.4.2 Oxidation of amorphous Al-Zr alloys

Hitherto, the oxidation behavior and oxidation mechanism of Zr-based multi-component bulk amorphous alloys has been well investigated [3, 5, 51-53], whereas the oxidation behavior of the binary amorphous Al-Zr system has received much less attention. Consequently, a thorough understanding of the oxidation mechanisms of amorphous Al-Zr alloys is lacking.

According to bulk thermodynamics, the pseudo-binary phase diagram of $AlO_{1.5}$ – ZrO_2 (Figure 1.3) doesn’t show the existence of any *crystalline* ternary oxide phase, but only the existence of crystalline binary oxide phases (Al_2O_3 and ZrO_2, each in different modifications) [54, 55]. Depending on the conditions, several modifications of Al_2O_3 and ZrO_2 exist. ZrO_2 possesses three crystalline polymorphs: monoclinic (α-)ZrO_2 (< 1173 °C), tetragonal (β-)ZrO_2 (1173 °C – 2370 °C) and cubic (γ-)ZrO_2 (2370 °C - 2690 °C) [56]. For Al_2O_3, rhombohedral α-Al_2O_3 and metastable cubic γ-Al_2O_3 are the most important polymorphs [57].

Generally, in binary alloy systems, the oxidation behavior can be predicted more easily if one of the constituting elements is much nobler than the other, e.g. for the system Ni-Pt [58]. However, the Gibbs energy of oxide formation per one mole oxygen of all (possibly forming) crystalline binary Al and Zr oxide phases is very similar indicating that both elements, participating in the oxidation reaction, show a similar high affinity towards oxygen. Consequently, a prediction of the sequence of oxide phase nucleation and growth upon thermal oxidation of (amorphous) Al-Zr alloys that is solely based on the comparison of the values of Gibbs energy of oxide formation of the competing oxide phases is often oversimplified. In the case that the equilibrium binary crystalline Al and Zr oxide phases form simultaneously upon oxidation of (amorphous) Al-Zr a phase separation is expected since the pseudo-binary phase diagram of $AlO_{1.5}$ – ZrO_2 shows no mutual solubility of the equilibrium binary crystalline oxide phases at room temperature and up to the eutectic point at 1130 °C [55].

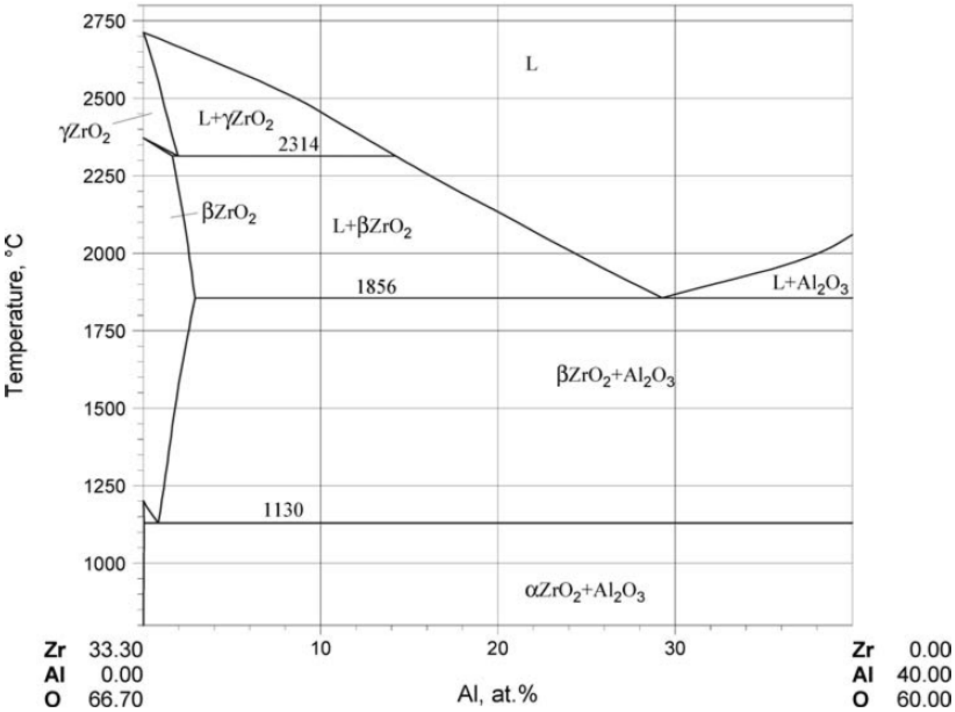

Figure 1.3: Pseudo-binary phase diagram ZrO_2-$AlO_{1.5}$ as taken from Ref. [54].

Hitherto, the oxidation behavior of amorphous Al-Zr alloys has only scarcely been investigated [48]. For example, Soroka *et al*. [48] investigated the structural stability and oxidation resistance of amorphous Al-Zr alloy layers. At elevated oxidation temperatures (up to 700 °C) the amorphous Al-Zr layer of only 150 nm thick fully transformed into an amorphous oxide layer. However, a detailed investigation of the oxide composition, the oxidation-induced changes in the substrate layer, the oxidation mechanism and the oxide-film growth kinetics has not been performed. Clearly such a process (oxidation of 150 nm thin amorphous Al-Zr) is not representative of the oxidation behavior of bulk amorphous Al-Zr alloys (as addressed in the present thesis).

1.3.4.3 Electrochemical behavior of amorphous Al-Zr alloys

As already introduced in Section 1.3.3, the alloying of Al with a more corrosion-resistant element, like Zr, can lead to an improved corrosion resistance. The investigation of the corrosion resistance of amorphous Al-Zr alloys, covered initially with an amorphous native oxide layer, was observed to improve with increasing Zr content in both the alloy and in the passive (Al,Zr)-(oxyhydr)oxide film, formed upon anodization [6, 7, 17, 59, 60]. Certainly, the ability of the amorphous alloy, to be structurally and chemically homogeneous, plays a key role in improved materials corrosion behavior [52]. However, it is generally acknowledged that not only the homogenous amorphous state of the *alloy* promotes superior corrosion behavior, but its ability to form an amorphous *oxide* overgrowth also plays an important role [61]. The am-$Al_{1-x}Zr_x$ alloy system allows the formation of a relatively thick amorphous (Al,Zr)-oxide overlayer by thermal oxidation under selected oxidation conditions, as compared to the only-few-nanometer-thick native amorphous (Al,Zr)-oxide films formed on the as-deposited am-$Al_{1-x}Zr_x$ alloys (covered with a native oxide layer).

1.4 Experimental approach

A prerequisite for a thorough investigation of the thermal oxidation behavior and the underlying oxidation mechanisms of (amorphous) alloys is the application of various experimental approaches combining microstructural and compositional characterization techniques with the analysis of the oxide-film growth kinetics. Thus, in the present thesis, a combined experimental approach by XRD, XPS, AES, cross-sectional (analytic) TEM and SE has been applied for the investigation of the oxidation behavior of amorphous Al-Zr alloys under defined oxidation conditions. Furthermore, the corrosion behavior of as-deposited and oxidized am-Al-Zr alloys has been investigated by the electrochemical microcapillary technique.

1.4.1 Oxidation procedure of am-Al_xZr_{1-x}

Oxidation of sputter-deposited am-Al_xZr_{1-x} specimens (x = 0.26, 0.35, 0.44, 0.51 and 0.68) was performed in quartz ampoules at oxidation temperatures T_{ox} in the range of 350 °C – 560 °C for up to 10 h under a constant oxygen pressure of $p_{O_2} = 1 \times 10^5$ Pa. In order to obtain an oxygen pressure of $p_{O_2} = 1 \times 10^5$ Pa at e.g. the oxidation temperature T_{ox} = 350 °C, the evacuated quartz ampoules were filled at room temperature (RT) with pure oxygen gas of $p_{O_2} = 4.70 \times 10^4$ Pa, which corresponds to $p_{O_2} = 1 \times 10^5$ Pa at T_{ox} = 350 °C. Analogously, quartz ampoules were prepared for various oxidation temperatures. The specimens were either enclosed separately in quartz ampoules or, when it is necessary to compare the oxidation behavior of the amorphous alloys of various alloy compositions, a special construction in each quartz ampoule is employed, which holds a set of specimens of all different compositions to ensure identical oxidation conditions (Figure 1.4). Oxidation of the specimen(s) in such-prepared quartz ampoules was performed isothermally at different T_{ox} for different oxidation times t_{ox}. After the oxidation, the quartz ampoules were immediately quenched in water (T ~ 18 °C), which promptly terminated the thermal oxidation process.

Figure 1.4: Special construction enabling the oxidation of a set of am-Al_xZr_{1-x} specimens with various alloy compositions under identical oxidation conditions.

1.4.2 Structural and compositional characterization

The development of the microstructure of the evolving alloy-substrate/oxide-film system during thermal oxidation of am-Al_xZr_{1-x} alloys was investigated by XRD, cross-sectional (analytical) TEM, AES and XPS.

X-ray diffraction is a powerful non-destructive method to characterize the phase and microstructural evolution of a material. In this study, X-ray diffraction (XRD) analysis was applied to investigate the microstructure of the as-deposited am-Al_xZr_{1-x} alloy specimens and to monitor the evolution of crystalline (oxide or intermetallic) phases upon oxidation of am-Al_xZr_{1-x} specimens.

In this study, cross-sectional TEM analysis was applied to determine the microstructure of oxidized am-Al_xZr_{1-x} alloys. To this end, cross-sectional TEM lamellae were prepared from as-deposited and oxidized am-Al_xZr_{1-x} alloy specimens by the Tripod polishing technique [62] and investigated by TEM. The elemental distribution in the oxidized am-Al_xZr_{1-x} alloy specimens were investigated by energy-filtered TEM (EFTEM) imaging and electron energy loss spectroscopy (EELS) elemental mapping.

AES and XPS analyses [63] were used to obtain a qualitative and quantitative description of the chemical constitution of the (oxidized) am-Al_xZr_{1-x} alloy specimens. By performing alternating cycles of AES/XPS analysis and ion sputtering, a depth-resolved elemental distribution was determined.

1.4.3 Oxide-film growth kinetics by spectroscopic ellipsometry

The principle of ellipsometry was first introduced by Drude in 1887, but only became popular in the 1970’s when the first complete automation of spectroscopic ellipsometry measurements has been realized [64-66]. Ellipsometry allows the non-destructive determination of e.g. optical constants and thin-film thicknesses by measuring the change of the state of polarization of a linearly polarized light beam upon reflection on a specimen. Usually, the incident linearly polarized light beam becomes elliptical upon reflection on a specimen, which is the reason for naming [66].

The electric field vector E_j, revealing the state of polarization of the incident (j = i) and the reflected (j = r) light, is described by p-(parallel to the plane of incidence) and s-(perpendicular to the plane of incidence)polarized components: $E_\mathrm{j} = E_\mathrm{jp} + E_\mathrm{js}$. Upon interaction of the linearly polarized light with the specimen surface, the light gets typically elliptically polarized due to a change in phase and amplitude of the reflected p-and s-polarized components. The change in polarization is described by the ratio of the amplitude reflection coefficients, r_p and r_s, for p- and s-components, which are composed of the ratios of the reflected to the incident electric fields. The ellipsometric parameters Ψ and Δ are then given by:

$$\rho = \tan\Psi \exp(\mathrm{i}\Delta) = \frac{r_\mathrm{p}}{r_\mathrm{s}} = \left(\frac{E_\mathrm{rp}}{E_\mathrm{ip}}\right) \Big/ \left(\frac{E_\mathrm{rs}}{E_\mathrm{is}}\right). \tag{1.1}$$

The ellipsometric parameter Ψ describes the amplitude ratio between reflected p- and s-polarized components, while Δ represents the phase difference between reflected p- and s-polarized components [66]. A schematic illustration of the measurement principle of spectroscopic ellipsometry is given in Figure 1.5.

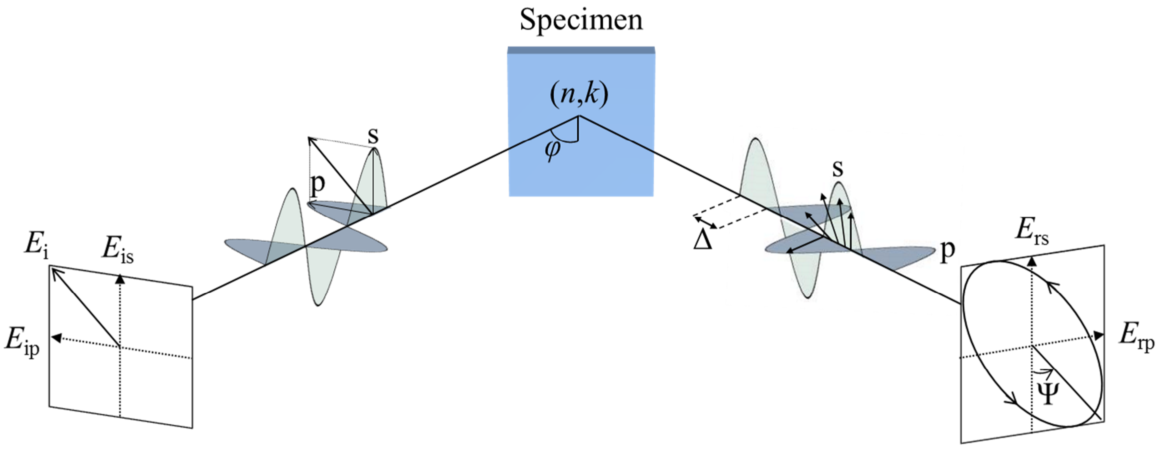

Figure 1.5: The measurement principle of ellipsometry as adopted from Ref. [66].

In the present work, spectroscopic ellipsometric investigations were performed in order to determine the change of oxide-film thickness as function of the oxidation time at constant oxidation temperatures. The ellipsometric measurements were performed with a J.A. Woollam M-2000$^\mathrm{TM}$ spectroscopic ellipsometer, equipped with a Xe light source, by recording $\Psi(\lambda, \varphi)$ and $\Delta(\lambda, \varphi)$ in a wavelength range of $\lambda = 300$ nm – 850 nm and at variable angles of incidence of $\varphi = 60°, 65°, 70°$ and 75° (with respect to the specimen-surface normal). From the recorded ellipsometric values, $\Psi(\lambda, \varphi)$ and $\Delta(\lambda, \varphi)$, and by adopting an optical model description for the evolving oxide/alloy-substrate system the oxide-film growth kinetics have been determined.

1.4.4 Microelectrochemical measurements

The electrochemical microcapillary technique enables the measurements of local (electrochemical) corrosion currents of a very small area of the alloy [67-69] and as such, the *intrinsic* corrosion behavior of passivating metal and alloy surfaces. This is not possible with large-scale electrochemical scanning methods for which the measured corrosion behavior is generally affected by compositional and structural inhomogeneities, scratches, contamination or other local defects within the immersed sample area.

Microelectrochemical measurements were carried out on as-deposited and oxidized am-Al_xZr_{1-x} alloys applying the electrochemical microcapillary technique [68, 70]. The microcapillary, filled with an electrolyte (1 M HCl, pH = 0), acts as an electrochemical cell connecting the working electrode, i.e. the (oxidized) am-Al_xZr_{1-x} specimen, with the Pt counter electrode. A saturated calomel electrode (SCE), to which all potentials are referred, is connected via an electrolytic bridge. The tip of the microcapillary has a diameter of 300 µm, defining the size of the investigated area, and a silicon seal, which hinders the leaking of the electrolyte during contact with the am-Al_xZr_{1-x} alloy surface. A schematically drawing of the experimental setup is given in Figure 1.6a.

Prior to the potentiodynamic polarization measurements, the microcapillary is positioned on the sample (see Figure 1.6b) and the open circuit potential (OCP), i.e. the potential of the specimen (working electrode) relative to the reference electrode in absence of an applied potential, is recorded for 5 minutes. Thereupon, potentiodynamic polarization curves, i.e. the current density as a function of the applied potential, with a scan rate of 1 mVs^{-1} were recorded starting from a potential 250 mV more negative than the recorded OCP. Investigation of the microelectrochemical behavior of the specimens has been performed on at least three different locations on the specimen surface in order to examine the homogeneity of the corrosion behavior.

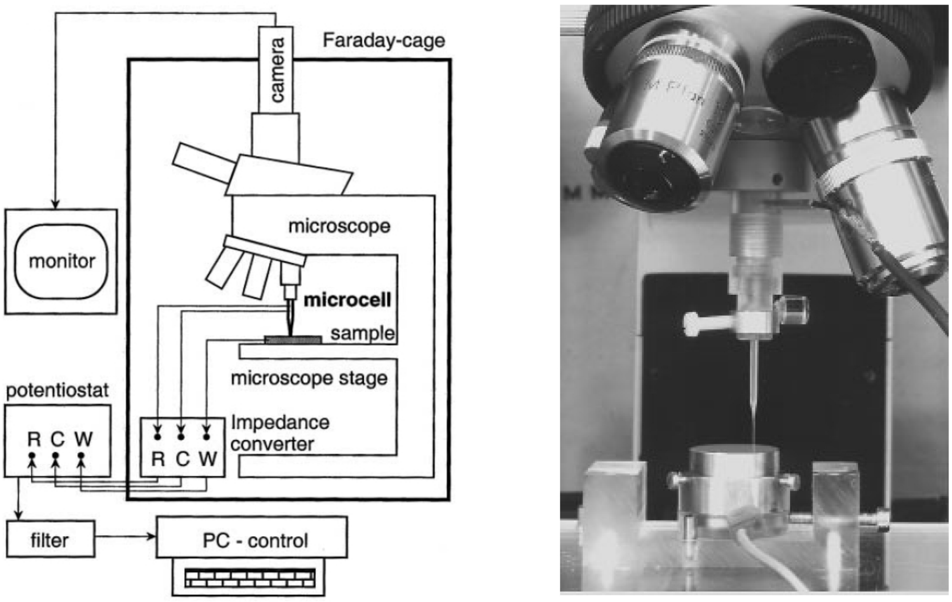

(a) (b)

Figure 1.6: (a) Schematic illustration of the electrochemical microcapillary technique setup and **(b)** the microcapillary, mounted on a microscope, in contact with the sample. Images taken from Ref. [69].

1.5 Outline of the thesis

In recent years, amorphous metallic alloys have been intensively investigated because of their remarkable physical and chemical properties, e.g. high corrosion resistance [4-6]. Despite these intensive research activities, until now little is known about the oxidation behavior of the amorphous metallic alloys. This thesis presents a comprehensive and fundamental investigation of the oxidation behavior of am-Al_xZr_{1-x} alloys, in particular, the oxidation mechanism, the developing oxide microstructure and the oxide growth kinetics, using a combinatorial experimental approach using XRD, cross-sectional (analytic) TEM, AES sputter-depth profiling and SE.

Chapter 2 addresses the development of oxide phases and microstructure upon thermal oxidation of am-Al_xZr_{1-x} alloys ($0.26 \leq x \leq 0.68$) in the temperature range of 350 °C – 500 °C. Special focus was on the influence of am-Al_xZr_{1-x} alloy composition and oxidation conditions on the developing oxide layer. The role of thermodynamics on the oxide layer composition is discussed.

Chapter 3 presents the oxide growth kinetics of amorphous (Al,Zr)-oxide layers, as grown by thermal oxidation of am-Al_xZr_{1-x} alloys ($0.26 \leq x \leq 0.68$) at oxidation temperatures of 350 °C – 400 °C. Further, the oxygen solubility and diffusivity in the amorphous alloys as function of the amorphous alloy composition are investigated. The relationships between the observed oxidation kinetics, the oxygen diffusivity and solubility in the amorphous alloy and the composition of the amorphous oxide layer are discussed and an oxidation mechanism is proposed.

Chapter 4 deals with the thermal oxidation of an am-$Al_{0.44}Zr_{0.56}$ alloy at high oxidation temperatures of 500 °C - 560 °C. The nucleation of a crystalline tetragonal ZrO_2 (t-ZrO_2) phase upon prolonged oxidation at 560 °C, immediately underneath the initially formed amorphous oxide layer, is discussed with regard to oxidation-induced compositional changes in the alloy below the reacting alloy/oxide interface.

In Chapter 5, the local electrochemical behavior of as-deposited and oxidized am-Al_xZr_{1-x} alloys is investigated with the electrochemical microcapillary technique. The local electrochemical behavior of as-deposited am-Al_xZr_{1-x} alloys ($0.26 \leq x \leq 0.75$) is examined with regard on the alloy composition. The effect of a pre-oxidation treatment of am-Al_xZr_{1-x} alloys ($0.35 \leq x \leq 0.68$) on their electrochemical behavior is discussed in terms of the properties of the thermally-grown am-(Al,Zr)- oxide overlayers.

1.6 References

[1] Munoz-Gil D., Perez-Coll D., Pena-Martinez J., Garcia-Martin S., J. Power Sources **263** (2014) 90.

[2] Mitra R., Rao V.V.R., Mater. Sci. Eng. A-Struct. Mater. Prop. Microstruct. Process. **260** (1999) 146.

[3] Hsieh H.H., Kai W., Huang R.T., Pan M.X., Nieh T.G., Intermetallics **12** (2004) 1089.

[4] Scully J.R., Lucente, A., American Society of Metals **13B** (2005) 476.

[5] Köster U., Jastrow L., Mater. Sci. Eng. A-Struct. Mater. Prop. Microstruct. Process. **449** (2007) 57.

[6] Hashimoto K., Kumagai N., Yoshioka H., Kim J.H., Akiyama E., Habazaki H., Mrowec S., Kawashima A., Asami K., Corros. Sci. **35** (1993) 363.

[7] Yoshioka H., Habazaki H., Kawashima A., Asami K., Hashimoto K., Electrochim. Acta **36** (1991) 1227.

[8] Weller K., Zotov N., Wang Z.M., Jeurgens L.P.H., Mittemeijer E.J., J. Non-Cryst. Solids **427** (2015) 104.

[9] Wang W.H., Dong C., Shek C.H., Mater. Sci. Eng. R **44** (2004) 45.

[10] Johnson W.L., MRS Bull. **24** (1999) 42.

[11] Zberg B., Uggowitzer P.J., Löffler J.F., Nat. Mater. **8** (2009) 887.

[12] Inoue A., Sci. Rep. Res. Inst. Tohoku Univ. Ser. A-Phys. Chem. Metall. **42** (1996) 1.

[13] Inoue A., Takeuchi A., Acta Mater. **59** (2011) 2243.

[14] Klement W., Willens R.H., Duwez P., Nature **187** (1960) 869.

[15] Inoue A., Acta Mater. **48** (2000) 279.

[16] Riedel E. Allgemeine und Anorganische Chemie: Walter de Gruyter, 2010.

[17] Hashimoto K., Park P.Y., Kim J.H., Yoshioka H., Mitsui H., Akiyama E., Habazaki H., Kawashima A., Asami K., Grzesik Z., Mrowec S., Mater. Sci. Eng. A-Struct. Mater. Prop. Microstruct. Process. **198** (1995) 1.

[18] Nomura K., Ohta H., Takagi A., Kamiya T., Hirano M., Hosono H., Nature **432** (2004) 488.

[19] Kamiya T., Hosono H., NPG Asia Mater **2** (2010) 15.

[20] Leskelä M., Kukli K., Ritala M., J. Alloy. Compd. **418** (2006) 27.

[21] Chaneliere C., Autran J.L., Devine R.A.B., Balland B., Materials Science and Engineering: R: Reports **22** (1998) 269.

[22] Nie X.P., Yang X.H., Chen L.Y., Yeap K.B., Zeng K.Y., Li D., Pan J.S., Wang X.D., Cao Q.P., Ding S.Q., Jiang J.Z., Corros. Sci. **53** (2011) 3557.

[23] Hotovy I., Huran J., Spiess L., Hascik S., Rehacek V., Sensors and Actuators B: Chemical **57** (1999) 147.

[24] Roy S., Basu S., Bull Mater Sci **25** (2002) 513.

[25] Jeurgens L.P.H., Sloof W.G., Tichelaar F.D., Mittemeijer E.J., Phys. Rev. B **62** (2000) 4707.

[26] Reichel F., Jeurgens L.P.H., Mittemeijer E.J., Acta Mater. **56** (2008) 659.

[27] Kofstad P. High-temperature oxidation of metals. New York: John Wiley & Son, 1966.

[28] Birks N., Meier G.H., Pettit F.S. Introduction to the High Temperature Oxidation of Metals. Cambridge: Cambridge University Press, 2006.

[29] Fromhold A.T. Theory of metal oxidation: North Holland Pub. Co., 1975.

[30] Wagner C., Z. Phys. Chem. B-Chem. Elem. Aufbau. Mater. **21** (1933) 25.

[31] Naka M., Hashimoto K., Masumoto T., J. Non-Cryst. Solids **31** (1979) 355.

[32] Vargel C. Corrosion of aluminium. Amsterdam: Elsevier, 2004.

[33] Davis J.R., editor Corrosion of aluminum and aluminum alloys. Materials Park, OH: ASM International, 1999.

[34] McCafferty E., Corros. Sci. **42** (2000) 1993.

[35] Vargel C., Jacques M., Schmidt M.P. Chapter B.1 - The Corrosion of Aluminium. In: Schmidt CVJP, editor. Corrosion of Aluminium. Amsterdam: Elsevier, 2004. p.81.

[36] Deltombe E. P.M., Cebelcor, rapport technique no. 42 (1956).

[37] Kematick R.J., Franzen H.F., J. Solid State Chem. **54** (1984) 226.

[38] Guan Z.-l., Wu C.-l., Vac. Sci. Technol. **4** (1984) 198.

[39] Barosi A., Rabusin E., Jpn. J. Appl. Phys. (1974) 49.

[40] Vegelius J., Soroka I.L., Korelis P.T., Hjorvarsson B., Butorin S.M., J. Phys. Condens. Matter **23** (2011) 265503.

[41] Itakura M., Kaburaki H., Arakawa C., Phys. Rev. E **71** (2005).

[42] Robertson J., Rep. Prog. Phys. **69** (2006) 327.

[43] Zhao C., Richard O., Young E., Bender H., Roebben G., Haukka S., De Gendt S., Houssa M., Carter R., Tsai W., Van ber Biest O., Heyns M., J. Non-Cryst. Solids **303** (2002) 144.

[44] Fecht H.J., Han G., Fu Z., Johnson W.L., J. Appl. Phys. **67** (1990) 1744.

[45] Ma E., Brunner F., Atzmon M., J. Phase Equilib. **14** (1993) 137.

[46] Sheng H.W., Lu K., Ma E., J. Appl. Phys. **85** (1999) 6400.

[47] Rehn L.E., Okamoto P.R., Pearson J., Bhadra R., Grimsditch M., Phys. Rev. Lett. **59** (1987) 2987.

[48] Soroka I.L., Vegelius J., Korelis P.T., Fallberg A., Butorin S.M., Hjorvarsson B., J. Nucl. Mater. **401** (2010) 38.

[49] Ho J.K., Lin K.L., J. Appl. Phys. **75** (1994) 2434.

[50] Gudzenko V.N., Polesya A.F., Phys. Met. Metallogr. **39** (1975) 177.

[51] Sun X., Schneider S., Geyer U., Johnson W.L., Nicolet M.A., J. Mater. Res. **11** (1996) 2738.

[52] Zander D., Köster U., Mater. Sci. Eng. A-Struct. Mater. Prop. Microstruct. Process. **375** (2004) 53.

[53] Kimura H.M., Asami K., Inoue A., Masumoto T., Corros. Sci. **35** (1993) 909.

[54] Harmelin M., Fabrichnaya, O. Aluminium-Oxygen-Zirconium: Springer-Verlag Berlin Heidelberg, 2009.

[55] Fabrichnaya O., Aldinger F., Z. Metallk. **95** (2004) 27.

[56] Claussen N., Ruhle M., Heuer A., (1983).

[57] Levin I., Brandon D., J. Am. Ceram. Soc. **81** (1998) 1995.

[58] Wagner C., J. Electrochem. Soc. **103** (1956) 571.

[59] Yoshioka H., Habazaki H., Kawashima A., Asami K., Hashimoto K., Corros. Sci. **33** (1992) 425.

[60] Yoshioka H., Yan Q., Habazaki H., Kawashima A., Asami K., Hashimoto K., Corros. Sci. **31** (1990) 349.

[61] Hashimoto K., Osada K., Masumoto T., Shimodaira S., Corros. Sci. **16** (1976) 71.

[62] Ayache J., Beaunier L., Boumendil J., Ehret G., Laub D. Sample Preparation Handbook for Transmission Electron Microscopy: Methodology. Berlin: Springer, 2010.

[63] Briggs D., Grant J., editors. Surface analysis by Auger and X-ray photoelectron spectroscopy: IMPublications, Chichester and SurfaceSpectra, Manchester, 2003.

[64] Drude P., Annalen der Physik **268** (1887) 584.

[65] Vedam K., Thin Solid Films **313** (1998) 1.

[66] Fujiwara H. Spectroscopic ellipsometry: principles and applications: John Wiley & Sons, 2007.

[67] Bohni H., Suter T., Schreyer A., Electrochim. Acta **40** (1995) 1361.

[68] Suter T., Bohni H., Electrochim. Acta **42** (1997) 3275.

[69] Suter T., Bohni H., Electrochim. Acta **47** (2001) 191.

[70] Bohni H., Suter T., Assi F., Surf. Coat. Technol. **130** (2000) 80.

Chapter 2

Thermodynamics controls amorphous oxide formation: Exclusive formation of a stoichiometric amorphous $(Al_{0.33}Zr_{0.67})O_{1.83}$ phase upon thermal oxidation of Al-Zr

Katharina Weller, Zumin Wang, Lars P. H. Jeurgens and Eric J. Mittemeijer

Abstract

During thermal oxidation of binary amorphous Al_xZr_{1-x} solid solutions over wide alloy-composition ($0.26 \leq x \leq 0.68$) and oxidation-temperature (350 °C – 560 °C) ranges, a single *amorphous* ternary oxide phase of well-defined stoichiometry, $(Al_{0.33}Zr_{0.67})O_{1.83}$, emerges. The composition of this unexpectedly stoichiometric ternary amorphous oxide phase, that develops instead of the crystalline oxide phases Al_2O_3 and ZrO_2, under conditions far away from genuine thermodynamic equilibrium, is governed by thermodynamics, as demonstrated by thermodynamic assessment, adopting the amorphous $(Al_{0.33}Zr_{0.67})O_{1.83}$ phase as a supercooled liquid oxide-oxide (Al_2O_3-ZrO_2) solution phase.

2.1 Introduction

Metallic alloys oxidize naturally under environmental air during service conditions, leading to oxide overgrowth on the alloy surface [1]. The composition and structure of the developing oxide layer determine various important surface-related properties of alloys, such as friction, wear, adhesion, catalytic activities, corrosion resistance and long-term stability/reliability, which are of vital importance in real-life applications [2]. Amorphous oxides have a more homogenous structure and possibly also a more homogenous composition as compared to their crystalline counterparts, which can result in improved surface properties [3]. Therefore, formation of amorphous oxide layers upon oxidation of alloys is often preferred in view of practical applications. Recently, in particular multi-component amorphous oxides have drawn great interest as building blocks of advanced electronic components [4]: for example, transparent conducting oxides (e.g. *am*-In_2O_3-ZnO) [5], amorphous oxide semiconductors (e.g. *am*-In_2O_3-

Ga_2O_3-ZnO) [6, 7] and amorphous oxide high-*k* dielectrics (e.g. *am*-ZrO_2-Al_2O_3, *am*-HfO_2-SiO_2) [8].

The atomic structure and formation mechanism of amorphous oxides, especially for multi-component amorphous oxides, are still poorly understood. The bulk Gibbs energy of formation of an amorphous oxide is always larger (less negative) than that of the corresponding crystalline oxide and therefore the amorphous oxide is normally considered to be thermodynamically metastable. However, it has been shown that the growth of ultrathin (typically below 2 nm) amorphous oxide films on pure metals and metallic alloys can be thermodynamically preferred due to their favorably low surface and interface energies [9, 10]. The occurrence of thicker amorphous oxide layers, instead, is usually considered to be a consequence of kinetic obstructions for the formation of the stable crystalline oxide phase(s) at the relatively low oxidation temperatures [11, 12]; the composition of these relatively thick amorphous oxide layers then is believed to be controlled by oxidation kinetics (which depends on the original alloy composition and the relative transport rates of metal atoms/cations through the oxide film) (see e.g. [13, 14]).

In contrast with this common interpretation, in this work it is shown that, upon growth of relatively thick (at least up to a few 100 nm) amorphous oxide layers by thermal oxidation of binary metallic alloys, the composition of the formed multi-component amorphous oxide layer can be fully governed by *bulk thermodynamics*. Such results are presented for the thermal oxidation of binary amorphous Al_xZr_{1-x} alloys where, over wide alloy-composition ($0.26 \leq x \leq 0.68$) and oxidation-temperature (350 – 560 °C) ranges, a single amorphous ternary oxide phase with a well-defined stoichiometry, am-$(Al_{0.33}Zr_{0.67})O_{1.83}$, forms, which can be fully explained on a thermodynamic basis. Generally, the finding demonstrates that bulk thermodynamics can still control precisely a material process even under conditions far away from the genuine thermodynamic equilibrium.

2.2 Experimental procedures and data evaluation

2.2.1 Amorphous Al_xZr_{1-x} alloy specimen preparation

Amorphous Al_xZr_{1-x} coatings (thickness about 2 μm) were deposited onto Si(100) wafers (4-inch, covered with am-SiO_2 and am-Si_3N_4 layers, each 50 nm thick), by co-sputtering from pure Al (purity 99.9995 wt.%) and Zr (purity 98.5 wt.%) targets in an ultrahigh-vacuum sputter system (base pressure ~ 5×10^{-7} Pa). The wafer substrates were sputter-cleaned for 1 minute by Ar^+ ions with an applied acceleration voltage of 105 V prior to the layer-deposition process. During deposition an equilibrium chamber pressure of 0.5 Pa was maintained by introducing the Ar gas (purity 99.9999 at.%) at a constant flow rate of 15 ml/min. During sputter-cleaning and the subsequent layer deposition the wafer substrates were rotated with a rotation speed of a few tens of cycles per minute.

The deposition of the amorphous Al_xZr_{1-x} alloys was carried out by keeping the power applied to the Zr target constant at P_{Zr} = 100 W, while varying the power applied to the Al target (P_{Al} = 20 – 101 W), leading to various alloy compositions: $Al_{0.26}Zr_{0.74}$, $Al_{0.35}Zr_{0.65}$ $Al_{0.51}Zr_{0.49}$, $Al_{0.68}Zr_{0.32}$. The compositions of the sputter-deposited am-Al_xZr_{1-x} alloys were determined by inductively coupled plasma optical emission spectroscopy (ICP-OES) measurements of alloy specimens deposited under the same conditions on polyimide foils (Kapton®, DuPont). The compositions of the as-deposited am-Al_xZr_{1-x} alloys, as well as their corresponding sputter parameters have been listed in Table 2.1. The thickness of the deposited am-Al_xZr_{1-x} alloys is about 2 µm (as measured with a Veeco DekTak 8 profilometer).

Table 2.1: Parameters applied for sputter deposition of the Al_xZr_{1-x} specimens and the resulting specimen compositions as determined by ICP-OES.

specimen code	P_{Al} (W)	P_{Zr} (W)	Al content (at.-%)	Zr content (at.-%)
$Al_{0.26}Zr_{0.74}$	20	100	25.6	74.4
$Al_{0.35}Zr_{0.65}$	28	100	35.1	64.9
$Al_{0.51}Zr_{0.49}$	53	100	50.9	49.1
$Al_{0.68}Zr_{0.32}$	101	100	68.0	32.0

2.2.2 Oxidation of am-Al_xZr_{1-x} alloys

Oxidation of the am-Al_xZr_{1-x} specimens was performed in quartz ampoules at oxidation temperatures T_{ox} in the range of 350 – 560 °C under a constant oxygen partial pressure of $p_{O_2} = 1 \times 10^5$ Pa.[1] To ensure the same oxidation conditions for a set of specimens, a special construction in each quartz ampoule holds a set of specimens of all different compositions. Oxidation of the specimens in the such-prepared quartz ampoules was performed in a pre-heated sandbath (TECHNE FB-08c) at different T_{ox} for different oxidation times (t_{ox} = 1, 2.5, 5, 7.5 and 10 h). After the oxidation, the quartz ampoules were immediately quenched in water ($T \sim 18$ °C), which promptly terminated the oxidation process. The grown oxide layers have thicknesses in the range of 4 nm to 160 nm (as determined by spectroscopic ellipsometric (SE) investigations, see [15]), depending on T_{ox}, t_{ox} and the parent alloy composition.

2.2.3 Structural and compositional characterization

The structure of the as-deposited and oxidized am-Al_xZr_{1-x} specimens was investigated by X-ray diffractometry on a Bruker D8 Discover diffractometer equipped with a Cu X-ray anode (40 kV/30 mA). In combination with an X-ray lens, a parallel-plate collimator and an energy-dispersive detector, X-ray diffraction (XRD) θ-2θ scans were recorded in parallel-beam geometry using Cu-Kα radiation (λ = 1.54056 Å) in a continuous scanning mode over a 2θ range of 10° - 65°.

The chemical state of oxygen in the grown oxide layer was investigated by X-ray photoelectron spectroscopy (XPS) in a Thermo VG Thetaprobe XPS system (base pressure < $2 \cdot 10^{-8}$ Pa) using monochromatic Al Kα radiation ($h\nu$ = 1486.68 eV, analysis area ~400 μm in diameter). First, the oxidized am-Al_xZr_{1-x} specimen (am-$Al_{0.51}Zr_{0.49}$, oxidized at 350 °C for 10 hours) was sputter-cleaned with 1 keV Ar^+ for 240 seconds (sputtered area of 2×2 mm^2; sputter rate of about 1 nm/min) in the XPS system to remove surface contaminations. Then, the O 1s spectrum in a binding energy (BE) region of 526 - 539 eV was recorded with a step size of 0.1 eV at a constant pass energy of 50 eV. Calibration of the energy scale of the analyzer was performed as described in

---

[1] In order to obtain an oxygen partial pressure of $p_{O2} = 1 \times 10^5$ Pa at the oxidation temperature T_{ox} = 350 °C, the evacuated quartz ampoules were filled at room temperature (RT) with pure oxygen gas up to $p_{O2} = 4.70 \times 10^4$ Pa, which corresponds to $p_{O2} = 1 \times 10^5$ Pa at T_{ox} = 350 °C. Analogously, quartz ampoules were prepared for higher oxidation temperatures.

Ref. [16]. In order to obtain information about the local chemical environment of oxygen in the oxidized am-Al_xZr_{1-x} alloy surface, its O1 s spectrum was compared to recordings of the O1 s XPS spectra of an oxidized Zr(0001) single crystal surface (oxidation conditions: 227 °C, 10^{-4} Pa, 2 h) and of an oxidized Al(100) single crystal surface (oxidation conditions: 27 °C, 1 Pa, 95 minutes).

The structure of and the elemental distribution in the developing oxide layer and the adjacent am-Al_xZr_{1-x} alloy were investigated by high-resolution transmission electron microscopy (TEM) in combination with electron energy loss spectroscopy (EELS) elemental mapping in a scanning transmission electron microscope (STEM, JEOL JEM-ARM200F). EELS elemental mapping was performed by recording spectra point-by-point (i.e. a set of EELS spectra at each point/pixel) in a region of interest as observed in the STEM. The noise in the recorded EELS spectra was filtered by principal component analysis [17, 18] utilizing the Gatan DigitalMicrograph software. A power-law background was subtracted from the filtered EELS spectra to determine the signal intensities of the O K edge, the Al L edge and the Zr M edge. On this basis elemental maps of Al, Zr and O were constructed.

Auger electron spectroscopy (AES) sputter-depth profiling was performed, using a JEOL JAMP 7830F Scanning Auger Microscope (for details of the experimental set-up, see [19]), to obtain information on the compositional distribution in the developing oxide layer and the underlying am-Al_xZr_{1-x} alloy substrate. An AES sputter-depth profile was obtained in a so-called discontinuous sputtering mode, where spectra of the Al LMM, Zr MNN and O KLL Auger lines were recorded after each successive ion sputtering step. Sputtering was performed with a focused 1 kV Ar^+ beam (a 2 kV Ar^+ beam for am-Al_xZr_{1-x} specimens with relatively thick oxide layers), scanning an area of 500×500 μm^2. Concentration-depth profiles derived from the spectral contributions of the oxidic and metallic species were obtained by linear least-squares fitting of the differential AES spectra (Phi-MultiPak software, version 7.5) and by multiplying the obtained peak-to-peak intensities with experimentally determined relative sensitivity factors. The relative sensitivity factors for metallic Al and metallic Zr were obtained directly from the recorded spectra of Al LMM and Zr MNN of an as-deposited am-Al_xZr_{1-x} alloy of known composition (i.e. am-$Al_{0.68}Zr_{0.32}$, measured by ICP-OES) and at the end of the sputter-depth profile (i.e. at a depth where pure substrate (am-Al_xZr_{1-x} alloy) occurs). The relative sensitivity factors for oxidic Al, oxidic Zr and O were obtained following the approach described in [19]. The thus experimentally determined sensitivity factors (with respect to metallic Al) are: $S_{\mathrm{Al}} = 1$, $S_{\mathrm{Zr}} = 1.05$, $S_{\mathrm{Zr^{ox}}} = 0.77$, $S_{\mathrm{Al^{ox}}} = 0.93$, $S_{\mathrm{O}} = 1.59$. Conversion of the sputter time to the (approximate) sputter depth was done straightforwardly for each sputter-depth profile on the basis of the known oxide-layer thickness as obtained from the SE investigations [15].

2.3 Results

2.3.1 Structure of as-deposited and oxidized am-Al_xZr_{1-x} alloys

The recorded XRD patterns of the as-deposited am-Al_xZr_{1-x} alloys confirm the amorphous nature of the Zr_xAl_{1-x} coatings: only very broad intensity humps, in a range of 2θ ~ 35° - 38°, are observed for the alloys of different composition (Figure 2.1a). The recorded XRD patterns of the oxidized am-Al_xZr_{1-x} alloys ($0.26 \leq x \leq 0.51$) after oxidation at 400 °C for 10 h and of the am-$Al_{0.68}Zr_{0.32}$ alloy after oxidation at 400 °C for even 20 h also do not show any diffraction peak, indicative of a developing crystalline intermetallic Zr-Al alloy phase and/or a crystalline pure ZrO_2, Al_2O_3 or mixed (Al,Zr)-oxide phase (see Figure 2.1b). It follows that the evolving oxide-layer/alloy-substrate system maintains fully XRD *amorphous* over the temperature range of 350 °C to 400 °C.

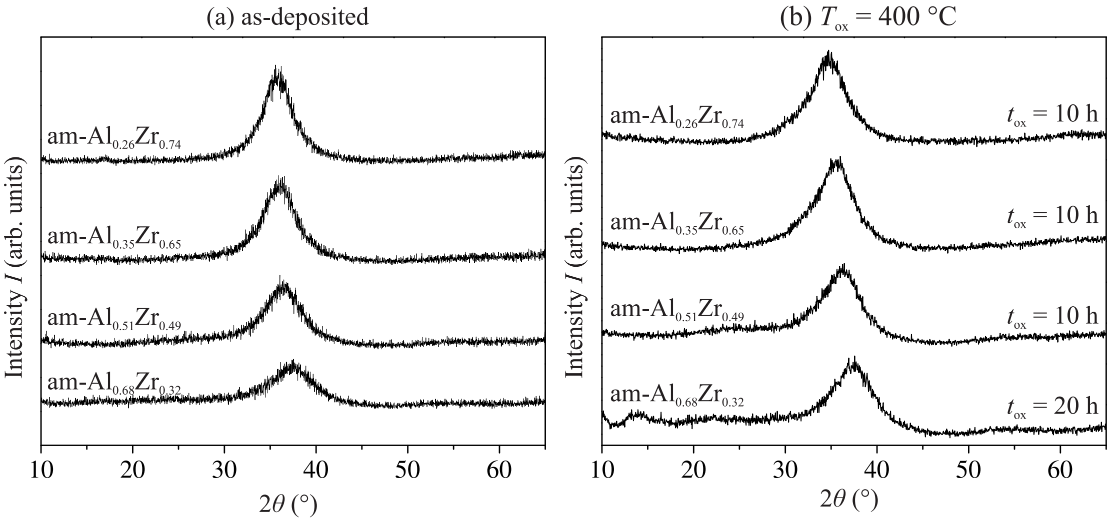

Figure 2.1: X-ray diffraction patterns (Cu-Kα radiation) of am-Al_xZr_{1-x} specimens of different compositions x (x = 0.26, 0.35, 0.51, 0.68): **a)** as-deposited and **b)** after thermal oxidation at 400 °C for 10 h (x = 0.26, 0.35, 0.51) and for 20 h (x = 0.68).

A cross-sectional bright-field TEM micrograph of a typical oxide layer (formed on the am-$Al_{0.51}Zr_{0.49}$ alloy after oxidation at 400 °C for 10 h) with its corresponding selected area diffraction pattern (SADP), recorded from a region comprising both the oxide and the alloy layer, is shown in Figure 2.2a. The TEM analysis confirms that, even after prolonged oxidation at an elevated temperature of 400 °C, both the oxide overgrowth and the parent alloy remain fully amorphous. The amorphous oxide overgrowth possesses a uniform thickness of about 40 nm (after 10 hours of oxidation at 400 °C). A cross-sectional annular dark-field TEM micrograph of the amorphous oxide layer and its corresponding elemental O, Zr, Al and combined (O+Zr+Al) maps, as recorded by subnanometer-resolution EELS elemental mapping (cf. Section 2.2.3), are shown in Figure 2.2b-f. The TEM-EELS analysis shows a *homogenous distribution* of all three elements (Al, Zr and O) and does not reveal any indication of nucleation (i.e. crystallization) and/or phase separation in the amorphous oxide layer, not even at the *subnanometer scale* (see in particular Figure 2.2f for a combined image of the Al, Zr and O maps). These results imply that the oxide layer is composed of a single, homogenous ternary amorphous oxide phase.

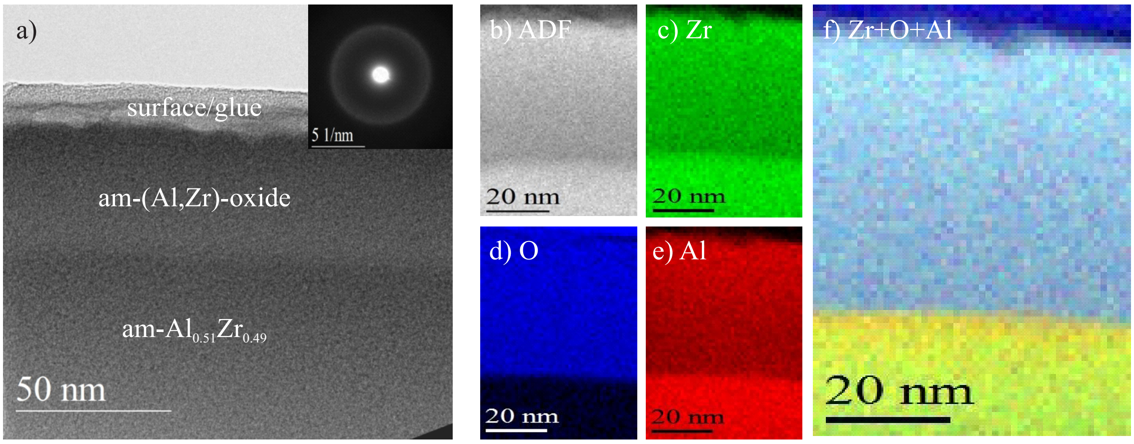

Figure 2.2: a) Bright-field TEM image of an am-$Al_{0.51}Zr_{0.49}$ specimen oxidized at 400 °C for 10 h, in which the formation of an amorphous oxide layer at the surface region is clearly observable. The inset shows the selected area diffraction pattern of the region comprising both the amorphous oxide and the adjacent substrate (the aperture diameter used was about 130 nm, containing both the amorphous oxide layer and the underlying amorphous solid solution substrate). The amorphous oxide layer, shown in the annular dark field TEM image in **b)**, has been analyzed by EELS elemental mapping of **c)** Zr, **d)** O and **e)** Al at very high (subnanometer) spatial resolution. A combined image of the O, Zr and Al EELS mappings is shown in **f)**.

The O 1s core-level spectrum, as recorded by XPS from the amorphous (Al,Zr)-oxide layer (see Figure 2.3), is constituted of a narrow and (more or less) symmetric single peak positioned at a BE of about 531.8 ± 0.1 eV, i.e. in between the corresponding O 1s BE values of pure Al_2O_3 (i.e. 532.2 ± 0.1 eV) and pure ZrO_2 (i.e. 531.3 ± 0.1 eV), as recorded from oxidized Al(100) and Zr(0001) single crystalline surfaces (cf. section 2.2.3), respectively. This observation is compatible with the above conclusion that the Al and Zr cations in the amorphous oxide phase are distributed homogenously on an atomic scale, corresponding to an (Al-O-Zr)-type local bonding configuration. Co-existing local chemical environments similar to those of pure Al_2O_3 and pure ZrO_2 were not observed (in such a case, either two O 1s main peaks would be resolved or the O 1s spectral envelope would be broader and likely (more) asymmetric). It can be concluded also that the XPS analysis indicates that the amorphous oxide layer is composed of a homogenous $(Al,Zr)_xO_y$ ternary oxide phase (rather than a mixture of amorphous ZrO_2 and Al_2O_3 binary oxides).

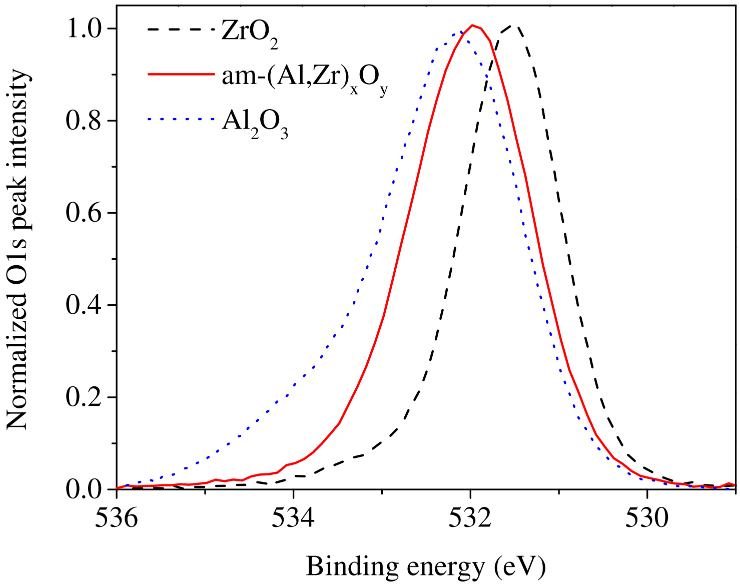

Figure 2.3: Normalized O1s XPS spectra of **(i)** an oxidized Zr(0001) single crystal surface (oxidation conditions: 227 °C, p_{O2} = 10^{-4} Pa, 2 h [20]), **(ii)** the oxidized am-$Al_{0.51}Zr_{0.49}$ alloy (oxidation conditions: 350 °C, p_{O2} = 10^{5} Pa, 10 h) and **(iii)** an oxidized Al(100) single crystal surface (oxidation conditions: 27 °C, p_{O2} = 1 Pa, 95 minutes; see Ref. [21]).

2.3.2 Oxide composition upon oxidation of am-Al_xZr_{1-x} ($0.26 \leq x \leq 0.68$) alloys

The chemical compositions of the grown oxide layers and of the underlying amorphous alloys upon thermal oxidation were investigated by AES sputter-depth profiling. The measured AES elemental concentration-depth profiles of Al and Zr in their metallic (further designated as Al^{met} and Zr^{met}) and oxidic (further designated as Al^{ox} and Zr^{ox}) states, as well as of O, are plotted for the various parent alloy compositions and oxidation temperatures (at a constant oxidation time of 10 h) in Figure 2.4. The grown oxide layers on am-Al_xZr_{1-x} alloys (in a composition range of $0.26 \leq x \leq 0.68$) contain both Al^{ox} and Zr^{ox} spectral contributions over the depth range of the whole oxide layer. The Al^{ox}/Zr^{ox} atomic ratio (for quantitative analyses, see below) in the oxide layers was found to be practically constant for most of the oxidized specimens, independent of the (sputter) depth, the parent am-Al_xZr_{1-x} substrate composition and T_{ox}. It is further evident from the AES profiles that the oxygen concentration in the am-Al_xZr_{1-x} alloy substrates, underneath the oxide layers, increases considerably with increasing Zr content, indicating that the oxygen solubility in the am-Al_xZr_{1-x} alloy substrate increases with the Zr content of the alloy substrate.

The overall composition of the grown oxide layers, expressed by the averaged Al^{ox}/Zr^{ox} atomic ratio[2] (as determined from the AES data) across the oxide layer for different oxidation conditions (for am-Al_xZr_{1-x} alloys (x = 0.26, 0.35, 0.51 and 0.68): 350 °C (t_{ox} = 10 h), 375 °C (t_{ox} = 10 h), 400 °C (t_{ox} = 10 h), 500 °C (t_{ox} = 1 h)[3]; for am-Al_xZr_{1-x} alloy (x = 0.51): 560 °C (t_{ox} = 10 h)), is plotted in Figure 2.5 as function of the initial Al/Zr ratio (i.e. = $x/(1-x)$) of the parent am-Al_xZr_{1-x} alloy substrate prior to each oxidation. Evidently, the Al^{ox}/Zr^{ox} ratio of the grown oxide layers is practically *constant* at about 0.5, independent of both the Al/Zr ratio in the parent am-Al_xZr_{1-x} alloy (for $0.26 \leq x \leq 0.68$) and the oxidation temperature (for 350 °C ≤ T ≤ 500 °C, for am-$Al_{0.51}Zr_{0.49}$: 350 °C ≤ T ≤ 560 °C). This implies that the composition of the grown, homogenous

---

[2] The concentration of oxygen c_O in all investigated oxide layers fits well, within the error of the AES analyses, with $c_O = 1.5c_{Al^{ox}} + 2c_{Zr^{ox}}$ (cf. Figure 2.4).

[3] At an oxidation temperature ≥ 500 °C only the am-$Al_{0.51}Zr_{0.49}$ alloy remains fully amorphous (cf. [19]). For the other am-Al_xZr_{1-x} alloy compositions (i.e. x = 0.26, 0.35 and 0.68), intermetallic phases start to crystallize from the alloy at T ≥ 500 °C. Nonetheless, the oxide layer formed on all alloys is fully amorphous also at T ≥ 500 °C and its composition remains unchanged.

oxide layers (an Al-Zr-O ternary oxide phase) can be given as $(Al_{0.33}Zr_{0.67})O_{1.83}$ [= $(AlO_{1.5})_1(ZrO_2)_2$].

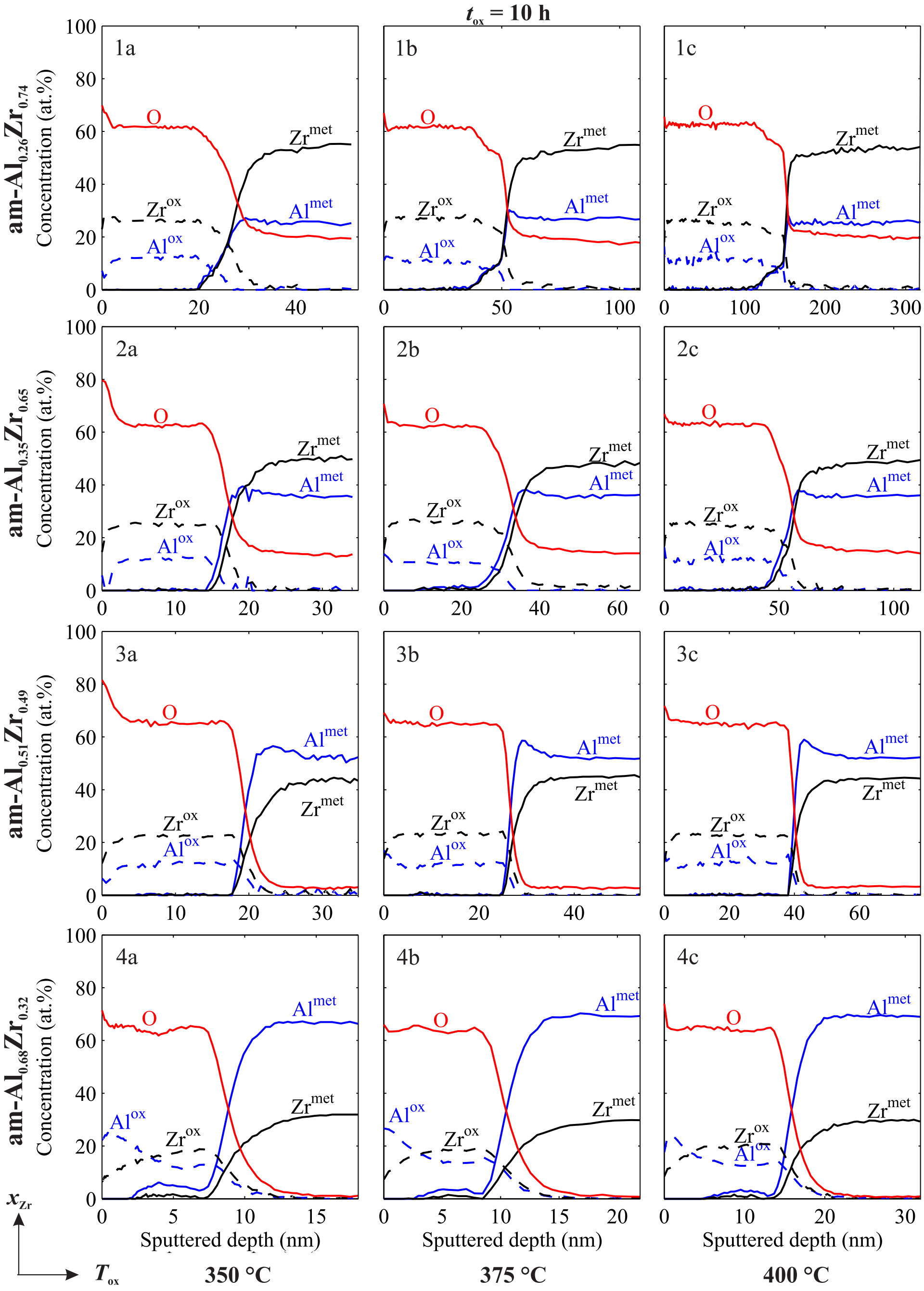

Figure 2.4: AES elemental concentration-depth profiles of am-Al$_x$Zr$_{1-x}$ solid solution substrates of different compositions x = 0.26 (**1**), 0.35 (**2**), 0.51 (**3**) and 0.68 (**4**), after oxidation at different temperatures of 350 °C (**a**), 375 °C (**b**) and 400 °C (**c**) for 10 hours at $p_{O2} = 10^5$ Pa, respectively. Note the different thicknesses of the oxide layers and that C contamination in surface-near regions (not considered in the quantification) has influenced the AES measurement in the beginning of the sputter-depth profiling (leading to unrealistically high amount of oxygen in the beginning of each measurement).

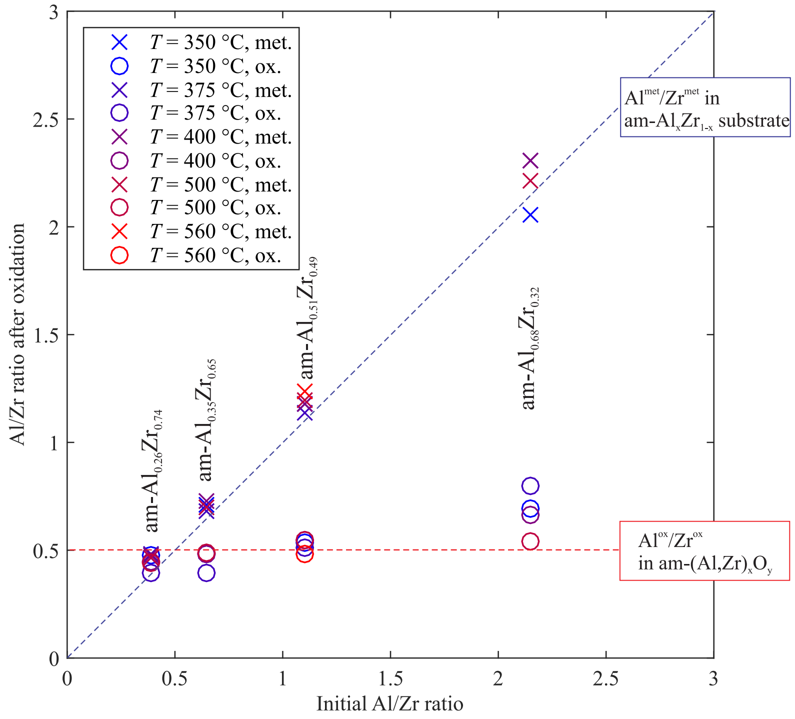

Figure 2.5: The Al^{ox}/Zr^{ox} ratio in the grown amorphous oxide (unfilled circles) and the Al^{met}/Zr^{met} ratio in the original am-Al_xZr_{1-x} substrate (crosses) upon thermal oxidation of am-Al_xZr_{1-x} alloys of different (initial) compositions at the temperatures indicated.

The composition of the oxide layer grown on the Al-richest, am-$Al_{0.68}Zr_{0.32}$ alloy is not fully homogenous (see 4a – 4c in Figure 2.4). The observed Al-rich oxide phase in the near-surface region may have formed during the very fast oxide growth at the initial stage of the oxidation [1]. During the subsequent, slower oxidation stage, the oxide-layer composition for this Al-richest am-Al_xZr_{1-x} alloy then (also) changes to that of a **Zr^{ox}-rich oxide** with an Al^{ox}/Zr^{ox} ratio of 0.66 at 400 °C and at $T \geq 500$ °C (for 1 h) with a constant Al^{ox}/Zr^{ox} ratio of about 0.5, in agreement with all other alloy compositions studied.

The above results can be summarized as follows: The grown oxide layers on the am-Al_xZr_{1-x} alloys

(i) are fully amorphous (by XRD and TEM with SADP);
(ii) have homogenous Al^{ox} and Zr^{ox} cation distributions down to the atomic scale (XPS and TEM with subnanometer-scale EELS mappings);
(iii) have a homogenous composition with a constant Al^{ox}/Zr^{ox} ratio of 0.5, independent of the alloy substrate composition and the oxidation temperature (AES).

The oxide layer grown on the am-Al_xZr_{1-x} alloys consists of an **amorphous, stoichiometric $(Al_{0.33}Zr_{0.67})O_{1.83}$ ternary oxide phase**, independent of both the parent alloy composition (for $0.26 \leq x \leq 0.68$) and the oxidation temperature (for 350 °C $\leq T \leq$ 500 °C, for am-$Al_{0.51}Zr_{0.49}$: 350 °C $\leq T \leq$ 560 °C).

2.4 Discussion

The experimental finding of both an **amorphous and stoichiometric $(Al_{0.33}Zr_{0.67})O_{1.83}$ ternary oxide phase upon thermal oxidation** is rather unexpected, because the pseudo-binary phase diagram (at 1 atm) of the Al_2O_3-ZrO_2 system predicts neither the occurrence of a mixed (Zr,Al)-oxide compound phase nor a considerable mutual solid 'solubility' of the pure phases Al_2O_3 and ZrO_2 at temperatures up to their eutectic point of 1856 °C [22].

In the following the amorphous nature of the oxide (section 2.4.1) and its singular composition (section 2.4.2) are addressed.

2.4.1 Amorphous nature of the $(Al_{0.33}Zr_{0.67})O_{1.83}$ ternary oxide phase

As known from a recent study [19], thermal oxidation of am-Al_xZr_{1-x} alloys, which are initially covered with an amorphous native (Al,Zr)-oxide film, proceeds by oxygen dissolution into the am-Al_xZr_{1-x} alloy substrate accompanied by subsequent growth of an amorphous (Al,Zr)-oxide layer into the oxygen-enriched amorphous solid solution phase once the oxygen solubility limit in the am-Al_xZr_{1-x} alloy substrate adjacent to the alloy/oxide interface is exceeded.

The formation of an amorphous oxide layer in the very beginning of oxidation is in line with recent studies, where it has been shown that very thin *amorphous* oxide layers (< 3 nm), formed during the initial oxidation process of crystalline metals [9, 23] and alloys [24], can be thermodynamically more stable compared to their crystalline counterparts due to their relatively low surface and interface energies. However, as soon as the amorphous oxide layer exceeds a critical thickness (typically in the range of 1 – 3 nm), the crystalline oxide phase should become the thermodynamically preferred one [10]. In the case of oxidation of am-Al_xZr_{1-x} alloys, the expected stable phases are the crystalline oxide phases Al_2O_3 (presumably γ-Al_2O_3 [9, 10]) and ZrO_2 (presumably tetragonal ZrO_2, further designated as t-ZrO_2 [19]), since neither a ternary crystalline (Al,Zr)-oxide compound phase nor a considerable mutual 'solubility' of crystalline Al_2O_3 and ZrO_2 are observed in the pseudo-binary Al_2O_3-ZrO_2 system [22]. Hence, at first glance, transformation of the formed amorphous (Al,Zr)-oxide phase (here: $(Al_{0.33}Zr_{0.67})O_{1.83}$) into the mentioned crystalline oxide phase(s) is expected. However, the formation of these crystalline oxide phases in the amorphous $(Al_{0.33}Zr_{0.67})O_{1.83}$ oxide phase is not observed, even though the amorphous $(Al_{0.33}Zr_{0.67})O_{1.83}$ oxide layers attain a very large thickness (4 nm - 160 nm) by growth into the am-Al_xZr_{1-x}[O] solid solution. Also, no formation of crystalline oxide phases in the amorphous Al_xZr_{1-x}[O] solid solution phase is observed. Apparently, the nucleation of crystalline oxide phases (i.e. γ-Al_2O_3 and *t*-ZrO_2) is inhibited in both the amorphous $(Al_{0.33}Zr_{0.67})O_{1.83}$ oxide phase and the amorphous Al_xZr_{1-x}[O] solid solution phase (at least within the studied compositional and temperature ranges of $0.26 \leq x \leq 0.68$ and $350\ °C \leq T \leq 560\ °C$).[4]

According to classical nucleation theory, for formation of a (spherical) particle, a nucleation barrier, $\Delta G^* = 16\pi\gamma^3/3(\Delta G_{chem} + \Delta G_{strain})^2$ [25], must be surpassed, which is defined by the contributions of the chemical Gibbs energy, ΔG_{chem} (< 0), the interface energy, γ (> 0), associated with the formation of interfaces, and the strain energy, ΔG_{strain} (> 0), associated with the (elastic) accommodation of volume misfit of the parent phase (here: amorphous $(Al_{0.33}Zr_{0.67})O_{1.83}$ oxide or am-Al_xZr_{1-x}[O] solid solution) and of the product phase (here: crystalline oxide). For precipitates of a crystalline phase in an amorphous matrix, the misfit-strain energy may be negligible as a consequence of rapid stress relaxation in the *amorphous* matrix. Then, the formation of the crystalline oxide phases (in both the amorphous $(Al_{0.33}Zr_{0.67})O_{1.83}$ oxide phase and the am-Al_xZr_{1-x}[O] solid solution) can be inhibited by a high energy barrier for the nucleation of crystalline oxide phases due to the creation of the new interfaces.

However, the nucleation of crystalline γ-Al_2O_3 and *t*-ZrO_2 phases within the amorphous $(Al_{0.33}Zr_{0.67})O_{1.83}$ oxide phase or within the amorphous am-Al_xZr_{1-x}[O] solid solution phase may also be inhibited by diffusional constraints. Because the solubility of Al and Al^{ox} in the crystalline oxide phase *t*-ZrO_2 and, vice versa, the solubility of Zr and Zr^{ox} in the crystalline oxide phase γ-Al_2O_3 are extremely low [22, 26, 27], the development of crystalline oxides, *t*-ZrO_2 and γ-Al_2O_3, either in the amorphous Al_xZr_{1-x}[O] solid solution phase or in the amorphous $(Al_{0.33}Zr_{0.67})O_{1.83}$ oxide phase would involve significant compositional redistribution, which requires pronounced atomic

---

[4] Note that at relatively high oxidation temperatures ($T \geq 560$°C) and prolonged oxidation times crystalline compounds as *t*-ZrO_2 do develop at the interface between the amorphous $(Al_{0.33}Zr_{0.67})O_{1.83}$ oxide phase and the O-saturated am-Al_xZr_{1-x}[O] solid solution [19].

diffusion in both the amorphous Al_xZr_{1-x}[O] solid solution and the amorphous $(Al_{0.33}Zr_{0.67})O_{1.83}$ oxide. At the relatively low oxidation temperatures (below 560 °C), pronounced diffusion may not occur and thus the formation of nuclei of the crystalline oxide phases would be obstructed. Note that the growth of the amorphous $(Al_{0.33}Zr_{0.67})O_{1.83}$ oxide phase at the interface with the O-saturated am-Al_xZr_{1-x}[O] solid solution phase requires less severe compositional rearrangement.

2.4.2 Stoichiometric composition of the $(Al_{0.33}Zr_{0.67})O_{1.83}$ ternary oxide phase

The well-defined stoichiometry of the $(Al_{0.33}Zr_{0.67})O_{1.83}$, oxide phase grown on the am-Al_xZr_{1-x} solid solution substrate, independent of both the substrate composition (for $0.26 \leq x \leq 0.68$) and the oxidation temperature (for am-Al_xZr_{1-x} ($0.26 \leq x \leq 0.68$): 350 °C $\leq T \leq$ 500 °C, for am-$Al_{0.51}Zr_{0.49}$: 350 °C $\leq T \leq$ 560 °C), strongly suggests a predominant role of thermodynamics in controlling the amorphous oxide growth. Thus, thermodynamic modeling and calculation of the pseudo-binary $AlO_{1.5}$-ZrO_2 system was performed using the CALPHAD approach [28]. Since the structure of an amorphous phase resembles that of the corresponding liquid phase of disordered structure, the amorphous oxide phase $(AlO_{1.5})_y(ZrO_2)_{1-y}$ was treated as a configurationally frozen liquid below the glass transition temperature by extrapolating the thermodynamic data of the corresponding liquid phase above the melting temperature to below the glass transition temperature. Note that an extreme extrapolation of thermodynamic data from high temperatures can lead to an underestimation of the enthalpy of mixing at low temperatures [29].

A CALPHAD assessment of the Al_2O_3-ZrO_2 pseudo-binary system has been made in Ref. [30] on the basis of the thermodynamic data presented in Refs. [31] and [32]. The liquid/amorphous phase is described by a regular solution model for ionic melts, i.e. the two-sublattice ionic liquid model (see [33] and references therein). This model consists of two sublattices, where one sublattice is filled with cations (Zr^{4+}) and the other one is filled with anions of O^{2-} and neutral[5] constituents ($\mathrm{AlO}_{1.5}^{0}$). Thus the liquid/amorphous Al_2O_3-ZrO_2 solution phase is described as $(\mathrm{Zr}^{4+})_P(\mathrm{O}^{2-},\mathrm{AlO}_{1.5}^{0})_Q$. P and Q denote the number of sites of the cation and ‘anion/neutral’ sublattices, respectively, which vary with composition to ensure electroneutrality [33]. The Gibbs

---

[5] It is assumed that the bonding in Al_2O_3 has considerable covalent nature [33].

energy of formation of the ternary amorphous oxide phase, $\Delta G_{\text{am-}\left(\text{Zr}^{4+}\text{:O}^{2-}\text{, AlO}^{0}_{1.5}\right)}(T, Y_i)$ can then be expressed as function of the composition by use of the parameter Y_i ($i = \text{Zr}^{4+}, \text{O}^{2-}$, $\text{AlO}^{0}_{1.5}$), which is the fraction of sublattice sites occupied by the species i (for the present system: $Y_{\text{Zr}^{4+}} = 1$, $Y_{\text{O}^{2-}} + Y_{\text{AlO}^{0}_{1.5}} = 1$,[6] $P = 2Y_{\text{O}^{2-}}$ and $Q = 4$). It thus follows that $\Delta G_{\text{am-}\left(\text{Zr}^{4+}\text{:O}^{2-}\text{, AlO}^{0}_{1.5}\right)}(T, Y_i)$, given in Joule per mole of $\left[(\text{Zr}^{4+})_\text{P}\left(\text{O}^{2-}, \text{AlO}^{0}_{1.5}\right)_\text{Q}\right]$, can be calculated according to:

$$\begin{aligned}
&\Delta G_{\text{am-}\left(\text{Zr}^{4+}\text{:O}^{2-}\text{, AlO}^{0}_{1.5}\right)}(T, Y_i) \\
&= P \cdot RT\left(Y_{\text{Zr}^{4+}} \ln Y_{\text{Zr}^{4+}}\right) + Q \cdot RT\left(Y_{\text{O}^{2-}} \ln Y_{\text{O}^{2-}} + Y_{\text{AlO}^{0}_{1.5}} \ln Y_{\text{AlO}^{0}_{1.5}}\right) \\
&+ Y_{\text{Zr}^{4+}} Y_{\text{O}^{2-}} Y_{\text{AlO}^{0}_{1.5}} \left({}^{0}L_{\text{Zr}^{4+}\text{:O}^{2-}\text{, AlO}^{0}_{1.5}} + {}^{1}L_{\text{Zr}^{4+}\text{:O}^{2-}\text{, AlO}^{0}_{1.5}} \left(Y_{\text{O}^{2-}} - Y_{\text{AlO}^{0}_{1.5}}\right)\right),
\end{aligned} \tag{2.1}$$

where ${}^{0}L$ and ${}^{1}L$ are constants of the Redlich-Kister polynomial [30]:

$${}^{0}L_{\text{Zr}^{4+}\text{:O}^{2-}\text{, AlO}^{0}_{1.5}} = 50000 \text{ J/mol}; \; {}^{1}L_{\text{Zr}^{4+}\text{:O}^{2-}\text{, AlO}^{0}_{1.5}} = -40000 \text{ J/mol}.$$

With this model, the Gibbs energy of formation of the liquid/amorphous $\text{AlO}_{1.5}$-ZrO_2 solution phase was calculated at low (supercooled) temperatures. The thus calculated Gibbs energy of formation ΔG (in J/mol-oxygen)[7] curves of the am-$(\text{AlO}_{1.5})_y(\text{ZrO}_2)_{1-y}$ oxide phase as function of the mole fraction of $\text{AlO}_{1.5}$, y, with respect to the Gibbs energies of formation of the pure amorphous oxide components (am-$\text{AlO}_{1.5}$ and am-ZrO_2), are shown in Figure 2.6a for different temperatures in the range of 350 °C – 400 °C. The ΔG curve at 400 °C shows an outspoken minimum at the composition of $y = 0.33$ (i.e. $(\text{AlO}_{1.5})_{0.33}(\text{ZrO}_2)_{0.67}$), which agrees very well with the $\text{Al}^{\text{ox}}/\text{Zr}^{\text{ox}}$-ratio of about 0.5 of the experimentally observed, amorphous $(\text{Al}_{0.33}\text{Zr}_{0.67})\text{O}_{1.83}$ oxide phase, developing at 350 °C - 500 °C (and for am-$\text{Al}_{0.51}\text{Zr}_{0.49}$: developing at 350 °C $\leq T \leq$ 560 °C). Note that a slight dependence of the minimum in the ΔG curves of the am-$(\text{AlO}_{1.5})_y(\text{ZrO}_2)_{1-y}$ oxide phase with temperature can be observed. However, the possibly resulting change in oxide composition, i.e. in the $\text{Al}^{\text{ox}}/\text{Zr}^{\text{ox}}$-ratio, is too small to be experimentally resolved by AES.

---

[6] The site fraction $Y_{\text{O2-}}$ (and thereby $Y_{\text{AlO1.5}}{}^{0}$) is determined by the oxide composition according to: $Y_{\text{O2-}} = 2x_{\text{ZrO2}}/(x_{\text{ZrO2}}+1)$), where x_{ZrO2} is the molar fraction of ZrO_2.

[7] ΔG in J/mole oxygen = [(ΔG in J/mole-$(\text{Zr}^{4+})_\text{P}(\text{O}^{2-}, \text{AlO}_{1.5}{}^{0})_\text{Q}$)]/ $(4Y_{\text{O2-}}+6(1-Y_{\text{O2-}}))$.

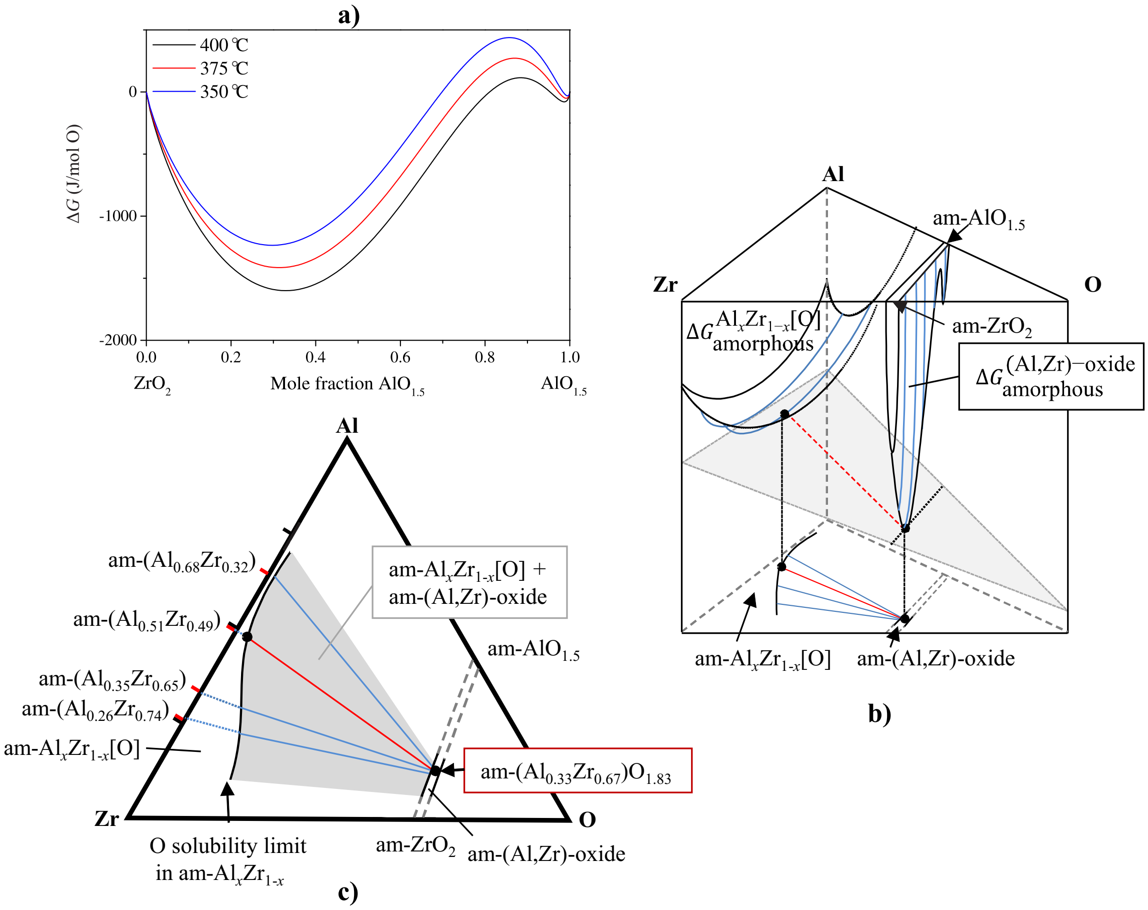

Figure 2.6: a) Gibbs energy of formation for the am-(Al,Zr)-oxide phase at 350 °C, 375 °C and 400 °C, modeled as a (configurationally frozen) homogenous solution of liquid ZrO_2 and liquid Al_2O_3 supercooled to the respective temperature, as calculated by the CALPHAD method. Reference state: liquid ZrO_2 and liquid Al_2O_3. **b)** Schematic illustration of the Gibbs energies of the am-(Al,Zr)-oxide and am-Al_xZr_{1-x}[O] solid solution phases, staying in equilibrium during the oxidation process. **c)** The corresponding ternary phase diagram of Al, Zr and O pertaining to a temperature in the range of 350 °C – 400 °C.

On this basis, the oxidation process of the am-Al_xZr_{1-x} alloys (solid solutions) can be understood as follows: At the onset of oxidation, oxygen dissolves into the amorphous Al_xZr_{1-x} solid solution substrate, forming an am-Al_xZr_{1-x}[O] solid solution phase (see Sec. 2.4.1). As soon as the oxide solubility limit in the alloy solid solution is reached, the am-(Al,Zr)-oxide phase begins to form and a thermodynamic equilibrium is established of the (surrounding, remaining) am-Al_xZr_{1-x}[O] solid solution phase with the am-(Al,Zr)-oxide phase. On the basis of the calculated Gibbs energy of formation ΔG curve of the am-$(AlO_{1.5})_y(ZrO_2)_{1-y}$ phase (Figure 2.6a) and the experimentally determined O solubility limit in am-Al_xZr_{1-x} solid solution substrates (which is strongly dependent on x; cf. Figure 2.4), a three-dimensional representation of the Gibbs energy surfaces $\Delta G^{\text{am-AlZr[O]}}$ and $\Delta G^{\text{am-(Al,Zr)-oxide}}$, for the concurring amorphous Al-Zr alloy phase and amorphous oxide phase, respectively, has been constructed schematically; see Figure 2.6b. The shape of the $\Delta G^{\text{am-AlZr[O]}}$ – surface of the am-Al_xZr_{1-x}[O] solid solution phase is entirely schematic, but representing the wide stability range of the am-Al_xZr_{1-x} solid solution phase and accounting as well for the concentration dependency of the oxygen solubility in the am-Al_xZr_{1-x} solid solution phases. The shape of the $\Delta G^{\text{am-(Al,Zr)-oxide}}$ surface was drawn according to the calculated Gibbs energy of formation ΔG of the am-$(AlO_{1.5})_y(ZrO_2)_{1-y}$ phase and considering the known narrow (almost singular) compositional ranges of the pure (amorphous) oxide phases, Al_2O_3 and ZrO_2. The common-tangent plane, representing the equilibrium state for the coexisting phases, touches both the $\Delta G^{\text{am-AlZr[O]}}$ surface and the $\Delta G^{\text{am-(Al,Zr)-oxide}}$ surface in a single point for each surface. This single point for the $\Delta G^{\text{am-(Al,Zr)-oxide}}$ surface is located close to/at the minimum of the $\Delta G^{\text{am-(Al,Zr)-oxide}}$ surface occurring at a composition of $y = 0.33$ (i.e. $(AlO_{1.5})_{0.33}(ZrO_2)_{0.67}$) at $T = 400$ °C; see the connecting (red, dashed) line in Figure 2.6b, corresponding with the (red, continuous) tie line in Figure 2.6c. The deep minimum at $y = 0.33$ for the Gibbs energy of formation of the am-$(AlO_{1.5})_y(ZrO_2)_{1-y}$ oxide phase (Figure 2.6a), leads to a series of possible equilibria of the am-Al_xZr_{1-x}[O] solution phase of wide compositional range, $0.26 \leq x \leq 0.68$, and the am-$(AlO_{1.5})_y(ZrO_2)_{1-y}$ oxide phase of practically singular composition given by $y = 0.33$: These are represented by the tie-lines in the compositional triangle, shown in Figure 2.6c, which bridge the 'am-Al_xZr_{1-x}[O] solid solution + am-$(AlO_{1.5})_y(ZrO_2)_{1-y}$ oxide' two-phase field in the *metastable* ternary phase diagram (involving only the amorphous phases). As a result, an amorphous $(Al_{0.33}Zr_{0.67})O_{1.83}$ phase forms exclusively during oxidation of am-Al_xZr_{1-x} alloys, regardless of the original am-Al_xZr_{1-x} alloy composition ($0.26 \leq x \leq 0.68$).

2.5 Conclusions

- An amorphous ternary oxide phase with a single, well-defined stoichiometry, *am*-$(Al_{0.33}Zr_{0.67})O_{1.83}$, emerges during thermal oxidation of binary amorphous Al_xZr_{1-x} solid solutions over wide ranges of alloy composition ($0.26 \leq x \leq 0.68$) and oxidation temperature (350 °C – 560 °C).
- The occurrence of an amorphous $(Al_{0.33}Zr_{0.67})O_{1.83}$ oxide phase, rather than the crystalline oxide phases, can be associated with a high nucleation barrier for the crystalline phases(s) owing to relatively high interface energies and/or kinetic

obstruction of the diffusional transport and structural rearrangement required for the development of crystalline compounds (as ZrO_2 and Al_2O_3).

- The practically singular composition of the amorphous oxide phase, $(Al_{0.33}Zr_{0.67})O_{1.83}$, can be explained on a fully thermodynamic basis: Conceiving the amorphous ternary oxide phase as a liquid oxide-oxide solution phase, which is supercooled to low (oxidation) temperatures, the equilibrium of the amorphous solid solution phase and the amorphous oxide phase is realized for a wide range of composition of the solid solution and amorphous oxide phase, $(Al_{0.33}Zr_{0.67})O_{1.83}$, with practically constant composition of the oxide phase as a consequence of the deep minimum of the $\Delta G^{\text{am-(Al,Zr)-oxide}}$ surface, occurring at a composition of $y = 0.33$ (*i.e.* $(AlO_{1.5})_{0.33}(ZrO_2)_{0.67}$).
- This study thus shows the dominant role of thermodynamics in controlling the ternary oxide phase composition, even for the growth of *amorphous* oxides occurring under conditions (far) away from genuine thermodynamic equilibrium for bulk phases.

Acknowledgements

The authors are grateful to Dipl. Ing. F. Thiele for specimen preparation by magnetron sputtering, G. Werner for ICP-OES measurements, Dipl.-Ing. B. Siegle for AES measurements, Dr. W. Sigle, Dipl.-Ing. P. Kopold and Dipl.-Ing. K. Hahn for TEM investigation, M. Wieland for XPS measurements and Dipl.-Ing. H. Göhring for assistance with CALPHAD calculations (all with MPI-IS).

2.6 References

[1] Atkinson A., Rev. Mod. Phys. **57** (1985) 437.

[2] Birks N., Meier G.H., Pettit F.S. Introduction to the High Temperature Oxidation of Metals. Cambridge: Cambridge University Press, 2006.

[3] Shih C.C., Lin S.J., Chung K.H., Chen Y.L., Su Y.Y., J. Biomed. Mater. Res. **52** (2000) 323.

[4] Barquinha P., Martins R., Pereira L., Fortunato E. Transparent Oxide Electronics: From Materials to Devices. Chichester, UK: John Wiley & Sons, 2012.

[5] Leenheer A.J., Perkins J.D., van Hest M.F.A.M., Berry J.J., O'Hayre R.P., Ginley D.S., Phys. Rev. B **77** (2008) 115215.

[6] Nomura K., Ohta H., Takagi A., Kamiya T., Hirano M., Hosono H., Nature **432** (2004) 488.

[7] Fortunato E., Barquinha P., Martins R., Advanced Materials **24** (2012) 2945.

[8] He G., Zhu L., Sun Z., Wan Q., Zhang L., Prog. Mater. Sci. **56** (2011) 475.

[9] Jeurgens L.P.H., Sloof W.G., Tichelaar F.D., Mittemeijer E.J., Phys. Rev. B **62** (2000) 4707.

[10] Reichel F., Jeurgens L.P.H., Mittemeijer E.J., Acta Mater. **56** (2008) 659.

[11] Fehlner F.P., Mott N.F., J. Electrochem. Soc. **117** (1970) 251.

[12] Revesz A.G., Fehlner F.P., Oxid. Met. **15** (1981) 297.

[13] Panda E., Jeurgens L.P.H., Mittemeijer E.J., Surf. Sci. **604** (2010) 588.

[14] Habazaki H., Shimizu K., Skeldon P., Thompson G.E., Wood G.C., Thin Solid Films **300** (1997) 131.

[15] Weller K., Wang Z., Jeurgens L.P.H., Mittemeijer E.J., Acta Mater. **94** (2015) 134.

[16] Vinodh M.S., Jeurgens L.P.H., Surf. Interface Anal. **36** (2004) 1629.

[17] Egerton R.F. Electron Energy-Loss Spectroscopy in the Electron Microscope. New York: Plenum Press, 2011.

[18] Borglund N., Astrand P.G., Csillag S., Microsc. Microanal. **11** (2005) 88.

[19] Weller K., Jeurgens L.P.H., Wang Z.M., Mittemeijer E.J., Acta Mater. **87** (2015) 187.

[20] Bakradze G. unpublished results.

[21] Flötotto D., Wang Z.M., Mittemeijer E.J., Surf. Sci. **633** (2015) 1.

[22] Harmelin M., Fabrichnaya, O. Aluminium-Oxygen-Zirconium: Springer-Verlag Berlin Heidelberg, 2009.

[23] Lyapin A., Jeurgens L.P.H., Graat P.C.J., Mittemeijer E.J., J. Appl. Phys. **96** (2004) 7126.

[24] Panda E., Jeurgens L.P.H., Richter G., Mittemeijer E.J., J. Mater. Res. **25** (2010) 871.

[25] Mittemeijer E.J. Fundamentals of Materials Science: The Microstructure–Property Relationship Using Metals as Model Systems. Berlin Heidelberg: Springer-Verlag, 2010.

[26] Stevens R. An Introduction to Zirconia. Twickenham UK: Magnesium Elektron Limited, 1986.

[27] Stevens R. Zirconia and Zirconia Ceramics: Magnesium Elektron Limited, 1986.

[28] Lukas H.L., Fries S.G., Sundman B. Computational thermodynamics: the Calphad method. Cambridge: Cambridge University Press, 2007.

[29] Bormann R., Gartner F., Zoltzer K., Journal of the Less-Common Metals **145** (1988) 19.

[30] Fabrichnaya O., Aldinger F., Z. Metallk. **95** (2004) 27.

[31] Dorner P., Gauckler L.J., Krieg H., Lukas H.L., Petzow G., Weiss J., Calphad-Comput. Coupling Ph. Diagrams Thermochem. **3** (1979) 241.

[32] Ball R.G.J., Mignanelli M.A., Barry T.I., Gisby J.A., J. Nucl. Mater. **201** (1993) 238.

[33] Hillert M., J. Alloy. Compd. **320** (2001) 161.

Chapter 3

Oxidation kinetics of amorphous Al_xZr_{1-x} alloys

K. Weller, Z. M. Wang, L. P. H. Jeurgens and E. J. Mittemeijer

Abstract

The oxidation kinetics of amorphous Al_xZr_{1-x} alloys (solid solution) has been studied as function of the alloy composition ($0.26 \leq x \leq 0.68$) and the oxidation temperature (350 °C $\leq T \leq$ 400 °C; at constant $pO_2 = 1 \times 10^5$ Pa) by a combinatorial approach using spectroscopic ellipsometry (SE), Auger electron spectroscopy (AES) depth profiling, transmission electron microscopy (TEM) and X-ray diffraction (XRD) analysis. Thermal oxidation of the am-Al_xZr_{1-x} alloys results in the formation of an amorphous oxide overgrowth with a thermodynamically preferred singular composition, corresponding to a constant Al^{ox}/Zr^{ox} ratio of 0.5. Both the solubility and the diffusivity of oxygen in the am-Al_xZr_{1-x} alloy substrate increase considerably with increasing Zr content, in particular for Zr contents above 49 at.% Zr. Strikingly, the oxidation kinetics exhibit a transition from parabolic oxide growth kinetics for Al-rich am-Al_xZr_{1-x} alloys ($x \geq 0.51$) to linear oxide growth kinetics for Zr-rich am-Al_xZr_{1-x} alloys ($x < 0.35$). The underlying oxidation mechanism is discussed. It is concluded that the oxidation kinetics of the amorphous Al_xZr_{1-x} alloys for $0.26 \leq x \leq 0.68$ and 350 °C $\leq T \leq$ 400 °C are governed by: (*i*) the atomic mobilities of O and Al in the alloy substrate at the reacting oxide/alloy interface, (*ii*) the solubility of O in the substrate and (*iii*) the compositional constraint due to the thermodynamically preferred formation of an amorphous oxide phase of singular composition.

3.1 Introduction

It has long been recognized that the properties of metals and alloys (e.g. corrosion resistance, electrical conductivity, adhesion) are strongly influenced by the presence of the surficial oxide layer, which forms naturally on metallic surfaces in an oxidizing gaseous or liquid environment. Functional properties of metal-based components and devices can thus be optimized by controlled (pre-)oxidation as a function of e.g. the alloy composition, the oxidation temperature (T), the oxidation time (t) and the oxygen partial pressure (pO_2). Such fine-tuning of the microstructure and thus properties of oxide overgrowths requires fundamental understanding of the underlying oxidation mechanism [1-4]. Whereas the oxidation behavior of *crystalline* metallic materials has been investigated extensively [5-7], the oxidation behavior of *amorphous* metallic materials has received much less attention and, consequently, a thorough understanding of the oxidation mechanisms of amorphous metallic alloys lacks, despite the increasing interest in and many potential applications of such amorphous metallic materials.

Zr-based bulk metallic glasses have gained significant interest in recent years, as they possess good corrosion resistance, high elastic strain limit, high strength and good biocompatibility [8, 9]. In order to predict and improve their long-term reliability in real-life applications, it is essential to investigate and understand their long-term stability under realistic conditions, often involving an oxidizing environment. Up to date, only few studies [10-12] have been devoted to the oxidation of *amorphous* Al_xZr_{1-x} alloys, which have mainly focused on the developing *oxide microstructure*. For example, the complete transformation of the amorphous alloy layer into an amorphous oxide phase has been reported for the thermal oxidation of 150 nm thick amorphous Al_xZr_{1-x} alloy layers (x = 0.293 – 0.62) up to 700 °C [10]. The formation of an amorphous (Al,Zr)-oxide overgrowth for the thermal oxidation of amorphous Al_xZr_{1-x} alloys over a wide compositional range of x = 0.26 – 0.68 and oxidation temperatures up to 500 °C was also evidenced in Ref. [11]. The amorphous state of the thickening oxide overgrowth was fully preserved at elevated temperatures up to 500 ºC and for very thick oxide layers (exceeding 300 nm) due to favorable interface energies of the amorphous oxide with the am-Al_xZr_{1-x} alloy substrate and a kinetic constraint for the formation of the crystalline (Al_2O_3 and/or ZrO_2) oxide phases. Strikingly, the amorphous (Al,Zr)-oxide overgrowth has a single homogeneous composition $(Al_{0.33}Zr_{0.67})O_{1.83}$, independent of the parent am-Al_xZr_{1-x} alloy composition ($0.26 \leq x \leq 0.68$) and the applied oxidation temperature [11]. This recent experimental finding was found to have a thermodynamic origin, as supported by thermodynamic model calculations, treating the amorphous (Al,Zr)-oxide phase as an undercooled liquid oxide-oxide (Al_2O_3-ZrO_2) solution phase [11].

Up to date, the *oxidation kinetics* of am-Al_xZr_{1-x} alloys as a function of alloy composition and oxidation temperature has not yet been reported. The present study addresses the growth kinetics of the amorphous (Al,Zr)-oxide layer of singular composition, as developing on amorphous Al_xZr_{1-x} (am-Al_xZr_{1-x}) alloy substrates (solid solution) over the compositional range of $0.26 \leq x \leq 0.68$ at various oxidation temperatures in the range of 350 °C – 400 °C (all at a constant partial oxygen pressure of $pO_2 = 1\times10^5$ Pa). To this end, the oxide-layer growth kinetics were established by ex-situ spectroscopic ellipsometry (SE). In addition, to elucidate the underlying oxidation mechanism, the compositional changes in the parent alloy adjacent to the oxide/alloy interface due to (*i*) the dissolution and diffusion of oxygen into the amorphous alloy and (*ii*) the preferred oxidation of Al or Zr (depending on the bulk alloy composition) has been investigated by Auger electron spectroscopy (AES) depth profiling analyses. The investigations demonstrate a strong dependence of the oxidation kinetics on the am-Al_xZr_{1-x} alloy composition.

3.2 Experimental procedures and data evaluation

3.2.1 Specimen preparation

Si(100) wafers, covered with a 50 nm-thick am-SiO_2 bottom layer and a 50 nm-thick am-Si_3N_4 top layer, were employed as substrates. The Si wafer substrates were introduced into a vacuum chamber for magnetron sputtering (base pressure < 5×10^{-8} mbar) and subsequently sputter-cleaned by Ar^+ plasma treatment for 1 minute, applying an acceleration voltage of 105 V. Next amorphous Al_xZr_{1-x} coatings (thickness 2 µm) were deposited at room temperature (RT) by co-sputtering from elemental targets of Al (99.9995 wt.%) and Zr (98.5 wt.%). Amorphous Al_xZr_{1-x} coatings of different compositions were obtained by maintaining a constant power of 100 W on the Zr target and a constant equilibrium Ar gas pressure of 5×10^{-3} mbar, while varying the power on the Al target (P_{Al}) in the range of 20 W – 144 W; i.e. am-$Al_{0.26}Zr_{0.74}$ for P_{Al} = 20 W, am-$Al_{0.35}Zr_{0.65}$ for P_{Al} = 28 W, am-$Al_{0.51}Zr_{0.49}$ for P_{Al} = 53 W and am-$Al_{0.68}Zr_{0.32}$ for P_{Al} = 101 W. The denoted coating compositions were determined by inductively coupled plasma optical emission spectrometry (ICP-OES). For further details, see Ref. [11].

3.2.2 Oxidation

The as-deposited am-Al_xZr_{1-x} specimens were cut into small pieces (lateral dimensions: 7×14 mm^2) and enclosed in quartz ampoules. To ensure identical oxidation conditions, each quartz ampoule always contained a set of four different am-Al_xZr_{1-x} specimens, i.e.

one of each alloy composition (see Sec. 3.2.1). The ampoules were firstly evacuated and then filled with pure oxygen up to a partial pressure of pO_2 = 4.70×10^4 Pa at room temperature (RT), which corresponds to 10^5 Pa at the oxidation temperature of 350 °C. Next the sealed ampoules were introduced into a pre-heated sandbath (TECHNE FB-08c) at 350 °C and isothermally treated for various oxidation times (t_{ox} = 1, 2.5, 5, 7.5 and 10 h).[1] After reaching the targeted oxidation time, the ampoules were removed from the sand bath and immediately quenched in water (T ~ 18 °C). Analogously, additional series of oxidation experiments were performed at the same pO_2 (= 10^5 Pa), but at different oxidation temperatures of T_{ox} = 375 °C ($p_{\mathrm{O_2}}$ = 4.52×10^4 Pa at RT), 400 °C ($p_{\mathrm{O_2}}$ = 4.35×10^4 Pa at RT) and 500 °C ($p_{\mathrm{O_2}}$ = 3.79×10^4 Pa at RT). For the determination of the oxidation kinetics, only experimental results in the temperature range 350 °C – 400 °C were taken into account. Prolonged oxidation at an oxidation temperature of 500 °C leads to the development of crystalline intermetallic phases from the am-Al_xZr_{1-x} alloys with x = 0.26, 0.35 and 0.68; only the am-$Al_{0.51}Zr_{0.49}$ alloy is thermally stable (i.e. remains fully amorphous) up to 500 °C [11, 13]. Nonetheless, for short oxidation times at 500 °C (up to 1 h), the fraction of transformed am-Al_xZr_{1-x} is small enough to not affect the oxidation process and therefore these specimens could be used to determine the interfacial oxygen concentration in the am-Al_xZr_{1-x} alloys at 500 °C.

3.2.3 Microstructural analysis and data evaluation

TEM analysis was applied to determine the microstructure of the oxidized am-Al_xZr_{1-x} alloys. To this end, cross-sectional TEM lamellae were prepared according to the procedure described in Ref. [12] and investigated using a JEOL JEM-ARM200F scanning transmission electron microscope operated at 200 kV.

The elemental depth-distributions in the as-deposited and oxidized am-Al_xZr_{1-x} alloys were investigated by AES sputter-depth profiling using a JEOL JAMP 7830F Scanning Auger Microscope, according to the measurement and quantification procedures, as described in Ref. [11]. The sputter depth was calibrated on the basis of the established am-Al_xZr_{1-x} coating thicknesses (as measured by a DekTak 8 profilometer) and the known oxide-layer thicknesses (as determined by SE; see below).

To trace the change of oxide-film thickness with time at constant oxidation temperature the oxidized am-Al_xZr_{1-x} specimens were analyzed using a J.A. Woollam

---

[1] Oxidation of am-$Al_{0.26}Zr_{0.74}$ has also been performed for an oxidation time of 0.5 h.

M-2000™ spectroscopic ellipsometer equipped with a Xe light source (wavelength $\lambda = 300$ nm – 850 nm). To this end, the ellipsometric values $\Psi(\lambda, \varphi)$ and $\Delta(\lambda, \varphi)$ (see footnote 2) were recorded ex-situ from the as-prepared and the oxidized am-Al_xZr_{1-x} specimens at variable angles of incidence of $\varphi = 60°$, 65°, 70° and 75° (with respect to the specimen-surface normal). Next the oxide-layer thickness for each oxidized am-Al_xZr_{1-x} alloy substrate was determined by linear-least squares fitting of sets of calculated spectra of $\Psi(\lambda, \varphi)$ and $\Delta(\lambda, \varphi)$ to the measured ones using the WVASE32 software package (version 3.770) as follows.

$\Psi(\lambda, \varphi)$ and $\Delta(\lambda, \varphi)$ spectra were calculated (for each alloy composition and oxide-layer thickness) by adopting a model description for the evolving substrate/film system, constituted of an am-Al_xZr_{1-x} alloy substrate, an oxide overgrowth of uniform thickness L_{ox} and a relatively thin interfacial sublayer of uniform thickness L_{EMA} between the oxide layer and the substrate (as introduced to account for interfacial mixing effects; see below). The optical constants (i.e. the refractive index, $n(\lambda)$ and the extinction coefficient, $k(\lambda)$) of the bulk am-Al_xZr_{1-x} substrates were directly obtained from the recorded $\Psi(\lambda, \varphi)$ and $\Delta(\lambda, \varphi)$ spectra of either the as-prepared alloy before oxidation or the oxidized alloy after removal of the oxide overgrowth (see below). The oxide overgrowths were optically transparent over the investigated wavelength range (i.e. $k(\lambda) \approx 0$) and thus the wavelength-dependence of the optical constants of the oxide overgrowth could be approximated by a Cauchy function $n(\lambda) = \mathrm{A}+\mathrm{B}/\lambda^2$, where A and B are the so-called Cauchy coefficients. The optical properties of the interfacial sublayer were estimated from the optical constants of the alloy substrate and the top oxide layer using the Bruggeman effective medium approximation (EMA), thus accounting for various ‘mixing’ effects at the interface, such as interface roughness, compositional gradients and/or phase mixing (cf. Ref. [14]): the corresponding fraction of the oxide in the interfacial sublayer is further denoted as f_{EMA}.

For each alloy composition and oxidation temperature, the measured spectra of $\Psi(\lambda, \varphi)$ and $\Delta(\lambda, \varphi)$ pertaining to different oxidation times were simultaneously fitted, while introducing the thicknesses L_{ox}, L_{EMA} and f_{EMA}, as well as single values of the

---

[2] The ellipsometric parameters Ψ and Δ describe the amplitude ratio and the phase difference of the p-(parallel to the plane of incidence) and s-(perpendicular to the plane of incidence)polarized components of the light beam before and after reflection, respectively.

Cauchy coefficients (A and B) as fit parameters. The resulting total oxide-layer thickness d_{ox} of each specimen was taken as $d_{ox} = L_{ox} + f_{EMA} \cdot L_{EMA}$.

As demonstrated by a parameter study, the optical constants of the oxidized am-$Al_{0.68}Zr_{0.32}$ and $Al_{0.51}Zr_{0.49}$ substrates (i.e. the am-Al_xZr_{1-x} alloys with the lowest Zr content), to a first approximation, can be taken constant and equal to the bulk optical constants of the alloy as determined prior to oxidation (see above). In the fitting procedure, any possible changes in the optical constants of the am-$Al_{0.68}Zr_{0.32}$ and $Al_{0.51}Zr_{0.49}$ substrates by oxidation-induced compositional changes are thus accounted for only by the introduced interfacial EMA layer. The Zr-rich am-$Al_{0.35}Zr_{0.65}$ and am-$Al_{0.26}Zr_{0.74}$ alloy substrates exhibit a pronounced change in their optical constants with time due to the extensive dissolution of O into the alloy substrate upon oxidation (up to 20 at.% [O]) (cf. Section 3.3.2). Therefore, such a first order approximation could not be applied for the evaluation of the recorded SE data of the oxidized alloy substrates of higher Zr content. Hence in the fitting procedure, the optical constants of the Zr-rich am-$Al_{0.35}Zr_{0.65}$ and am-$Al_{0.26}Zr_{0.74}$ alloy substrates were employed as derived from the recorded $\Psi(\lambda, \varphi)$ and $\Delta(\lambda, \varphi)$ spectra of the O-saturated am-$Al_{0.35}Zr_{0.65}$ and am-$Al_{0.26}Zr_{0.74}$ alloy substrates after removal of the oxide overgrowth. To this end, the am-$Al_{0.35}Zr_{0.65}$ and am-$Al_{0.26}Zr_{0.74}$ alloys were oxidized for 5 h at 375 °C (thus containing a considerable amount of dissolved oxygen in the alloy substrate, further designated as am-Al_xZr_{1-x}[O]) and subsequently sputter-cleaned at RT to remove completely the amorphous oxide overgrowth. Sputter-cleaning was performed in an ultra-high vacuum chamber (base pressure < $3 \cdot 10^{-8}$ Pa) using a focused 3 kV Ar^+ ion beam scanning over the specimen surface, while monitoring the layer-by-layer removal of the oxide overgrowth by *in vacuo* X-ray photoelectron spectroscopy (XPS) (for conditions, see Ref. [11]). The sputter cleaning treatment was interrupted as soon as the oxidic Al and Zr components could no longer be detected by XPS (and thus only a dissolved O 1s component remained). Next the optical constants of the O-saturated am-$Al_{0.35}Zr_{0.65}$ and am-$Al_{0.26}Zr_{0.74}$ alloys were obtained from the recorded $\Psi(\lambda, \varphi)$ and $\Delta(\lambda, \varphi)$ of these sputter-cleaned specimens.

3.3 Results

3.3.1 Microstructure and composition of oxidized am-Al_xZr_{1-x} alloys

The microstructures of the am-Al_xZr_{1-x} alloy substrates (x = 0.26, 0.35, 0.51, 0.68) and their oxide overgrowths after oxidation for 10 h at 400 °C were investigated by XRD and cross-sectional TEM. Neither the formation of a crystalline oxide phase nor the formation of a crystalline intermetallic Al-Zr phase was observed upon oxidation of the am-Al_xZr_{1-x} alloys up to 400 °C by XRD (cf. Fig. 1 in Ref [11]). A bright-field cross-sectional TEM micrograph of the oxidized (at 400 °C for 10 h) am-$Al_{0.51}Zr_{0.49}$ alloy and a corresponding selected-area electron diffraction pattern (SADP) are shown in Figure 3.1a and b, respectively: the TEM analysis confirms the amorphous state of the am-$Al_{0.51}Zr_{0.49}$ alloy and the amorphous oxide overgrowth after prolonged oxidation. Note the uniformity of the amorphous oxide-overgrowth layer thickness (see Figure 3.1a).

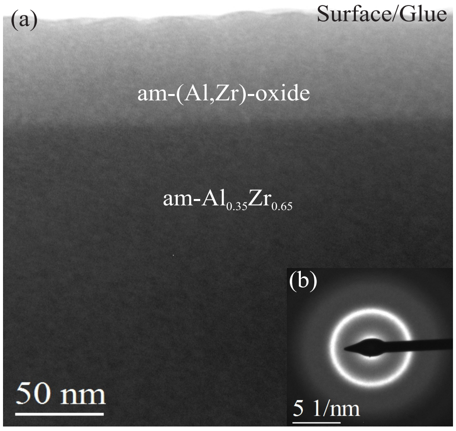

Figure 3.1: **a)** Cross-sectional bright-field TEM micrograph of an am-$Al_{0.51}Zr_{0.49}$ alloy oxidized at 400 °C for 10 h. The oxide overgrowth on the am-$Al_{0.51}Zr_{0.49}$ substrate is amorphous. **b)** A selective area diffraction pattern (SADP), taken with an aperture of diameter ~ 130 nm at a region that contains both the oxide layer and the underlying substrate, confirming the amorphous nature of both the oxide overgrowth and the oxidized alloy.

As shown by AES compositional sputter-depth profiling, the amorphous oxide overgrowths on the am-Al_xZr_{1-x} alloys have incorporated both Al and Zr from the alloy (further designated as Al^{ox} and Zr^{ox}). Strikingly, the composition of the oxide overgrowths is nearly constant, exhibiting a constant Al^{ox}/Zr^{ox} ratio of about 0.5 [i.e. $(AlO_{1.5})_{0.33}(ZrO_2)_{0.67}$], independent of both the Al/Zr ratio in the parent am-Al_xZr_{1-x}

alloy (for $0.26 \leq x \leq 0.68$) and the oxidation temperature in the range of 350 °C $\leq T \leq$ 500 °C: see Figure 3.2, the discussion in Sec. 3.4 and Ref. [11]. For am-Al_xZr_{1-x} alloys with $x = 0.35$ (Figure 3.2c) and, in particular, for $x = 0.51$ (Figure 3.2b), a pile-up of Al at the oxide/alloy interface occurs, which is discussed in Sec. 3.4.

3.3.2 Oxygen solubility and diffusivity in am-Al_xZr_{1-x} alloys

As indicated by the AES sputter-depth profiling analyses (see Figure 3.2), oxygen has dissolved and diffused into the alloy substrate upon oxidation. The dissolved oxygen content in the interior of the am-Al_xZr_{1-x} alloy substrate, as marked with red arrows in Figure 3.2a-d, increases with increasing Zr content in the alloy. It is taken for granted that, apart from the (very) beginning stage of oxide-layer growth [15, 16], the oxygen concentration as established in the alloy substrate adjacent to the oxide/alloy interface is determined by a local equilibrium.[3] Indeed it was found that the interfacial O concentration in the alloy substrate for each alloy composition has attained a practically constant value for oxidation times ≥ 1 h for am-Al_xZr_{1-x} with $x = 0.51$ and 0.65 (and ≥ 0.5 h for am-$Al_{0.26}Zr_{0.74}$) at T = 350 – 400 °C (cf. Figure 3.5). The interfacial O concentrations in the alloy substrates for various oxidation times (up to 10 h) for the various alloy compositions and oxidation temperatures were deduced from the measured AES sputter-depth profiles of the oxidized alloys (see Figure 3.2) by determining[4] the O concentrations in the alloy at the depth position below the surface where both the oxidic Zr concentration and the oxidic Al concentration drop below 0.5 at.%.

---

[3] It is assumed that a local equilibrium prevails at the solid-solid oxide/amorphous alloy interface, i.e. this implies constancy of the O concentration in the am-Al_xZr_{1-x} alloy substrate *at* the inward moving oxide/amorphous alloy interface [16, 17].

[4] The O-concentration values at the interface, presented in Figure 3.3, are averages over 5 consecutive O-concentration values of the measured sputter-depth profiles in order to reduce the error caused by AES depth-profile broadening effects due to e.g. preferential sputtering or interface roughness [18, 19].

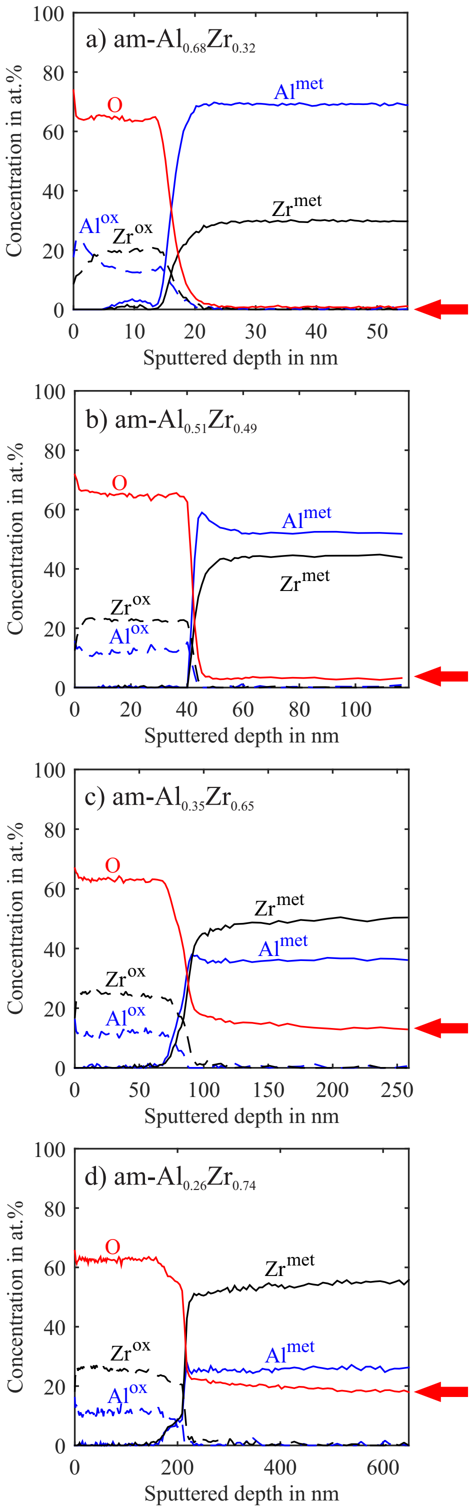

Figure 3.2: AES concentration depth profiles of am-Al$_x$Zr$_{1-x}$ alloy substrates with x = **a)** 0.68, **b)** 0.51, **c)** 0.35 and **d)** 0.26 oxidized at 400 °C for 10 h. Note that the oxygen solubility in the am-Al$_x$Zr$_{1-x}$ alloy substrate increases (red arrow) with increasing Zr concentration in the am-Al$_x$Zr$_{1-x}$ solid solution (see red arrows).

The thus obtained interfacial O concentrations (for oxidation times ≥ 1 h) have been plotted as function of the Zr concentration in the am-Al_xZr_{1-x} alloy substrate and as function of the oxidation temperature in the range of 350 – 500 °C (500 °C -560 °C for am-$Al_{0.44}Zr_{0.56}$ [12]) in Figure 3.3a and b, respectively. Strikingly, no distinct temperature dependency of the interfacial O concentration in the am-Al_xZr_{1-x} alloy substrates is observable in the investigated temperature range. Therefore, an average interfacial O concentration, calculated from the interfacial O concentration values obtained at different temperatures as shown in Figure 3.3, was obtained for the investigated am-Al_xZr_{1-x} alloy compositions: 1.3 ± 0.2 at.% for am-$Al_{0.68}Zr_{0.32}$, 2.9 ± 0.7 at.% for am-$Al_{0.51}Zr_{0.49}$, 15.0 ± 1.2 at.% for am-$Al_{0.35}Zr_{0.65}$ and 19.8 ± 1.1 at.% for am-$Al_{0.26}Zr_{0.74.}$ It follows that the interfacial O concentration is relative low (1-3 at.%) for the am-$Al_{0.68}Zr_{0.32}$ and am-$Al_{0.51}Zr_{0.49}$ alloys and that it abruptly increases approximately linearly with increasing Zr content for Zr contents exceeding 49 at.%.

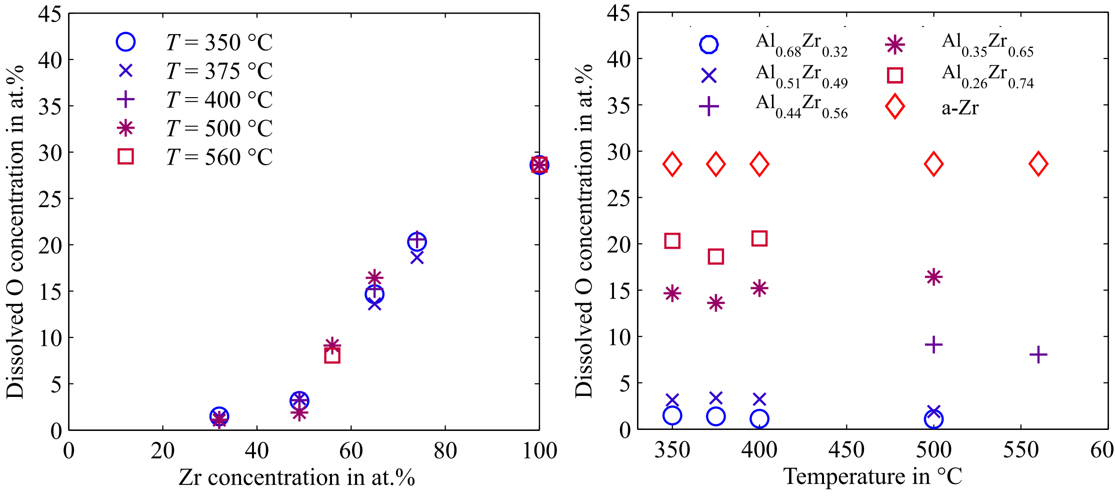

(a) (b)

Figure 3.3: Dissolved oxygen concentration of oxidized am-Al_xZr_{1-x} alloys (directly in front of the oxide/alloy interface) as a function of **(a)** the Zr concentration in the alloys and **(b)** the oxidation temperature. The corresponding data for pure Zr [20] have also been indicated. The corresponding oxidation times are: 10 h (350 °C – 400 °C) and 1 h (500 °C) for am-Al_xZr_{1-x} (x = 0.26, 0.35, 0.51, 0.68); 3 h (500 °C) and 1 h (560 °C) for am-Al_xZr_{1-x} (x = 0.44); see Ref. [12]. Note that the error bars are smaller than the size of the symbols.

With increasing oxidation time (in the present study up to 10 h), the continuous inward diffusion of oxygen from the reacting oxide/alloy interface into the alloy causes the oxygen diffusion zone to progressively extend into the interior of the am-$\mathrm{Al}_x\mathrm{Zr}_{1\text{-}x}$ alloy substrate. The oxygen diffusion within the am-$\mathrm{Al}_x\mathrm{Zr}_{1\text{-}x}$ is governed by Fick's second law,

$$\frac{\partial c_{\mathrm{O}}^{\text{am-Al}_x\text{Zr}_{1\text{-}x}}}{\partial t} = D_{\mathrm{O}}^{\text{am-Al}_x\text{Zr}_{1\text{-}x}} \frac{\partial^2 c_{\mathrm{O}}^{\text{am-Al}_x\text{Zr}_{1\text{-}x}}}{\partial l^2}, \tag{3.1}$$

where $D_{\mathrm{O}}^{\text{am-Al}_x\text{Zr}_{1\text{-}x}}$ is the diffusion coefficient of oxygen in the am-$\mathrm{Al}_x\mathrm{Zr}_{1\text{-}x}$ alloy substrate (assumed to be concentration independent), t is the diffusion/oxidation time and $c_{\mathrm{O}}^{\text{am-Al}_x\text{Zr}_{1\text{-}x}}$ is the oxygen concentration at depth l below the oxide/alloy interface/boundary plane (where $l = 0$). Due to consumption of the am-$\mathrm{Al}_x\mathrm{Zr}_{1\text{-}x}$ alloy substrate by the growing oxide layer, the oxide/alloy interface boundary plane actually moves inwardly with progressing oxidation time, which is not taken into account by Eq. (3.1). However, the growth of the oxide layer is much slower than growth of the extent of the O diffusion zone in the am-$\mathrm{Al}_x\mathrm{Zr}_{1\text{-}x}$ alloy substrate (cf. Figure 3.4). Hence, the movement of the oxide/alloy interface/boundary plane can be neglected (cf. Ref [21]). Furthermore, it is assumed by use of Eq. (3.1) that the diffusion of oxygen does not depend on the concentration gradients of Al and Zr in the alloy (adjacent to the interface).

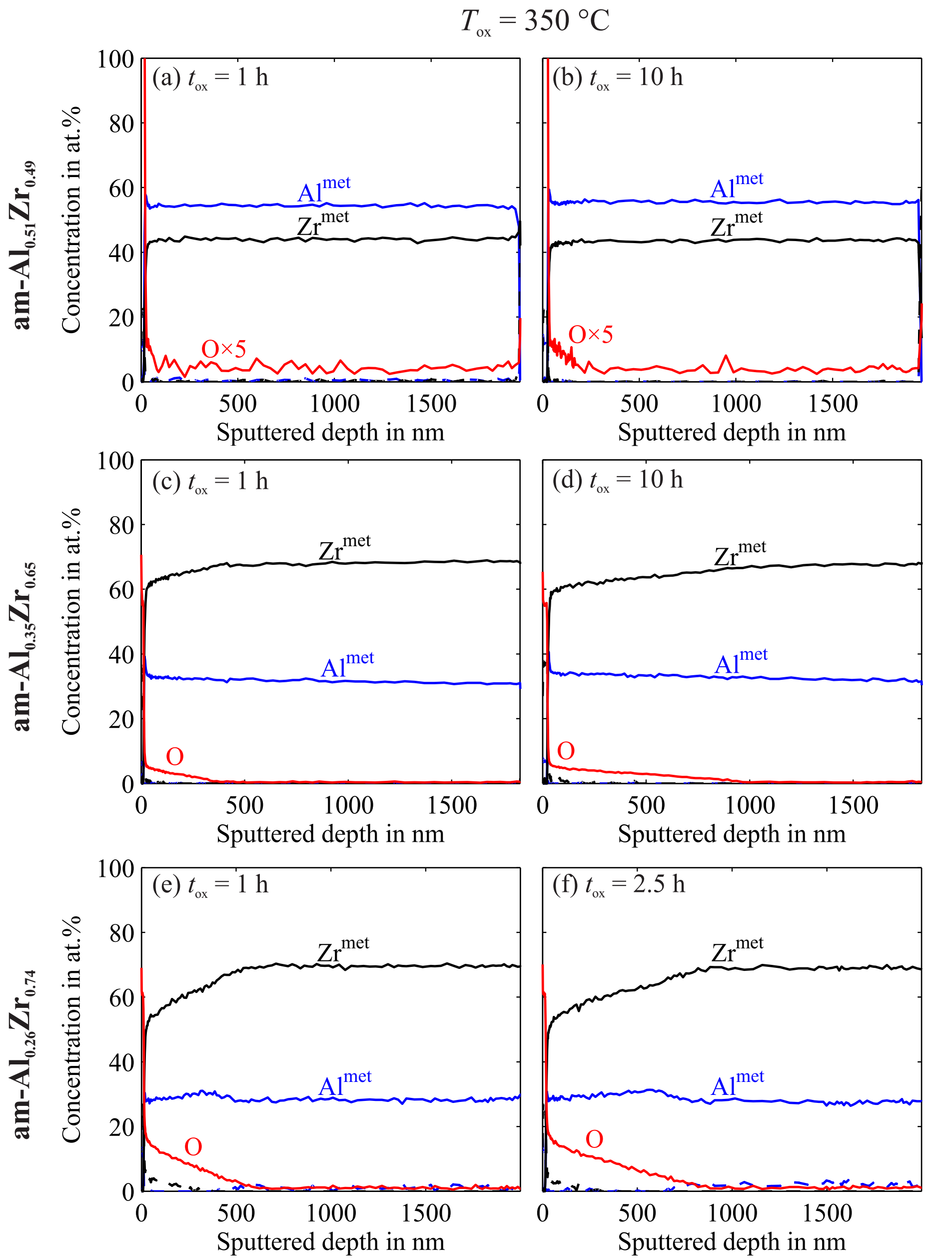

Figure 3.4: AES concentration-depth profiles of am-Al$_x$Zr$_{1-x}$ substrates oxidized at 350 °C: am-Al$_{0.51}$Zr$_{0.49}$ for **a)** 1 h and **b)** 10 h, am-Al$_{0.35}$Zr$_{0.65}$ for **c)** 1 h and **d)** 10 h, am-Al$_{0.26}$Zr$_{0.74}$ for **e)** 1 h and **f)** 2.5 h.

The diffusion coefficient of oxygen in the am-Al$_x$Zr$_{1-x}$ alloy can now be estimated for each alloy composition and oxidation temperature from the evolution of the respective concentration-depth profile of dissolved oxygen in the alloy substrate, $c_{\mathrm{O}}^{\text{am-Al}_x\text{Zr}_{1-x}}(l,t)$, for different oxidation times and oxidation temperatures, as measured by AES sputter-depth profiling (cf. Figure 3.4). To this end, modeling of the oxygen concentration profile was performed on the basis of Eq. (3.1), assuming a semi-infinite solid-solution alloy matrix and applying the following boundary conditions:

$$c_{\mathrm{O}}^{\text{am-Al}_x\text{Zr}_{1\text{-}x}}(l,t)\Big|_{l=0,t>0} = c_{\mathrm{O}}^{\mathrm{i}}, \tag{3.2}$$

$$c_{\mathrm{O}}^{\text{am-Al}_x\text{Zr}_{1\text{-}x}}\Big|_{l>0,t=0} = c_{\mathrm{O}}^{0}, \tag{3.3}$$

where $c_{\mathrm{O}}^{\mathrm{i}}$ represents the interfacial O concentration in the alloy at depth $l = 0$, i.e. the oxide/alloy boundary plane, and c_{O}^{0} represents the initial oxygen concentration in the alloy at depth l, which is $c_{\mathrm{O}}^{0} = 0$ (see footnote 5). The solution of Fick's second law (Eq. (3.1)), applying the above boundary conditions, is given by

$$c_{\mathrm{O}}^{\text{am-Al}_x\text{Zr}_{1\text{-}x}}(l,t) = c_{\mathrm{O}}^{\mathrm{i}} \cdot \left[1 - \mathrm{erf}\left(l \times \left\{2\sqrt{D_{\mathrm{O}}^{\text{am-Al}_x\text{Zr}_{1\text{-}x}} \cdot t}\right\}^{-1}\right)\right]. \tag{3.4}$$

The temperature dependence of $D_{\mathrm{O}}^{\text{am-Al}_x\text{Zr}_{1\text{-}x}}$ satisfies

$$D_{\mathrm{O}}^{\text{am-Al}_x\text{Zr}_{1\text{-}x}} = D_0 \cdot \exp\left(-\frac{Q}{\mathrm{R} \cdot T}\right), \tag{3.5}$$

where D_0 is the pre-exponential factor, Q the activation energy for oxygen diffusion and R the gas constant. For each alloy composition (x = 0.51, 0.35, 0.26), linear least squares fitting of the measured and calculated (using Eq. (3.4)) O diffusion profiles was performed for each alloy-substrate composition *simultaneously* on the entire set of measured oxygen diffusion profiles for different oxidation times and different temperatures, adopting $c_{\mathrm{O}}^{\mathrm{i}}$, D_0 and Q (all independent of T) as fitting parameters. The result of the fitting procedure for am-$Al_{0.51}Zr_{0.49}$, am-$Al_{0.35}Zr_{0.65}$ and am-$Al_{0.26}Zr_{0.74}$ is shown in Figure 3.5. Differences of the measured and the modeled oxygen concentration-depth profiles can originate from (*i*) inaccuracy of the oxygen concentrations as determined by the quantification of the AES data using experimentally-determined sensitivity factors, and/or (*ii*) (small) deviation of the real diffusion behavior of oxygen in am-Al_xZr_{1-x} alloys to that assumed in the applied (idealized) model. For the am-$Al_{0.68}Zr_{0.32}$ a comparable investigation of the oxygen diffusion in the am-Al_xZr_{1-x} alloy matrix was not possible due to a too low O solubility in the am-Al_xZr_{1-x} alloy matrix (cf. Figure 3.3).

---

[5] Any residual oxygen signal recorded in the am-Al_xZr_{1-x} solid solution at the very end of each AES depth profile was subtracted from the measured oxygen-diffusion profile.

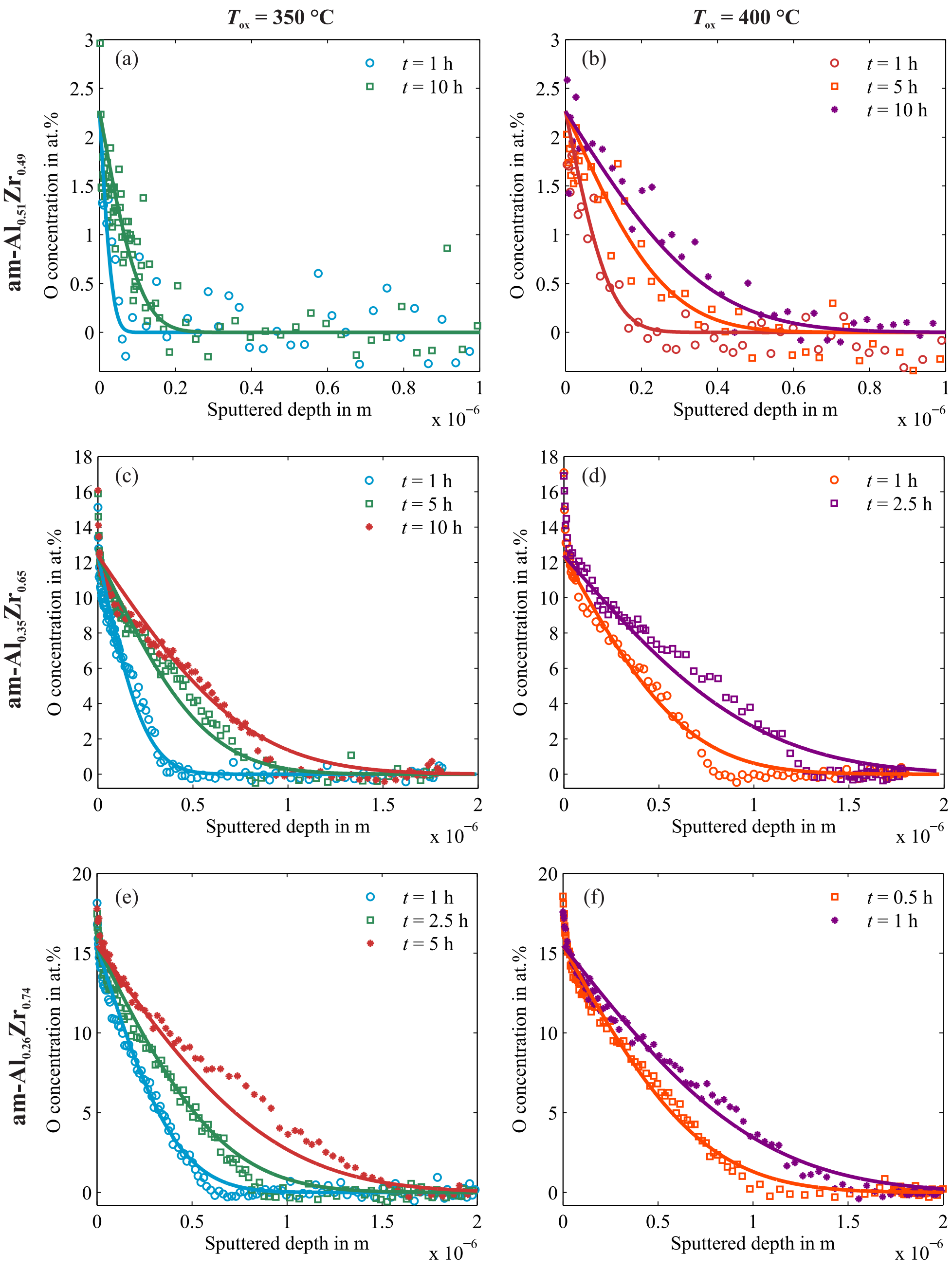

Figure 3.5: Oxygen diffusion profiles (experimental data (points) and fitted model (lines; cf. Equation (3.4))) of: am-$Al_{0.51}Zr_{0.49}$ oxidized at **(a)** 350 °C for 1 h and 10 h and **(b)** 400 °C for 1 h, 5 h and 10 h; am-$Al_{0.35}Zr_{0.65}$ oxidized at **(c)** 350 °C for 1 h, 5 h and 10 h and **(d)** 400 °C for 1 h and 2.5 h; am-$Al_{0.26}Zr_{0.74}$ oxidized at **(e)** 350 °C for 1 h, 2.5 h and 5 h and **(f)** 400 °C for 0.5 h and 1 h. All profiles of one concentration were fitted simultaneously for both temperatures, which resulted in values for the activation energy Q, the pre-exponential factor D_0 and the interfacial oxygen concentration c_O^i listed in Table 3.1. The sputtered depth indicates the distance from the oxide/alloy interface.

The determined values of c_i, D_0, Q and the accordingly calculated values of $D_O^{\text{am-Al}_x\text{Zr}_{1-x}}$ at 350 °C and 400 °C for the oxidized am-$Al_{0.51}Zr_{0.49}$, am-$Al_{0.35}Zr_{0.65}$ and am-$Al_{0.26}Zr_{0.74}$ alloys, as well as the corresponding values for pure, crystalline (α-)Zr [20], have been collected in Table 3.1. For am-$Al_{0.51}Zr_{0.49}$, the interfacial O concentration c_O^i = 2.3 at.%, as obtained by the fitting procedure, agrees well with the experimental estimate for the O concentration in the alloy at the oxide/alloy interface, which is 2.9 ± 0.7 at.% (see beginning of this subsection). The interfacial O concentrations for am-$Al_{0.35}Zr_{0.65}$ and am-$Al_{0.26}Zr_{0.74}$ (12.4 at.% and 15.5 at.%, respectively) show a stronger deviation from the experimentally-determined interfacial O concentrations (15.0 ± 1.2 at.% for am-$Al_{0.35}Zr_{0.65}$ and 19.8 ± 1.1 at.% for am-$Al_{0.26}Zr_{0.74}$). The experimentally-determined interfacial O concentrations (see above) might differ from the interfacial O concentrations, as obtained by the fitting procedure, due to difficulties in defining the position of the amorphous oxide/alloy interface from the measured sputter-depth profiles in Figure 3.2.

It follows that the O diffusivity in the am-Al_xZr_{1-x} alloy increases distinctly with increasing Zr concentration in the alloy: The O diffusivity in the Zr-rich am-$Al_{0.26}Zr_{0.74}$ alloy is more than three orders of magnitude higher than that in the am-$Al_{0.51}Zr_{0.49}$ alloy. It is noted that the diffusivity of oxygen in pure *crystalline* (α-)Zr is much lower than those in the *amorphous* Al_xZr_{1-x} alloys.

Table 3.1: The pre-exponential coefficient D_0, the activation energy for oxygen diffusion Q, the interfacial oxygen concentration c_i, as determined by fitting of the oxygen diffusion profiles in oxidized am-Al_xZr_{1-x} with equation (3.4) (presented in Figure 3.5), as well as the corresponding calculated diffusion coefficient D for 350 °C and 400 °C.

specimen	D_0 in m^2/s	Q kJ/mol	c_i in at.%	D (350 °C) in m^2/s	D (400 °C) in m^2/s
am-$Al_{0.51}Zr_{0.49}$	3.9×10^{-5}	174	2.3	9.9×10^{-20}	1.2×10^{-18}
am-$Al_{0.35}Zr_{0.65}$	6.4×10^{-7}	132	12.4	5.5×10^{-18}	3.6×10^{-17}
am-$Al_{0.26}Zr_{0.74}$	7.1×10^{-7}	127	15.5	1.5×10^{-17}	9.3×10^{-17}
(α-)Zr	6.61×10^{-6}	184 [22]	28.6 [20]	2.4×10^{-21} [22]	-

3.3.3 Oxidation kinetics of am-Al_xZr_{1-x} alloys

The uniform thicknesses of the amorphous oxide overgrowths (cf. Figure 3.1) for different oxidation times (1 – 10 h), alloy compositions (x = 0.68, 0.51, 0.35 and 0.26) and oxidation temperatures in the range of 350 °C to 400 °C were determined by SE (see Sec. 3.2.3): see Figure 3.6. It follows that the oxide-film growth rate increases with increasing Zr concentration in the am-Al_xZr_{1-x} alloy substrate: the oxide layer on the Zr-richest am-$Al_{0.26}Zr_{0.74}$ alloy substrate attains a thickness of 158 nm after 10 hours of oxidation at 400 °C, which can be compared with a corresponding thickness of only 15 nm for the oxidation of the Zr-poorest, am-$Al_{0.68}Zr_{0.32}$ alloy under the same oxidation conditions: see Figure 3.6.

Depending on the alloy composition, the oxidation kinetics are found to follow either a parabolic rate law or a linear rate law (see Figure 3.6a-d), as described by

$$d(t) = \sqrt{2K_\mathrm{p}t + d_0(T)^2} \tag{3.6}$$

and

$$d(t) = K_\mathrm{l}t + d_0(T), \tag{3.7}$$

respectively. In Eqs. (3.6) and (3.7), d is the oxide layer thickness, t is the oxidation time, K_p is the parabolic growth-rate constant and K_l is the linear growth-rate constant. A temperature-dependent term, $d_0(T)$, has been introduced to account for the combined effects of the native oxide (i.e. a non-zero thickness at t = 0) and an initial, very fast non-parabolic/non-linear oxidation regime (until the formation of a laterally-closed oxide layer on top of the alloy surface; see Ref. [23]). Usually, a parabolic oxide-layer growth behavior is observed when the diffusion of ions/defects through the growing oxide scale determines the rate of the oxide-growth process (diffusion-control), whereas a linear oxide-layer growth behavior is observed when a surface- or phase-boundary process, e.g. at the oxide/alloy interface, is the rate-determining step for the oxide growth (interface-control) [6, 7, 24]. It is assumed that not only the diffusion-controlled process but also the interface-controlled process is thermally activated, i.e. the rate constants K_p and K_l follow an Arrhenius behavior [6]:

$$K_\mathrm{p/l} = K_0 \times \exp\left(-\frac{Q}{\mathrm{R}\cdot T}\right), \tag{3.8}$$

where K_0 is a pre-exponential factor, Q is the activation energy for the rate-determining step in the oxidation process, R is the gas constant and T is the oxidation temperature.

For each alloy composition, linear least squares fitting of the measured and calculated oxide-layer thicknesses was performed *simultaneously* on the corresponding, entire data set of different oxidation times and oxidation temperatures, adopting Q, K_0 (both independent of T) and $d_0(T)$ as fitting parameters: see Figure 3.6. The optimized values of Q, K_0 and $d_0(T)$ have been gathered in Table 3.2.

Table 3.2: Experimentally determined (p: parabolic/l: linear) oxide-film growth parameters for crystalline Al, am-Al_xZr_{1-x} and crystalline Zr: the pre-exponential factor K_0, the activation energy Q, the oxide layer thicknesses $d_0(T_{ox})$ at t_{ox} = 0 h, the parabolic/linear oxide growth constants at 400 °C and the goodness of fit. The data for pure Al and Zr have been given for comparison.

specimen	mode	K_0	Q in kJ/mol	K_p in m²/s K_l in m/s 400 °C	d_0 in nm 350 °C	d_0 in nm 375 °C	d_0 in nm 400 °C	goodness of fit
Al	p		226 [25]*	1.10×10^{-22} [25]*,**				
am-$Al_{0.68}Zr_{0.32}$	p	1.4×10^{-15}	73	2.9×10^{-21}	2.9	2.5	6.1	0.058
am-$Al_{0.51}Zr_{0.49}$	p	2.2×10^{-11}	117	1.9×10^{-20}	11.5	12.7	16.2	0.010
am-$Al_{0.35}Zr_{0.65}$	p	1.6×10^{-05}	188	3.9×10^{-20}	9.4	8.4	0.0	0.112
am-$Al_{0.35}Zr_{0.65}$	l	0.04	135	1.4×10^{-12}	9.6	10.4	10.2	0.103
am-$Al_{0.26}Zr_{0.74}$	l	37.7	167	4.0×10^{-12}	11.9	10.9	6.0	0.108
Zr	p		133 [26]	7.1×10^{-20} [26]**				

* at 450 °C ** Converted from $g^2/(cm^4 s)$ in m^2/s by the use of the densities of Al_2O_3 [25] and ZrO_2 [27].

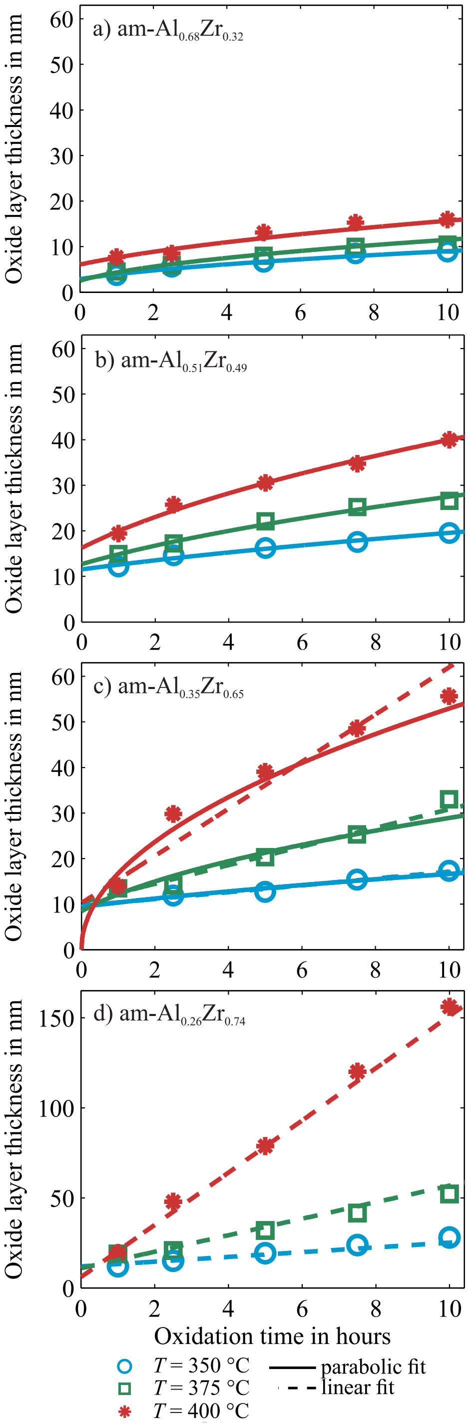

Figure 3.6: Oxide-film thickness as function of oxidation time in a temperature range of 350 °C to 400 °C. The oxide-film growth on am-Al_xZr_{1-x} alloys ($0.51 < x_{Al} < 0.68$) obeys a parabolic rate law **(a-b)**. The oxide-film growth on am-Al_xZr_{1-x} alloys ($x_{Al} = 0.26$) obeys a linear rate law **(d)**. The oxide-film growth on am-$Al_{0.35}Zr_{0.65}$ alloys takes an intermediate position **(c)**.

It follows that oxide-film growth on the Al-rich am-Al_xZr_{1-x} alloys with $x = 0.68$ and 0.51 exhibits relatively slow, *parabolic* oxidation kinetics (Figure 3.6a and b, respectively), whereas oxide-film growth on the Zr-richest am-Al_xZr_{1-x} alloy with $x = 0.26$ displays relatively fast, *linear* oxidation kinetics (see Figure 3.6d). The oxidation kinetics of the am-Al_xZr_{1-x} alloy with $x = 0.35$ takes an intermediate position: the linear and parabolic growth models can both be fitted reasonably well (although fitting with the linear growth model leads to slightly better results; cf. the goodness of fits displayed in Table 3.2): see Figure 3.6c. Hence with increasing Zr content in the alloy, a transition from parabolic oxidation kinetics to linear oxidation kinetics occurs at an alloy composition of about am-$Al_{0.35}Zr_{0.65}$. The determined activation energy Q for *parabolic* oxidation of the am-Al_xZr_{1-x} alloys increases with increasing Zr content in the range from 32 - 65 at.% Zr: i.e. $Q = 73$ kJ/mol for 32 at.% Zr, $Q = 117$ kJ/mol for 49 at.% Zr, $Q = 188$ kJ/mol for 65 at.% Zr (see Table 3.2). The activation energy Q for *linear* oxidation, as observed for the am-$Al_{0.35}Zr_{0.65}$ and $Al_{0.26}Zr_{0.74}$ alloys, also indicates an increase with increasing Zr content in the range from 65 - 74 at.% Zr: i.e. $Q = 135$ kJ/mol for 65 at.%. and $Q = 167$ kJ/mol for 74 at.% Zr. Consequently, the observed oxidation growth rates show a stronger temperature dependency with increasing Zr content in both regimes (i.e. for the parabolic oxide-growth regime observed at low Zr content and for the linear oxide-growth regime observed at high Zr content).

3.4 Proposed oxidation mechanism

3.4.1 Diffusion of O and Al in the am-Al_xZr_{1-x} alloys

The diffusivity of dissolved O in the am-Al_xZr_{1-x} alloys (solid solutions) has been found to depend strongly on the amorphous alloy composition (see Sec. 3.2): the diffusion coefficient of O increases very pronouncedly with increasing Zr content (cf. Table 3.1, Figure 3.5 and Sec. 3.3.2). Recognizing that the diffusion coefficient of O in relatively dense crystalline (α-)Zr is *much smaller* than in the considerably less dense am-Al_xZr_{1-x} alloys (cf. Table 3.1),[6] the strong dependence of the O diffusivity on Zr content for the amorphous am-Al_xZr_{1-x} alloys suggests a less dense atomic structure of the amorphous solid-solution matrix with increasing Zr content. Indeed, a recent XRD investigation of the am-Al_xZr_{1-x} alloys by our group has shown that Zr-rich am-Al_xZr_{1-x} alloys have a

---

[6] The diffusion coefficient of O in (α-)Zr is given by $D = 0.0661\cdot10^{-4}\cdot\exp(-184096/R(T+273.15))$ in m^2/s for T = 290 °C – 650 °C, as determined by tracer experiments [22].

less dense atomic packing as compared to Al-rich am-Al_xZr_{1-x} alloys [13]. Hence the increased O diffusivity in the am-Al_xZr_{1-x} alloys with increasing Zr concentration can be rationalized on the basis of atomic packing densities decreasing with increasing Zr content.

As compared to Al, Zr has a higher metal-metal bond strength ($E_{\text{Zr-Zr}}$ = 298 kJ/mol vs. $E_{\text{Al-Al}}$ = 264 kJ/mol [28]), a much higher oxygen-metal bond strength ($E_{\text{Zr-O}}$ = 776 kJ/mol vs. $E_{\text{Al-O}}$ = 511 kJ/mol [29]) and a much larger atomic size[7] (1.60 Å (Zr) vs. 1.43 Å (Al) [32]). Therefore, it may be assumed that the mobility of Al is (much) higher than that of Zr in the am-Al_xZr_{1-x} alloy and also in the O-dissolved region of the am-Al_xZr_{1-x} alloy adjacent to the oxide/alloy interface (cf. Figure 3.2). Further, recognizing the reduced packing density with increasing Zr alloying content (see above and Ref. [13]), it is likely that the mobility of Al in the am-Al_xZr_{1-x} alloy increases with increasing Zr concentration in the am-Al_xZr_{1-x} alloy. The assumption of a higher diffusivity of Al in (also oxidized) Zr-rich am-Al_xZr_{1-x} alloys is consistent with the observed differences in the oxide-film growth kinetics of the am-Al_xZr_{1-x} alloys, as discussed next in Sec. 3.4.2.

3.4.2 Oxide-film growth mechanism

In the following, the oxide-film growth kinetics of the am-Al_xZr_{1-x} alloys will be discussed on the basis of the experimental results as presented in Sec. 3.3. The exclusive, thermodynamically preferred formation of an amorphous oxide phase with a singular composition, corresponding to an Al^{ox}/Zr^{ox} atomic ratio of 0.5, has been treated in detail in Ref. [11], which can be summarized as follows: the amorphous state of the oxide overgrowth (instead of a crystalline oxide overgrowth) is attributed to relatively high energy barriers for the nucleation of the crystalline Al_2O_3 and ZrO_2 pure oxide phases in combination with a kinetic obstruction for the amorphous-to-crystalline transition of the initial amorphous oxide overgrowth. The occurrence of a practically singular composition of the amorphous oxide phase, $(Al_{0.33}Zr_{0.67})O_{1.83}$, independent of the parental alloy composition, is due to the existence of a deep minimum in the Gibbs energy of formation of the am-$(AlO_{1.5})_y(ZrO_2)_{1-y}$ phase at a composition of $y = 0.33$ (i.e. $Al^{ox}/Zr^{ox} = 0.5$).

The experimental results of the oxide-film growth rates as function of the alloy (solid solution) composition (see Sec. 3.3) demonstrate a stronger temperature

---

[7] The diffusivity of atoms in amorphous alloys was found to increase with decreasing atomic size [30, 31].

dependency with increasing Zr content both within the parabolic oxide growth regime, as observed for oxidation of am-Al_xZr_{1-x} alloy substrates with low Zr content, and within the linear oxide growth regime, as observed for oxidation of am-Al_xZr_{1-x} alloy substrates with high Zr content (cf. Figure 3.6 and Table 3.2).

The solubility of O in the am-Al_xZr_{1-x} alloy starts to increase abruptly and roughly linearly with increasing Zr alloying content for Zr contents exceeding 49 at.% (i.e. for am-Al_xZr_{1-x} with $x \leq 0.51$): see Figure 3.3a. Pure Al has a negligible O solubility [33] and the pronounced solubility of O in the am-Al_xZr_{1-x} alloy for $x \leq 0.51$ relates to the intrinsically high solubility of oxygen in pure crystalline (α-)Zr, which has an oxygen solubility limit as high as 28.6 at.% at 400 °C [20]. No distinct temperature dependency of the interfacial O concentration in the am-Al_xZr_{1-x} alloys was observed in the investigated temperature range (Figure 3.3b). This parallels the oxygen solubility limit in α-Zr which increases only very slightly with increasing temperature ($O_{\text{dissolved}}$ (at.%) $= 28.6 + \exp(-6748 \times T^{-1} + 4.748)$ for $473 \leq T \leq 1478$ K [20]).

The continuous dissolution and inward diffusion of O into the am-Al_xZr_{1-x} alloy substrate with simultaneous thickening of the oxide overgrowth (cf. Figure 3.4 and Figure 3.6) requires a constant net transport of O anions from the outer oxide surface through the developing am-(Al,Zr)-oxide layer towards the oxide/alloy interface. In the absence of short-circuit diffusion paths in the amorphous oxide overgrowth (which is of uniform thickness; cf. Figure 3.1a), such anionic transport mechanism requires coupled fluxes of inwardly migrating O anions and outwardly migrating O-vacancy-like defects. O-vacancy-like defects are easily injected into the thickening oxide overgrowth at the oxide/alloy interface by continuous dissolution of O from the amorphous oxide layer into the alloy substrate, analogous to the transport mechanism proposed for the oxidation of Zr metal [34]. The resulting oxygen-transport rate through the oxide layer is equal to the net O vacancy flux from the reacting interface to the oxide surface under influence of the respective chemical potential gradient across the thickening oxide layer [7]. At constant pressure (*here:* $pO_2 = 1 \times 10^5$ Pa), the observed larger extent of O dissolution in the alloy substrate for higher Zr alloying content is likely paralleled by a higher O defect concentration in the oxide at the reacting oxide/alloy interface and, consequently, in a larger chemical potential gradient across the oxide layer for a given oxide-layer thickness. Hence a higher oxide-film growth rate is expected for higher Zr content in the alloy substrate, which is in accordance with the experimental results (cf. Figure 3.6 and Table 3.2).

At the reacting oxide/alloy interface, the dissolution of O into the alloy substrate competes with the thermodynamically-preferred formation of the amorphous oxide phase, with an almost singular composition, $(AlO_{1.5})_{0.33}(ZrO_2)_{0.67}$, which corresponds to a constant Al^{ox}/Zr^{ox} ratio of about 0.5 [11]. Preferred formation of this am-$(AlO_{1.5})_{0.33}(ZrO_2)_{0.67}$ phase at the reacting oxide/alloy interface thus requires continuous adjustment of the interfacial alloy composition to an Al/Zr ratio of 0.5.

The am-$Al_{0.51}Zr_{0.49}$ and am-$Al_{0.68}Zr_{0.32}$ alloys have bulk Al/Zr ratios of 1.0 and 2.1, considerably larger than the preferred Al/Zr alloy ratio of 0.5 for the formation of the am-$(AlO_{1.5})_{0.33}(ZrO_2)_{0.67}$ phase. Continued oxidation of the am-$Al_{0.51}Zr_{0.49}$ and am-$Al_{0.68}Zr_{0.32}$ alloys would thus require backward diffusion of Al into the interior of the alloy substrate (recognizing that Zr is relatively immobile thus constituting the reference matrix element; see Sec. 3.4.1). If the backward diffusion of Al into the alloy is too slow as compared to the inward motion of the moving oxide/alloy boundary plane (due to continuous oxide formation), a pile-up of Al occurs. Indeed a distinct pile-up of Al in the alloy substrate at the reacting alloy/oxide interface occurs for the oxidation of the am-$Al_{0.51}Zr_{0.49}$ alloy, which has a much faster oxidation rate than the Al-richest am-$Al_{0.68}Zr_{0.32}$ alloy (and thus a faster moving oxide/alloy interface): compare Figure 3.2a,b and Figure 3.6a,b. (Selective oxidation of Zr upon thermal oxidation of crystalline, intermetallic Al-Zr alloys was also found to result in an Al enrichment in the alloy substrate [35, 36]). The pile-up of Al in the alloy substrate at the reacting oxide/alloy interface for the oxidation of especially the am-$Al_{0.51}Zr_{0.49}$ alloy can imply that the (parabolic) oxidation rate for this alloy is not only determined by the rate of oxygen transport through the oxide layer but also by the backward diffusion of Al into the interior of the alloy.

The am-$Al_{0.35}Zr_{0.65}$ alloy has a bulk Al/Zr ratio of 0.54, which is only slightly above the thermodynamically-preferred oxide composition (Al^{ox}/Zr^{ox} = 0.5). In accordance with the above discussion, oxidation of am-$Al_{0.35}Zr_{0.65}$ results in only a small Al pile-up in front of the oxide film (cf. Figure 3.2c) (see what follows).

The am-$Al_{0.26}Zr_{0.74}$ has a bulk Al/Zr ratio of 0.35, which is smaller than the preferred Al/Zr alloy ratio of 0.5 for the formation of the am-$(AlO_{1.5})_{0.33}(ZrO_2)_{0.67}$ phase. Continuous oxidation now requires diffusion of Al from the interior of the alloy towards the reacting interface to adjust the alloy composition to the preferred ratio of

Al/Zr = 0.5 for the formation of the am-$(AlO_{1.5})_{0.33}(ZrO_2)_{0.67}$ phase. If the rate of formation of the am-$(AlO_{1.5})_{0.33}(ZrO_2)_{0.67}$ phase at the reacting oxide/alloy interface would be governed by the diffusion of Al from the alloy interior to the reacting interface or by diffusion of oxygen through the oxide layer, parabolic oxidation kinetics is expected, which is clearly not observed (see Figure 3.6d). The am-$Al_{0.26}Zr_{0.74}$ is the Zr-richest alloy of this study and the dissolved O content in the alloy at the oxide/substrate interface is as large as 15.0 ± 1.2 at.% (cf. Figure 3.2d). Consequently a high Al mobility in the alloy (see Sec. 3.4.1) and a high transport rate of O through the oxide layer (see above) are expected. Then the oxide-film growth rate can be interface-controlled, i.e. governed by e.g. the redistribution of atoms at the amorphous oxide/alloy interface and consequently a linear growth rate is expected [24]. The am-$Al_{0.35}Zr_{0.65}$ alloy then takes an intermediate position.

As follows from the above discussion, the oxidation kinetics of the am-Al_xZr_{1-x} alloys are principally controlled by (*i*) the atomic mobilities of O and Al in the alloy substrate at the reacting oxide/alloy interface, (*ii*) the solubility of O in the substrate and (*iii*) the compositional constraint due to the selective formation of an amorphous oxide phase of singular composition (independent of the alloy composition); where (*i*) and (*ii*) strongly depend on the Zr content of the am-Al_xZr_{1-x} alloy substrate.

3.5 Conclusions

- The solubility of O in Al-rich am-Al_xZr_{1-x} alloys ($x_{Al} > 0.51$) is below 3 at.%. For Zr-rich am-Al_xZr_{1-x} alloys ($x_{Al} < 0.51$) the oxygen solubility abruptly increases roughly linearly with increasing Zr alloying content (up to 19.8 ± 1.1 at.% for am-$Al_{0.26}Zr_{0.74}$).
- The diffusion coefficient of oxygen in the am-Al_xZr_{1-x} alloy increases with increasing Zr alloying content in the alloy due to a decrease of the atomic packing density in the alloy (solid solution) with increasing Zr content.
- The oxide-film growth rate of am-Al_xZr_{1-x} increases pronouncedly with increasing Zr alloying content in the alloy, which is due to (*i*) the increase of the solubility of O in the alloy with increasing Zr content *and* (*ii*) the increase of the mobility of Al in the (O-dissolved region of the) am-Al_xZr_{1-x} alloy with increasing Zr content.

- Parabolic oxide-film growth kinetics occurs for Al-rich am-Al_xZr_{1-x} alloys ($x \geq 0.51$), whereas linear oxide-film growth kinetics prevails for Zr-rich am-Al_xZr_{1-x} alloys ($x < 0.35$). The am-$Al_{0.35}Zr_{0.65}$ alloy takes an intermediate position.
- The parabolic oxide-film growth kinetics of the am-$Al_{0.51}Zr_{0.49}$ (Al/Zr ratio = 1.0) and am-$Al_{0.68}Zr_{0.32}$ (Al/Zr ratio = 2.1) alloy substrates (with an Al/Zr ratio much higher than the thermodynamically-preferred Al^{ox}/Zr^{ox} ratio of 0.5) implies a diffusion-controlled oxide-growth behavior. The oxide-film growth rate can be governed by the rate of oxygen diffusion through the growing oxide layer and/or by the backward diffusion of Al from the reacting oxide/alloy interface towards the interior of the alloy (as a consequence of the exclusive formation of the thermodynamically-preferred am-$(AlO_{1.5})_{0.33}(ZrO_2)_{0.67}$ phase).
- For high Zr contents of the am-Al_xZr_{1-x} alloy, the diffusion processes in oxide film and substrate have become that fast that the oxide-film growth rate is governed by the reactive formation of the thermodynamically preferred am-$(AlO_{1.5})_{0.33}(ZrO_2)_{0.67}$ oxide phase at the oxide layer/substrate interface: linear oxide-film growth kinetics occurs.

Acknowledgements

The authors are grateful to Dipl.-Ing. F. Thiele for specimen preparation by magnetron sputtering, G. Werner for ICP-OES measurements, Dipl.-Ing. B. Siegle for AES measurements and Dr. W. Sigle and Dipl.-Ing. P. Kopold for TEM investigation (all with MPI-IS).

3.6 References

[1] Girtan M., Rusu G.I., Rusu G.G., Gurlui S., Appl. Surf. Sci. **162** (2000) 492.

[2] Park S.W., Im H.B., Thin Solid Films **207** (1992) 258.

[3] Koteneva M.V., Nikulin S.A., Rozhnov A.B., Rogachev S.O., Prot. Met. Phys. Chem. Surf. **50** (2014) 64.

[4] Brady M.P., Gleeson B., Wright I.G., JOM **52** (2000) 16.

[5] Wallwork G.R., Rep. Prog. Phys. **39** (1976) 401.

[6] Kofstad P. High-temperature oxidation of metals. New York: John Wiley & Son, 1966.

[7] Birks N., Meier G.H., Pettit F.S. Introduction to the High Temperature Oxidation of Metals. Cambridge: Cambridge University Press, 2006.

[8] Chen Q., Liu L., Zhang S.-M., Front. Mater. Sci. China **4** (2010) 34.

[9] Kakiuchi H., Inoue A., Onuki M., Takano Y., Yamaguchi T., Mater. Trans. **42** (2001) 678.

[10] Soroka I.L., Vegelius J., Korelis P.T., Fallberg A., Butorin S.M., Hjorvarsson B., J. Nucl. Mater. **401** (2010) 38.

[11] Weller K., Wang Z., Jeurgens L.P.H., Mittemeijer E.J., Acta Mater. **94** (2015) 134.

[12] Weller K., Jeurgens L.P.H., Wang Z.M., Mittemeijer E.J., Acta Mater. **87** (2015) 187.

[13] Weller K., Zotov N., Wang Z.M., Jeurgens L.P.H., Mittemeijer E.J., J. Non-Cryst. Solids **427** (2015) 104.

[14] Woollam J.A. Guide to Using WVASE32^{TM}. Lincoln: J. A. Woollam Co., Inc., 2010.

[15] Nijdam T.J., Jeurgens L.P.H., Sloof W.G., Mater. High. Temp. **20** (2003) 311.

[16] Nijdam T.J., Jeurgens L.P.H., Sloof W.G., Acta Mater. **51** (2003) 5295.

[17] Mittemeijer E.J. Fundamentals of Materials Science: The Microstructure–Property Relationship Using Metals as Model Systems. Berlin Heidelberg: Springer-Verlag, 2010.

[18] Sloof W.G., Jeurgens L.P.H., Microchim. Acta **145** (2004) 215.

[19] Wang J.Y., Mittemeijer E.J., J. Mater. Res. **19** (2004) 3389.

[20] Abriata J.P., Garcés J., Versaci R., Bull. Alloy Phase Diagr. **7** (1986) 116.

[21] Nikolussi M., Leineweber A., Mittemeijer E.J., Philos. Mag. **90** (2010) 1105.

[22] Ritchie I.G., Atrens A., J. Nucl. Mater. **67** (1977) 254.

[23] Nijdam T.J., Jeurgens L.P.H., Sloof W.G., Acta Mater. **53** (2005) 1643.

[24] Khanna A.S. Introduction to High Temperature Oxidation and Corrosion. Materials Park, OH: ASM International, 2002.

[25] Beck A.F., Heine M.A., Caule E.J., Pryor M.J., Corros. Sci. **7** (1967) 1.

[26] Hussey R.J., Smeltzer W.W., J. Electrochem. Soc. **111** (1964) 564.

[27] Pies W., Weiss A. b770, II. 1.1 Simple oxides. Key Element: O. Part 1. Berlin Heidelberg: Springer-Verlag, 1975. p.322.

[28] Luo Y.R. Comprehensive Handbook of Chemical Bond Energies. Boca Raton, FL: CRC Press, 2007.

[29] Lide D.R., editor CRC Handbook of Chemistry and Physics. Boca Raton, FL: CRC Press, 2004.

[30] Sharma S.K., Macht M.P., Naundorf V., Phys. Rev. B **49** (1994) 6655.

[31] Faupel F., Frank W., Macht M.P., Mehrer H., Naundorf V., Ratzke K., Schober H.R., Sharma S.K., Teichler H., Rev. Mod. Phys. **75** (2003) 237.

[32] Greenwood N., Earnshaw A. Chemistry of the elements. London: Butterworth-Heinemann, 1997.

[33] Wriedt H.A., Bull. Alloy Phase Diagr. **6** (1985) 548.

[34] Bakradze G., Jeurgens L.P.H., Acartürk T., Starke U., Mittemeijer E.J., Acta Mater. **59** (2011) 7498.

[35] Paljevic M., J. Alloy. Compd. **204** (1994) 119.

[36] Paljevic M., J. Alloy. Compd. **191** (1993) 27.

Chapter 4

Thermal oxidation of amorphous $Al_{0.44}Zr_{0.56}$ alloys

Katharina Weller, Lars P. H. Jeurgens, Zumin Wang and Eric J. Mittemeijer

Abstract

The oxidation of amorphous $Al_{0.44}Zr_{0.56}$ alloys upon exposure to pure O_2(g) at 500 and 560 °C (and $p_{O2} = 1\times10^5$ Pa) was investigated by a combinatorial experimental approach using X-ray diffraction, spectroscopic ellipsometry, transmission electron microscopy and Auger electron spectroscopy. During the early stages of oxidation at 500 and 560 °C, an amorphous (Zr,Al)-oxide layer of homogeneous composition and uniform thickness is formed, which is enriched in Zr with respect to the alloy substrate. At 500 °C, both the alloy substrate and the oxide layer remain amorphous during continued oxidation, whereas at 560 °C, a crystalline tetragonal ZrO_2 (t-ZrO_2) phase nucleates after prolonged oxidation, while the alloy remains amorphous. The nucleation and growth of t-ZrO_2 at 560 °C occurs exclusively close to the interface between the initially formed amorphous (Zr,Al)-oxide layer and the alloy, immediately underneath a region of Al enrichment in the substrate, as triggered by oxidation-induced compositional changes in the alloy below the reacting alloy/oxide interface and a favorable energy of the interface between t-ZrO_2 crystallites and the amorphous alloy matrix. The growing t-ZrO_2 oxide crystallites eventually laterally coalesce to form a continuous layer constituted of branches of dendrite-shaped t-ZrO_2 phase crystallites surrounded by an Al-rich amorphous Al-Zr alloy matrix. The underlying mechanism of the oxidation process is discussed.

4.1 Introduction

Bulk amorphous alloys, also known as metallic glasses, have attracted much interest in the last decade owing to their outstanding physical and chemical properties, such as high yield strength, very high elastic strain limit, good castability, good moldability and a relatively low density [1, 2]. Zr-based (e.g. Zr-Al-TM, Zr-Cu-TM, TM = transition metal) amorphous alloys represent one of the most attractive families of amorphous metallic alloys, because they possess a relatively high thermal stability and a low coefficient of thermal expansion in combination with excellent corrosion resistance [3, 4], which provides opportunities for many potential applications (see Ref. [1] and references therein). Hitherto, research on Zr-based amorphous alloys has mainly focused on the investigation of their thermal stability [5-8] and mechanical properties (e.g. Refs. [9-11]). The oxidation behavior of Zr-based amorphous alloys, in particular under near-atmospheric conditions, has received much less attention to date [12-16]. Clearly, comprehensive knowledge of the oxidation behavior of amorphous alloys is indispensable for assessing their durability and reliability under practical operating conditions. In the absence of grain boundaries in the amorphous state (cf. Ref. [17]), thermal or plasma (pre-)oxidation of (usually) homogeneous amorphous alloys is expected to result in a highly uniform oxide barrier, and this uniformity enhances the adhesion and corrosion resistance of the barrier.

The growth kinetics and developing microstructure of oxide layers formed on multicomponent Zr-based amorphous alloys by oxidation are mainly determined by the oxidation conditions (e.g. temperature, time, pressure, humidity) and the nominal (bulk) composition of the alloy [14, 18-20]. During oxidation, the composition of the alloy adjacent to the developing oxide overlayer can strongly deviate from the bulk alloy composition due to the combined effects of, for example, preferential oxidation, interfacial segregation and the nucleation of crystalline intermetallic phases. Typically cumbersome experimental assessments of the oxidation-induced microstructural changes in the alloy, as a function of the oxidation conditions, are then needed to unravel the oxidation mechanism. Such comprehensive experimental oxidation studies have been reported for *crystalline* binary, ternary and quaternary alloys [21-24], but are very scarce ([25, 26]) for *amorphous* alloys. Furthermore, it is emphasized that, due to the amorphous state of the parent alloy substrate, growth stresses in the developing oxide overlayer due to lattice mismatch strain do not occur and, consequently, the evolution of the oxide microstructure likely differs from the development of the oxide microstructure on its *crystalline* alloy counterpart [27]. It is concluded that the underlying oxidation mechanisms of *amorphous* alloys are still poorly understood.

As a first step to improve fundamental understanding of the oxidation behavior of multicomponent Zr-based amorphous alloys, oxidation studies of ***binary*** Zr-based amorphous alloy systems, like Al-Zr and Cu-Zr alloys, have to be performed. One may wonder how different or equal affinities for oxygen of the components of the alloy (*in the present study:* Al and Zr; cf. Ref. [28] for the oxidation of crystalline Al-Ti alloys) work out for the oxidation kinetics and developing oxide-layer microstructure. Revealing the preferentially oxidizing species in (crystalline) binary alloy systems of components with similarly strong oxygen affinities can in particular be difficult; for Mg-Al, see e.g. Ref. [22]. To the best of our knowledge, only one previous study has been reported on the oxidation of amorphous Al-Zr binary alloys [29], which involved the thermal oxidation of amorphous Al_xZr_{1-x} (38 at.% – 70.7 at.% Zr) thin films with a *limited thickness* of 150 nm. At elevated oxidation temperatures (up to 700 °C), the amorphous Al-Zr layer of only 150 nm thick fully transformed into oxide (a detailed investigation of the oxide composition or elemental depth distribution was not performed). Clearly such a process is not representative of the oxidation behavior of bulk amorphous Al-Zr alloys (as addressed in the present study).

The current paper presents a comprehensive investigation of the thermal oxidation of 2 μm thick (bulk-like) amorphous $Al_{0.44}Zr_{0.56}$ (am-$Al_{0.44}Zr_{0.56}$) alloy coatings at 500 °C and 560 °C and at $p_{O_2} = 1\times10^5$ Pa. At these elevated temperatures, diffusion of oxygen in the oxide, as well as oxygen dissolution in the alloy substrate, are thermally activated and relatively thick oxide layers (i.e. thicknesses > 50 nm; see Sec. 4.3.3) develop on the amorphous alloy substrate. The developing oxide film microstructure and the oxidation-induced compositional and microstructural changes in the parent am-$Al_{0.44}Zr_{0.56}$ alloy substrate were investigated by a combinatorial experimental approach using X-ray diffraction (XRD), cross-sectional (analytic) transmission electron microscopy (TEM) and Auger electron spectroscopy (AES) sputter-depth profiling. Furthermore, the oxide-film growth kinetics was investigated by spectroscopic ellipsometry (SE). The thus-obtained results on the growth kinetics and the developing oxide-layer microstructure were discussed in terms of the mechanisms and processes governing the oxidation of amorphous Al-Zr alloy systems.

4.2 Experimental procedures and data evaluation

4.2.1 Specimen preparation

Amorphous Al-Zr alloy coatings were deposited onto Si(100) wafers, covered with a 50 nm-thick thermally grown SiO_2 layer, by co-sputtering from pure Al (purity 99.9995 wt.%) and Zr (purity 98.5 wt.%) targets in an ATC 1500 F high-vacuum sputter system (base pressure ~ 5×10^{-6} Pa; AJA International Inc.). The Ar gas (purity 99.9999 at.%) was introduced into the system at a constant flow rate of 18 ml/min, leading to an equilibrium chamber pressure of 0.5 Pa. The deposition of the amorphous Al-Zr coating was carried out for 3 h, applying direct current (DC) powers of 119 W and 93 W for the Zr and Al targets, respectively, and a substrate rotation speed of 10 rpm. The sputter depositions were performed without active cooling and, consequently, the substrate temperature gradually increased from room temperature up to about 80 ºC after 3 h of deposition.

The as-deposited coatings have a uniform thickness of about 2 µm (as measured with a DekTak 8 profilometer) and a nominal composition of 44 at.% Al and 56 at.% Zr (as measured by electron probe microanalysis using a Cameca SX100 microprobe system). The amorphous structure of the as-deposited $Al_{0.44}Zr_{0.56}$ alloy was confirmed by XRD and TEM (see Figure 4.9 and discussion thereof in the supporting information). The specimens are further designated as am-$Al_{0.44}Zr_{0.56}$ alloy.

4.2.2 Oxidation of the am-$Al_{0.44}Zr_{0.56}$ alloy

The as-deposited am-$Al_{0.44}Zr_{0.56}$-coated wafers were cut into small pieces (14×14 mm^2), each of which was enclosed in a separate quartz ampoule. The ampoules were evacuated and then filled with pure oxygen up to an oxygen partial pressure of $p_{O_2} = 3.50\times10^4$ Pa at room temperature (RT), which corresponds to $p_{O_2} = 1\times10^5$ Pa at 560 °C. Subsequently, the sealed ampoules were introduced into a pre-heated furnace at T_{ox} = 560 °C for different oxidation times (t_{ox} = 15, 30, 45, 60, 120, 180, 240, 300 minutes). After the chosen oxidation times, the ampoules were taken out of the furnace and immediately quenched in water (T ~ 18 °C). Analogously, an additional series of oxidation experiments was performed at T_{ox} = 500 °C for oxidation times of t_{ox} = 60, 120, 180, 240 and 300 minutes ($p_{O_2} = 3.8\times10^4$ Pa at RT / $p_{O_2} = 1\times10^5$ Pa at 500 °C).

4.2.3 X-ray diffraction

The phase constitution and crystallinity of the as-deposited and oxidized am-$Al_{0.44}Zr_{0.56}$ alloys were determined by XRD. To this end, θ-2θ scans were recorded over a 2θ range from 10° to 65° using a Bruker D8 Discover diffractometer, operating in parallel-beam geometry, applying Cu-$K\alpha$ radiation (λ = 1.54056 Å) combined with an energy-dispersive detector.

4.2.4 Spectroscopic ellipsometry

The oxidation kinetics of the am-$Al_{0.44}Zr_{0.56}$ alloy was investigated by SE using a J.A. Woollam M-2000^{TM} spectroscopic ellipsometer equipped with a Xenon light source (wavelength λ range: 300–850 nm). The ellipsometric parameters Ψ and Δ as functions of λ were recorded at variable incident angles φ = 60°, 65°, 75° and 80° (with respect to the surface normal) from the as-prepared and oxidized alloy. To determine the oxidation kinetics from the measured spectra of $\Psi(\lambda, \varphi)$ and $\Delta(\lambda, \varphi)$, a method similar to that described in Refs. [30, 31] has been used, in which the evolving alloy substrate/oxide layer system is described by an optical model incorporating an am-$Al_{0.44}Zr_{0.56}$ substrate covered with a double-layered structure including an external (i.e. surface-adjacent) oxide layer of uniform thickness, L_{ox}, and an intermediate (interface-adjacent) layer of uniform layer thickness, L_{EMA}. More details of the optical model and the fitting procedure/parameters are given in the supporting information.

4.2.5 Transmission electron microscopy

The microstructure of the oxidized am-$Al_{0.44}Zr_{0.56}$ alloy was studied by TEM using a Philips CM 200 microscope operated at 200 kV and by energy-filtered TEM (EFTEM) using a Zeiss 912 Omega microscope operated at 120 kV. Cross-sectional TEM specimens were prepared using the so-called “tripod polishing method” (see the supporting information for the detailed procedure). Elemental distributions in the oxidized am-$Al_{0.44}Zr_{0.56}$ alloys were obtained by EFTEM imaging at the Al *L* edge (73 eV), the Zr *M* edge (180 eV) and the O *K* edge (532 eV) in the cross-sectional lamellae of the oxidized am-$Al_{0.44}Zr_{0.56}$ alloys. A standard three-window method [32] (two pre-edge signal windows before the ionization-edge and a post-edge signal window) was applied for such energy-filtered TEM imaging.

4.2.6 Auger electron spectroscopy sputter-depth profiling

The elemental depth-distribution in the developing oxide layer and the adjacent alloy substrate were determined by AES sputter-depth profiling. To this end, alternating cycles of AES analysis and ion sputtering were performed with a JEOL JAMP 7830F scanning Auger microscope. During each measurement step, spectra of the Al LMM, Zr MNN and O KLL Auger lines were recorded using a primary electron beam of 10 keV and 15 nA scanning an area of $10\times10\ \mu m^2$. The sputtering steps were performed for 30 s using a focused 3 kV Ar^+ beam with a current of about 0.7 μA, scanning an area of

500×500 μm^2. To prevent differential charging of the insulating oxide layer during the analysis steps, each specimen was precoated with a 50 nm thick Al capping layer (by magnetron sputtering) prior to the AES analysis. The peak-to-peak intensities of the various oxidic and metallic spectral contributions were resolved from the differential AES spectra using the linear least-squares fitting procedure as implemented in the Phi-MultiPak software (version 7.5). For each recorded sputter-depth profile, a linear conversion of the cumulative sputter time to the (approximate) sputter depth was performed by applying the sputter rate as determined from the known Al capping layer thickness of 50 nm (see above). Concentration-depth profiles for the resolved metallic and oxidic Al and Zr signals and the O signal were obtained by multiplying the respective peak-to-peak intensities with experimentally determined sensitivity factors (see the supporting information) and normalizing to 100 at.%.

4.3 Results

4.3.1 Oxidation of the am-$Al_{0.44}Zr_{0.56}$ alloy at 500 °C

The evolution of the XRD patterns of the am-$Al_{0.44}Zr_{0.56}$ alloy for different oxidation times up to 300 minutes at 500 °C (p_{O_2} = 1×10^5 Pa) is presented in Figure 4.1a. All recorded diffraction patterns only display a broad intensity hump at $2\theta \sim 36°$, which originates from the am-$Al_{0.44}Zr_{0.56}$ alloy. It is thus concluded that neither a crystalline oxide phase nor a crystalline metallic phase (due to nucleation of a crystalline intermetallic or solid-solution phase) develops upon prolonged oxidation at 500 °C. Corresponding cross-sectional TEM analysis indeed reveals the formation of an *amorphous* oxide layer with a uniform thickness of about 300 nm after oxidation at 500 °C for 300 minutes (see micrograph and selected-area electron diffraction pattern (SADP) in Figure 4.1b). With increasing oxidation time, the recorded XRD intensity hump at $2\theta \sim 36°$ corresponding to the am-$Al_{0.44}Zr_{0.56}$ alloy decreases (see Figure 4.1a), which is attributed mainly to the reduction in the thickness of the am-$Al_{0.44}Zr_{0.56}$ alloy substrate due to the amorphous oxide growth and partially to X-ray absorption by the overgrown amorphous oxide. The XRD patterns further evidence a development of small intensity at around $2\theta \sim 30°$ with increasing oxidation time, which should correspond to the X-ray scattering from the growing amorphous oxide layer (cf. Ref. [33]). The thickness of the amorphous oxide layer as function of the oxidation time up to 300 minutes at 500 °C, as determined by cross-sectional TEM and SE, is shown in Figure 4.2 (for detailed analysis of the oxide-layer growth kinetics, see Sec. 4.3.3).

As evidenced by AES sputter-depth profiling analysis (see Figure 4.1c), the amorphous oxide layer grown at 500 °C contains both oxidized Zr and Al and possesses a homogeneous composition of 11.0±0.7 at.% Al, 25.0±0.4 at.% Zr and 63.7±0.6 at.% O. This corresponds to a constant Al/Zr atomic ratio of 0.44±0.03 in the amorphous oxide, which is lower than the Al/Zr ratio of 0.68±0.01 in the bulk alloy. This implies that the amorphous (Zr,Al)-oxide layer is enriched in Zr with respect to the alloy: i.e. Zr is preferentially oxidized from the am-$Al_{0.44}Zr_{0.56}$ alloy. The AES analysis further reveals a pronounced dissolution and inward diffusion of O into the alloy substrate during oxidation (the O content of the alloy substrate is about 8.6±0.4 at.% at 500 °C; see Figure 4.1c). Further, an enrichment (i.e. a pile-up) of Al in the alloy adjacent to the reacting interface is observed after the oxidation at 500 °C for 180 minutes (see Figure 4.1c), which is discussed in Secs. 4.3.2.3 and 4.4.1.

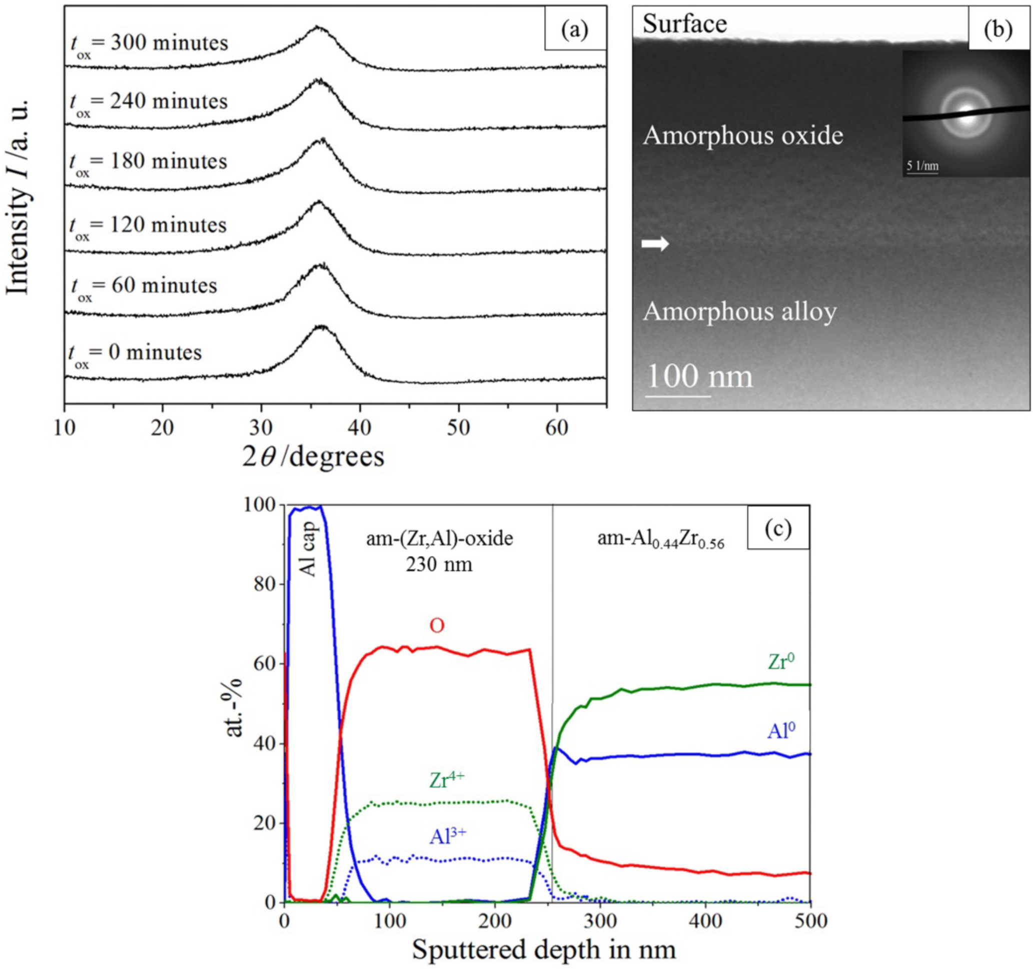

Figure 4.1: (a) XRD patterns recorded from the am-$Al_{0.44}Zr_{0.56}$ alloy after oxidization for different times (t_{ox}) at 500 °C (p_{O2} = 1×10^5 Pa). **(b)** Cross-sectional bright-field TEM micrograph of the am-$Al_{0.44}Zr_{0.56}$ thin film after oxidation at 500 °C for 300 minutes. The arrow in (b) indicates the (approximate) location of the oxide/alloy interface. A selected area electron diffraction pattern recorded from the amorphous oxide region is shown in the inset of (b). **(c)** Concentration-depth profiles of the am-$Al_{0.44}Zr_{0.56}$ alloy after oxidation at 500 °C for 180 minutes, as measured by AES sputter depth profiling.

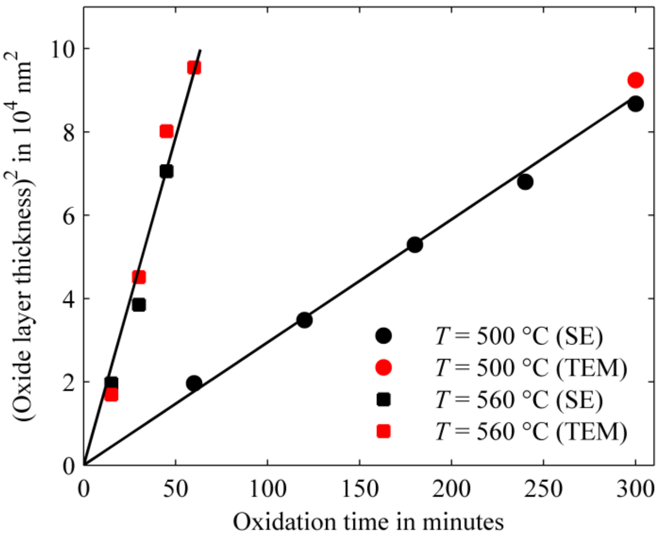

Figure 4.2: (Oxide layer thickness)^2 as a function of the oxidation time for the thermal oxidation of the am-$Al_{0.44}Zr_{0.56}$ alloy at 500 °C and 560 °C (at $p_{O2} = 1\times10^5$ Pa), as determined independently by spectroscopic ellipsometry (SE) and TEM. For details, see Secs. 4.3.3 and 4.4.1. Note that the error bars are smaller than the size of the symbols: the standard deviation of the thickness values determined by TEM is ± 5 nm; the figure of merit (FOM) for the thickness values determined by SE is ± 0.26 nm.

4.3.2 Oxidation of the am-$Al_{0.44}Zr_{0.56}$ alloy at 560 °C

4.3.2.1 Oxide microstructure

XRD analysis of the am-$Al_{0.44}Zr_{0.56}$ alloy after oxidation at 560 °C (also) shows no formation of a crystalline oxide during initial oxidation up to 60 minutes (i.e. again only a distinct broad intensity hump from the am-$Al_{0.44}Zr_{0.56}$, and a small intensity increase at $2\theta \sim 30°$ from the amorphous oxide, is observed in the recorded diffraction patterns; see Figure 4.3 and cf. Sec. 4.3.1). This is in accordance with the cross-sectional TEM analysis presented in Figure 4.4b-e, showing the formation of an amorphous oxide layer with a very uniform thickness for oxidation times up to 60 minutes. The thickness of the amorphous oxide layer as function of oxidation time up to 60 minutes, as determined by cross-sectional TEM and SE, is shown (also) in Figure 4.2 (for discussion, see Sec. 4.3.3). The amorphous oxide layers grown at 500 °C and at 560 °C (up to 60 minutes) will be designated hereinafter as *am-(Zr,Al)-oxide layer*.

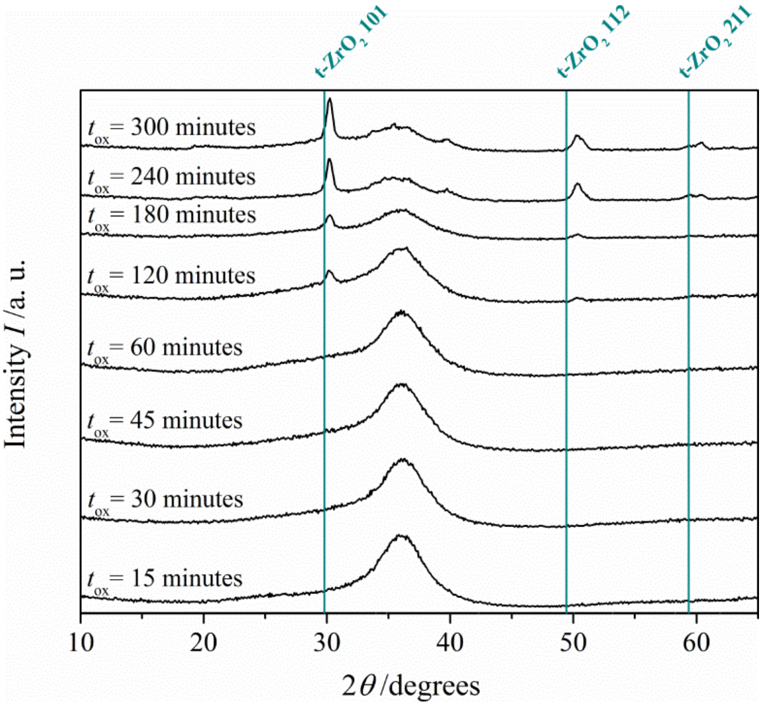

Figure 4.3: XRD patterns recorded from the am-$Al_{0.44}Zr_{0.56}$ alloy after oxidization for different times (t_{ox} = 15 min – 300 min) at 560 °C ($p_{O2} = 1\times10^5$ Pa), indicating the formation of a crystalline tetragonal ZrO_2 phase (*t*-ZrO_2) for $t_{ox} > 60$ minutes.

After 120 minutes of oxidation, sharp diffraction peaks are observed in the recorded XRD patterns (see Figure 4.3), which can be unambiguously attributed to the formation of a crystalline tetragonal ZrO_2 (β-ZrO_2) phase (further designated as *t*-ZrO_2; ICDD card 00-042-1164 [34]). The corresponding cross-sectional TEM analysis shows that the first oxide crystallites have already nucleated in the alloy substrate close to the interface between the am-$Al_{0.44}Zr_{0.56}$ alloy substrate and the external (i.e. surface-adjacent) amorphous oxide layer after 45 minutes of oxidation: see Figure 4.4d. The density of the initial oxide nuclei (as distributed along the interface), as well as (to a lesser extent) the average crystallite size, both increase with increasing oxidation time. Obviously, at the very early stage of crystallization, the tiny *t*-ZrO_2 crystallites are too small to be detected by XRD. Analysis of recorded SADPs of the oxide crystallites in TEM confirm that the crystalline oxide phase corresponds to *t*-ZrO_2: see Figure 4.4g (SADP) and h (dark-field image). The diffraction pattern in Figure 4.4g contains two sets of diffraction spots rotated about 5° relative to each other, which suggests that the corresponding *t*-ZrO_2 crystalline particle (see Figure 4.4h) contains a small-angle grain boundary.

After initiation of nucleation of *t*-ZrO_2, the growth of the external am-(Zr,Al)-oxide layer retards with respect to the parabolic growth behavior (see Sec. 4.3.3) of earlier times: continued oxidation predominantly involves continued nucleation and growth of *t*-ZrO_2 underneath the external am-(Zr,Al) oxide layer (cf. cross-sectional TEM images in Figure 4.4e and f). The *t*-ZrO_2 crystallites preferentially grow inwardly (i.e. into the interior of the am-$Al_{0.44}Zr_{0.56}$ alloy substrate) and thereby develop an irregular (dendritic-like) morphology without distinct crystal facets (see Figure 4.4e). After 120 minutes of oxidation at 560 °C (see Figure 4.4f), the *t*-ZrO_2 crystallites have coalesced into a seemingly laterally continuous crystalline layer of irregular thickness underneath the initially formed external am-(Zr,Al)-oxide layer. Upon continued oxidation (180 minutes - 300 minutes), this layer grows further into the am-$Al_{0.44}Zr_{0.56}$ alloy substrate, as shown by the cross-sectional bright-field and dark-field TEM images for an oxidation time of 180 min in Figure 4.5a-c. A high-magnification dark-field TEM image (taken by selecting a diffraction spot from *t*-ZrO_2) of the crystalline oxide layer region for the oxidation time of 300 min (Figure 4.5d) shows that this crystalline oxide layer is not completely compact and actually consists of interconnected branches of *t*-ZrO_2 crystallites. Therefore the crystalline oxide layer will be further designated as a (quasi-)continuous *t*-ZrO_2 layer.

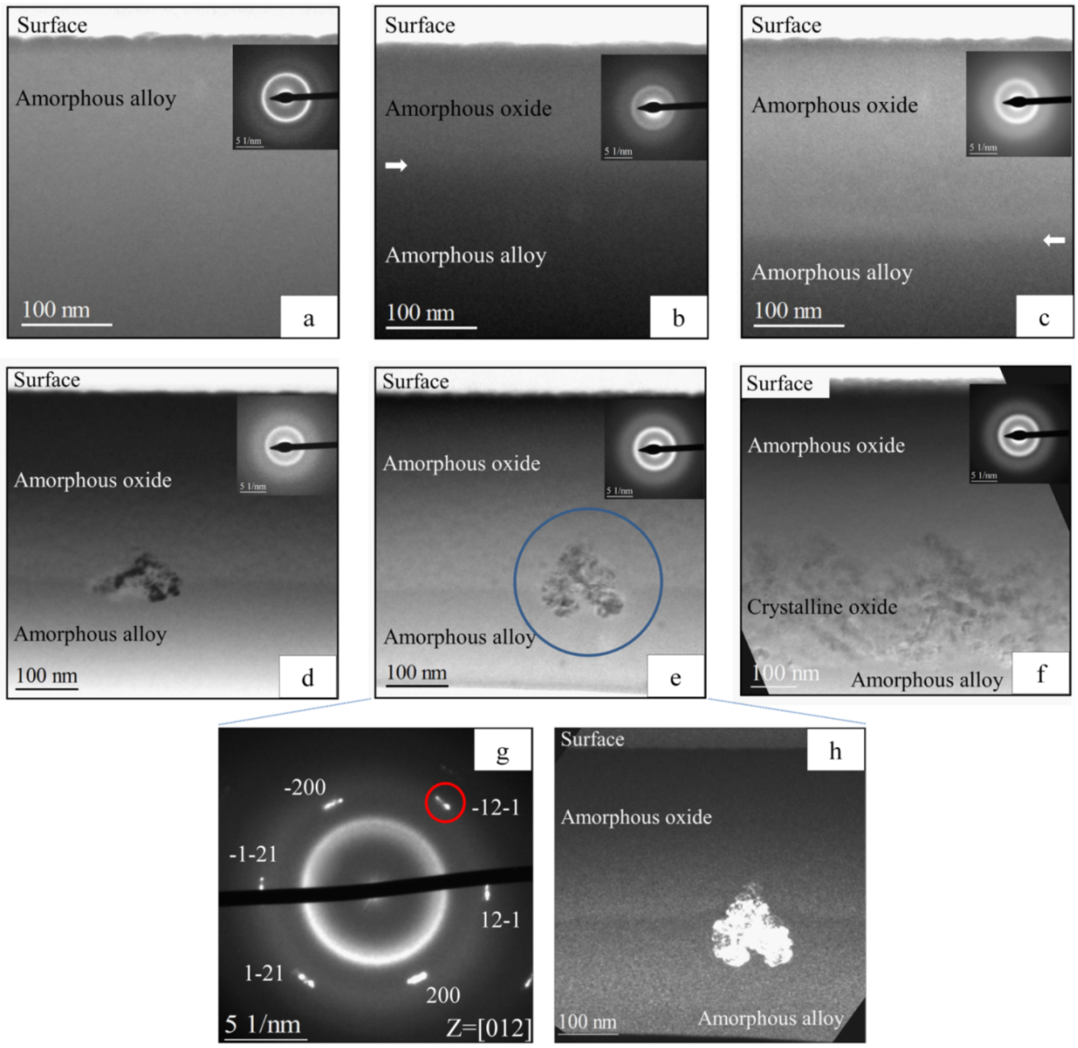

Figure 4.4: Cross-sectional bright-field TEM images of as-deposited am-$Al_{0.44}Zr_{0.56}$ thin film **(a)** before oxidation, and after oxidation at 560 °C (p_{O2} = 1×10^5 Pa) for **(b)** 15 minutes, **(c)** 30 minutes, **(d)** 45 minutes, **(e)** 60 minutes and **(f)** 120 minutes. The insets of (b) to (f) show corresponding SAD patterns from selected regions in the amorphous oxide layer adjacent to the surface. The arrows in **(b)** and **(c)** indicate the (approximate) location of the alloy/am-oxide interface. The SAD pattern taken at the *t*-ZrO_2 crystallite marked in **(e)** is shown in **(g)**. The corresponding dark field-TEM image, as obtained by selecting the diffraction spots marked in (g), is shown in **(h)**.

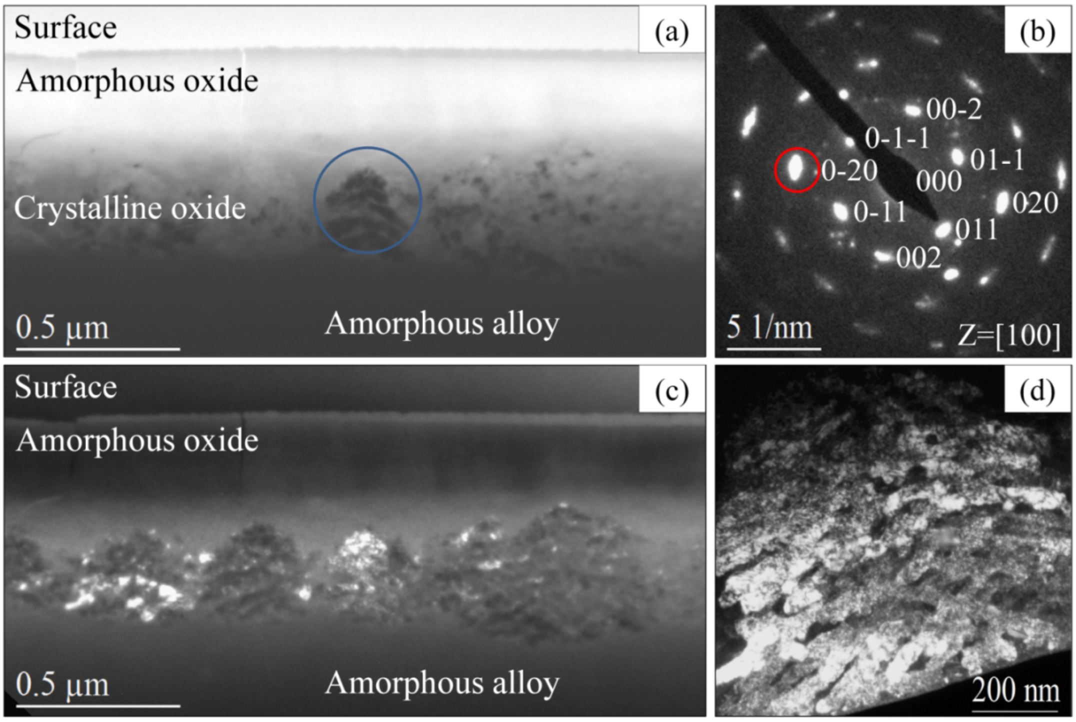

Figure 4.5: Cross-sectional TEM analyses of the am-$Al_{0.44}Zr_{0.56}$ specimen oxidized at 560 °C (p_{O2} = 1×10^5 Pa) for 180 minutes. **(a)** bright-field TEM image, **(b)** SAD pattern taken at the crystalline *t*-ZrO_2 region marked in (a), **(c)** dark-field TEM image as obtained by selecting the 0-20 *t*-ZrO_2 diffraction spot marked in (b). The cracks in the surface oxide layer (dark lines in (c) originate from TEM sample preparation. **(d)** dark-field TEM image (taken by selecting a diffraction spot from *t*-ZrO_2) of the crystalline oxide region of the am-$Al_{0.44}Zr_{0.56}$ specimen oxidized at 560 °C (p_{O2} = 1×10^5 Pa) for 300 minutes, showing that the crystalline oxide region is composed of interconnected branches of *t*-ZrO_2 crystallites.

4.3.2.2 Elemental distribution in the layer containing crystalline oxide (*t*-ZrO_2)

The local elemental distributions of Al, Zr and O in the (quasi-)continuous *t*-ZrO_2 layer, as formed after prolonged oxidation (i.e. t_{ox} = 180 min) at 560 °C, were analyzed by EFTEM: see Figure 4.6. A bright-field TEM image of the investigated crystalline oxide region is shown in Figure 4.6a. Individual EFTEM elemental maps of the Al L edge (green), the Zr M edge (blue) and the O K edge (red) are presented in Figure 4.6b-d, respectively. An overlay of the individual elemental maps of Al, Zr and O is shown in Figure 4.6e. The purple-colored areas in the branch-like structure of Figure 4.6e result from the overlapping of the signal contributions of Zr and O in Figure 4.6c and d, respectively. It follows that the (Zr,O)-rich purple-colored areas in the branch-like structure in Figure 4.6e correspond to pure *t*-ZrO_2 crystallites, i.e. no (or a negligible) amount of Al is detected in the *t*-ZrO_2 phase.

The EFTEM analysis further reveals a pronounced Al enrichment (as compared to the alloy substrate) in the matrix surrounding the *t*-ZrO_2 crystallites (Figure 4.6b). The corresponding AES analysis (see Sec. 4.3.2.3) also evidences a lower concentration of metallic Zr between the branches of *t*-ZrO_2, which could not be detected by EFTEM analysis (due to its lower sensitivity); this metallic Zr is likely left over from the alloy substrate upon developing of the *t*-ZrO_2 branches. The inter-branch regions entangling the *t*-ZrO_2 crystallites thus correspond to an Al-enriched Al-Zr alloy (possibly with some dissolved remaining oxygen), which is amorphous as proven by XRD and TEM.

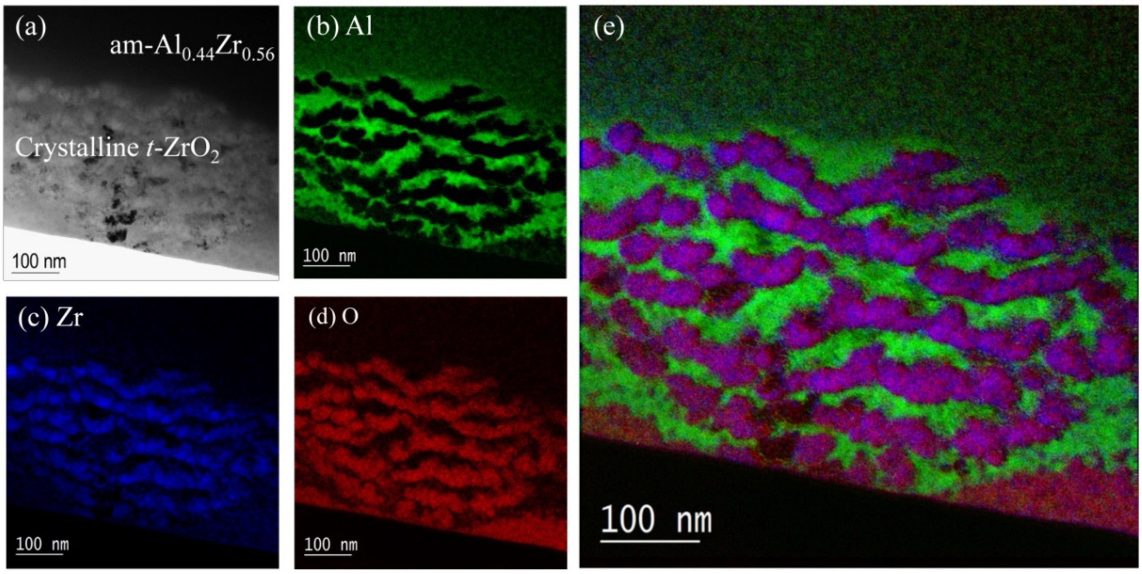

Figure 4.6: **(a)** Bright-field TEM image of the am-$Al_{0.44}Zr_{0.56}$ specimen oxidized at 560 °C for 180 minutes showing the continuous crystalline oxide, *t*-ZrO_2 layer. Elemental mapping of **(b)** the Al L edge at 73 eV (green), **(c)** the Zr M edge at 180 eV (blue) and **(d)** the O K edge at 532 eV (red). **(e)** Overlay of the individual elemental maps of Al, Zr and O (note: the purple color results from the overlapping signal intensities of Zr and O). The uniform dark grey area in (a) corresponds to the am-$Al_{0.44}Zr_{0.56}$ alloy substrate (not electron transparent).

4.3.2.3 Depth-resolved chemical constitution

The measured AES sputter-depth profiles after thermal oxidation of the am-$Al_{0.44}Zr_{0.56}$ alloy for 15, 30, 45, 180 and 240 minutes at 560 ºC are shown in Figure 4.7a-f, respectively. The Al capping layer, as deposited on top of the alloy after oxidation, is clearly resolved in all sputter-depth profiles (see Sec. 4.2.6). As evidenced by XRD and TEM (see Sec. 4.3.2.1), for $t \leq 60$ minutes, an amorphous oxide layer of uniform thickness has formed and pronounced nucleation of *t*-ZrO_2 has not yet occurred. The corresponding AES sputter-depth profiles for $t_{ox} = 15$ min (Figure 4.7a), $t_{ox} = 30$ min (Figure 4.7b) and $t_{ox} = 45$ min (Figure 4.7c) show a homogeneous composition of the amorphous (Zr,Al)-oxide layer. The amorphous (Zr,Al)-oxide layer is enriched in Zr (relative to Al, as compared to the substrate) and overall contains 10.7±1.0 at.% Al and 25.5±0.6 at.% Zr at 560 ºC. The composition of the amorphous oxide layer remains approximately constant upon continued oxidation (which involves predominantly subsequent growth of *t*-ZrO_2) up to 240 minutes at 560 ºC (cf. Figure 4.7). Moreover, the compositions of the amorphous oxide layers grown at 500 ºC and 560 ºC are practically the same (within experimental accuracy).

The AES analysis reveals the occurrence of a pronounced dissolution and inward diffusion of O into the underlying alloy substrate during oxidation, which indicates a high diffusivity of O anions through the developing am-(Zr,Al) oxide layer at 560 ºC. For the amorphous oxide-growth regime up to $t_{ox} = 45$ min, an enrichment of Al in the alloy substrate adjacent to the reacting interface is observed (Figure 4.7a-c), which runs parallel with a slight, gradual increase of the dissolved O concentration in front of the Al-enrichment zone (Figure 4.7d). The enrichment of Al in the substrate at the reacting alloy/oxide interface has disappeared after oxidation for 180 and 240 minutes at 560 ºC (see Figure 4.7e and f), i.e. after the nucleation and lateral growth of *t*-ZrO_2. After these prolonged oxidation times at 560 ºC, a double-layered oxide structure has developed, which consists of a surface layer of amorphous (Zr,Al)-oxide and a bottom (quasi-)continuous layer (see Sec. 4.3.2.2) of polycrystalline *t*-ZrO_2: as shown in Sections 4.3.2.1 and 4.3.2.2. The AES depth profiles after 180 and 240 minutes show that the *t*-ZrO_2 growth front gradually advances inwardly (i.e. the region containing *t*-ZrO_2 thickens), whereas growth of the am-(Zr,Al)-oxide layer retards (with respect to the parabolic growth behavior observed for $t_{ox} \leq 60$ minutes; see Sec. 4.3.3). A constant (stoichiometric) O/oxidic-Zr atomic ratio is established across the polycrystalline oxide region (i.e. intensity plateaus of the O and oxidic Zr signals are observed; see Figure 4.7e and Figure 4.7f). The AES analysis also exposes the presence of enriched (as compared to the alloy substrate) metallic Al (and some metallic Zr) within the polycrystalline oxide region. The o*xidic* Al intensity within the crystalline oxide region is practically negligible. These AES results are fully consistent with the corresponding XRD, TEM and EFTEM analyses (discussed in sections 4.4.2, 4.3.2.1 and 4.3.2.2), indicating that the inter-branch regions surrounding the t-ZrO_2 crystallites correspond to a relatively Al-rich amorphous Al-Zr solid solution (see Figure 4.7f).

4.3.3 Oxidation kinetics at 500 °C and 560 °C

The square of the oxide-layer thickness, as determined by SE ($L_{\mathrm{total}} = L_{\mathrm{ox}}+L_{\mathrm{EMA}}$, see Section 4.2.4) and by cross-sectional TEM analysis (see Section 4.2.5), have been plotted as a function of the oxidation time in Figure 4.2 for the oxidation experiments at 500 °C and 560 °C (at $pO_2 = 1\times10^5$ Pa). The total oxide-layer thickness values obtained by SE, $L_{\mathrm{total}} = L_{\mathrm{ox}}+L_{\mathrm{EMA}}$, as introduced in the optical model (see Sec. 4.2.4), are in very good agreement with oxide-layer thickness values independently determined by TEM (see Secs. 4.3.1 and 4.3.2.1). The EMA thickness values, L_{EMA}, describing the changes of the optical constants of the evolving substrate/film system adjacent to the oxide/alloy interface (see Sec. 4.2.4), are (very) much smaller than the corresponding thickness values, L_{ox}, of the bulk amorphous oxide top layer: At 500 °C, L_{EMA} equals 21.8±3.2 nm, approximately independent of oxidation time and temperature. At 560 °C, L_{EMA} gradually decreases with increasing oxidation time from 23.3±0.3 nm after t_{ox} = 30 minutes to 17.8±0.1 nm after t_{ox} = 45 minutes.

As soon as a t-ZrO_2 has significantly nucleated at the interface between the am-(Zr,Al) oxide layer and the alloy substrate (i.e. for $t \geq 60$ minutes at 560 °C, as in particular shown by TEM in Sec. 4.3.2.1), the optical model fails to describe the measured spectra of $\Psi(\lambda, \varphi)$ and $\Delta(\lambda, \varphi)$. Then only the thickness value determined by TEM can be used for the oxidation time of 60 minutes at 560 °C.

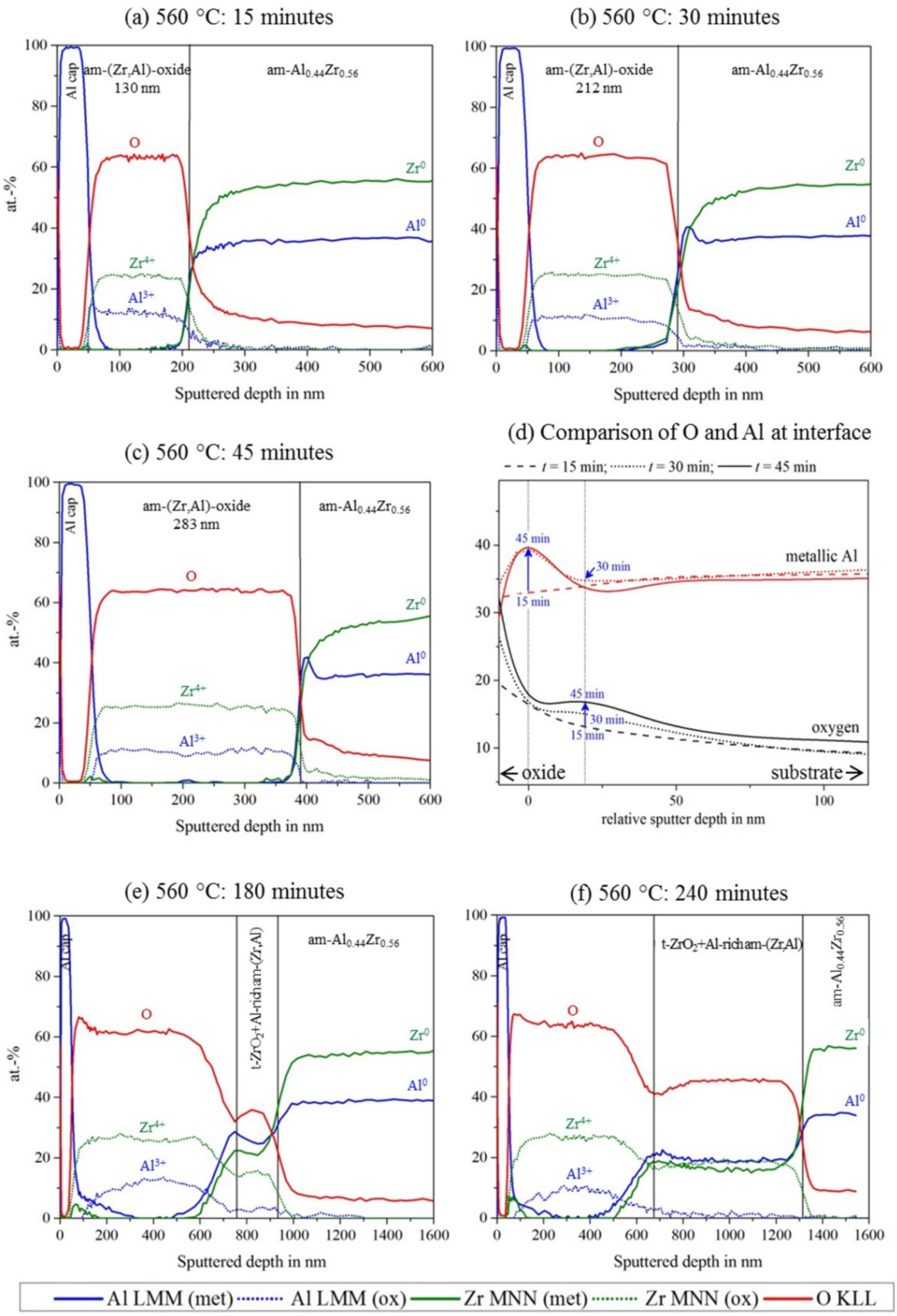

Figure 4.7: AES elemental concentration-depth profiles of the am-$Al_{0.44}Zr_{0.56}$ alloy after oxidation at 560 °C for: **(a)** 15 minutes, **(b)** 30 minutes, **(c)** 45 minutes, **(e)** 180 minutes and **(f)** 240 minutes. **(d)** shows a comparison of Al and O concentrations at the amorphous oxide/amorphous alloy interface for am-$Al_{0.44}Zr_{0.56}$ samples oxidized at 560 °C for 15, 30 and 45 minutes. (Relative sputter depth: 0 = maximum of Al enrichment for 30 and 45 minutes oxidation; for the specimen without Al enrichment (15 minutes oxidation) the relative sputter

depth was set by letting coincident the oxygen levels at large depths (larger than 100 nm below the amorphous oxide layer) for the experiments for 15 and 30 minutes of oxidation.

The observed linear relationship between (layer thickness)^2 and oxidation time (see Figure 4.2) implies that the oxidation kinetics of the am-$Al_{0.44}Zr_{0.56}$ alloy obeys a parabolic growth law. This suggests that, at 500 °C and 560 °C ($t \leq 60$ min), the rate of oxidation of the am-$Al_{0.44}Zr_{0.56}$ alloy is rate-limited by diffusion of reactants through the am-(Zr,Al) oxide layer, i.e. presumably by the diffusion of oxygen anions (see discussion in Sec. 4.4.1). Note that the intercepts of the linear fit of L_{total}^2 versus t in Figure 4.2 cross the origin (within experimental accuracy), implying a parabolic oxide growth behavior from the beginning of oxidation. The experimentally determined parabolic growth constants equal $k_p = 4.92\times10^{-14}$ cm^2/s and $k_p = 2.62\times10^{-13}$ cm^2/s at 500 °C and 560 °C, respectively (see Figure 4.2 and discussion in Sec. 4.4.1).[1]

4.4 Discussion of oxide-growth behavior and mechanisms

On the basis of the results presented in Section 4.3, the oxidation behavior of the am-$Al_{0.44}Zr_{0.56}$ alloy at 500 °C and 560 °C ($p_{O_2} = 1\times10^5$ Pa) can be subdivided into three characteristic (partially overlapping) oxidation regimes, which are discussed below and are schematically illustrated in Figure 4.8.

4.4.1 Stage I: amorphous oxide-layer growth

The onset of oxidation of the am-$Al_{0.44}Zr_{0.56}$ alloy at 500 °C and 560 °C ($p_{O_2} = 1\times10^5$ Pa) is characterized by the formation and overgrowth of an amorphous (Zr,Al)-oxide layer of uniform thickness and homogeneous composition: see Stage I in Figure 4.8. Strikingly, the amorphous oxide layers formed at 500 °C and 560 °C have the same nominal composition, practically independent of the oxidation time. The average Al and Zr contents of the amorphous oxide layers, as determined from the measured AES depth profiles after various oxidation times at 500 °C and 560 °C, are 10.8±0.8 at.% Al and 25.2±0.5 at.% Zr. The corresponding Al/Zr-atomic ratio of 0.43±0.03 for the amorphous oxide layer is significantly lower than the Al/Zr-ratio of 0.68±0.01 of the bulk am-$Al_{0.44}Zr_{0.56}$ alloy (see Figure 4.1c and Figure 4.7). Hence Zr is preferentially oxidized from the am-$Al_{0.44}Zr_{0.56}$ alloy substrate.

---

[1] The parabolic growth constants were obtained according to $k_p = L_{total}^2/t$.

The Gibbs energies of formation, $\Delta_f G^0$, (in kJ per mole O) at 800 K (i.e. in between 500 °C and 560 °C) for the common crystalline ZrO_2 and Al_2O_3 single-oxide phases, as well as for amorphous ZrO_2 and Al_2O_3 (as estimated from the respective configurationally frozen liquid oxide phases below the glass transition [27]) have been gathered in Table 4.1. It follows that the listed bulk Gibbs energies of formation (per mole O) are practically identical for am-Al_2O_3 and am-ZrO_2. Hence bulk thermodynamic considerations cannot explain the observed preferential oxidation of Zr from the am-$Al_{0.44}Zr_{0.56}$ alloy. The constant homogeneous composition of the amorphous (Zr,Al)-oxide phases independent of oxidation time and temperature instead suggests the existence of a distinct minimum in the Gibbs energy of mixing of the homogeneous $(Al_2O_3)_x(ZrO_2)_y$ solid solution at a composition of 10.8±0.8 at.% Al and 25.2±0.5 at.% Zr, likely in combination with a favorably low interface energy between the amorphous oxide and the amorphous solid solution (due to the absence of lattice-mismatch strains; see [35, 36] and also Section 4.4.2). Ongoing structural investigations in combination with a detailed thermodynamic assessment of the Al_2O_3-ZrO_2 pseudo-phase diagram by the present authors indeed reveal metastability for an amorphous $(AlO_{1.5})_{0.5}(ZrO_2)_1$ ternary oxide phase [37]. It is thus concluded that, in the studied oxidation regime, the phase constitution of the oxide layer is not determined by the reaction kinetics (e.g. by a flux balance of the rates of incorporation of Zr and Al into the growing oxide and the rates of diffusion of Al and Zr from the interior of the bulk alloy to the reacting alloy/oxide interface; e.g. see Ref. [38]).

Table 4.1: The Gibbs energies of formation, $\Delta_f G^0$ (in kJ per mole O), at 800 K (and at 1 atm) for common crystalline ZrO_2 and Al_2O_3 pure oxide phases, as well as for amorphous ZrO_2 and amorphous Al_2O_3 (estimated from the corresponding configurationally frozen liquid phases below the glass transition [27]). All necessary thermodynamic data were taken from [39].

Chemical formula	$\Delta_f G^0$ in kJ/mol O atom at 800 K
Monoclinic α-ZrO_2	-473
Tetragonal β-ZrO_2	-470
am-ZrO_2	-445
Rhombohedral α-Al_2O_3	-475
Cubic γ-Al_2O_3	-470
am-Al_2O_3	-445

The am-$Al_{0.44}Zr_{0.56}$ alloy dissolves a considerable amount of oxygen during oxidation at $T \geq 500$ °C (see Section 4.3.2.3). This indicates that at $T \geq 500$ °C, oxygen anions can easily migrate through the developing am-(Zr,Al)-oxide layer towards the reacting oxidation front, presumably by a “vacancy”-like diffusion mechanism (as discussed for the oxygen diffusion in amorphous Al_2O_3 [40]), to dissolve and diffuse into the am-$Al_{0.44}Zr_{0.56}$ alloy substrate. The transport of O anions through the thickening am-(Zr,Al)-oxide layer towards the oxide/alloy interface requires coupled currents of negatively charged O anions (as generated by dissociative chemisorption at the outer surface) and positively charged O “vacancies” (as generated by the steady-state dissolution of O anions from the oxide layer into the am-$Al_{0.44}Zr_{0.56}$ substrate, analogous to the thermal oxidation of pure crystalline (α-)Zr [41, 42]), as well as of electrons and electron holes (by thermionic emission, which is not considered to be rate-limiting at $T \geq 500$ °C [41, 43]). The significant solubility and diffusivity of oxygen in the am-$Al_{0.44}Zr_{0.56}$ alloy substrate relates to the intrinsically high solubility and diffusivity of oxygen in pure crystalline (α-)Zr,[2] which has an oxygen solubility of as high as 28.6 at.% in its pure form at 500 °C. A similar high oxygen solubility (about 7 at.% at

---

[2] The amount of oxygen that can be dissolved in α-Zr increases with increasing temperature: $O_{dissolv}$ (at.%) = 28.6 + exp(-6748T^{-1}+4.748) for $473 \leq T \leq 1478$ K [44]. The diffusion coefficient of oxygen in α-Zr ($D_V = 0.0661 \cdot 10^{-4} \cdot \exp(-184096/RT)$ in m^2/s) is 2.4×10^{-18} m^2/s at $T = 773.15$ K and 1.9×10^{-17} m^2/s $T = 833.15$ K [45].

900 °C [46]) was found in α_2-Ti_3Al, which relates to the high oxygen solubility in α-Ti (32 at.% O at 900 °C) [28, 47]. The large O solubility in Zr metal is in great contrast to the negligible O solubility in pure crystalline Al. Thus, it is expected that the O solubility limit decreases with increasing Al content in the amorphous AlZr solid solution, which has indeed been experimentally observed [37].

The oxidation process has induced considerable changes in the composition of the am-$Al_{0.44}Zr_{0.56}$ substrate in the vicinity of the formed oxide layer. For the oxidation experiments at T = 560 °C (see Section 4.3.2.3), Al enrichment in the alloy develops adjacent to the alloy/am-(Zr,Al)-oxide interface for oxidation times up to 45 minutes: see Figure 4.7b-d. Such gradual enrichment of Al at the reacting interface is induced by the preferential oxidation of Zr from the am-$Al_{0.44}Zr_{0.56}$ alloy (see above discussion) and the concurrent oxidation-induced (inward) migration of the am-(Zr,Al)-oxide/alloy interface. As shown in Figure 4.7d, the *decreased* O solubility limit of the Al-enriched region then induces expulsion of dissolved oxygen to larger depths in front of the Al-enrichment zone. These effects are less pronounced for the oxidation at the lower temperature of 500 °C, as the oxidation kinetics are much slower (cf. Figure 4.1c and Figure 4.7d).

After the formation of a closed amorphous (Zr,Al)-oxide layer, which acts as a diffusion-barrier layer for the reactants, a (diffusion-controlled) parabolic growth law is established with parabolic growth constants of $k_p = 4.92\times10^{-14}$ cm^2/s and $k_p = 2.62\times10^{-13}$ cm^2/s at 500 °C and 560 °C, respectively (see Figure 4.2). These parabolic growth constants for the external growth of the am-(Zr,Al)-oxide layer on the am-$Al_{0.44}Zr_{0.56}$ alloy are similar to the parabolic growth constants of $k_p^{Zr} = 1.41\cdot10^{-14}$ cm^2/s and $k_p^{Zr} = 4.69\cdot10^{-14}$ cm^2/s, as reported for oxide-layer growth on crystalline Zr at 500 °C and 550 °C [48]; the parabolic growth constant as reported for the oxidation of *crystalline* Al at 500 °C (at $p_{O_2} = 1\times10^4$ Pa), is significantly lower: $k_p^{Al} = 8.89\times10^{-18}$ cm^2/s [49]. [3] The parabolic oxidation rates are governed by the rate of oxygen diffusion through the thickening am-(Zr,Al)-oxide layer towards the oxide/alloy interface via the anion-“vacancy” exchange mechanism, as discussed above (for details, see Refs. [40, 41]) and in accordance with previous studies of the oxidation of Zr-based metallic glasses (see

---

[3] The parabolic growth constants were given in units of g^2/cm^{4}s in Refs. [48, 49]. These data have been recalculated here in units of cm^2/s by considering the densities of monoclinic ZrO_2 (5.73 g/cm^3) [50] and γ-Al_2O_3 (3.69 g/cm^3) [49], respectively.

Ref. [12] and references therein). The oxide-growth rate could be co-determined by the degree of Al-enrichment at the reacting alloy/am-(Zr,Al)-oxide, because this Al enrichment decreases the flux of dissolved O into the alloy substrate, thereby reducing the rate of O "vacancy" generation [41].

4.4.2 Stage II: interfacial nucleation of *t*-ZrO_2

After the initial formation and growth of an amorphous (Zr,Al)-oxide layer on the am-$Al_{0.44}Zr_{0.56}$ alloy (Stage I), *t*-ZrO_2 nanocrystallites nucleate in the alloy substrate close to the interface between the am-$Al_{0.44}Zr_{0.56}$ alloy and the external amorphous oxide layer: see Stage II and its enlarged part IIa in Figure 4.8 (see also Figure 4.4d). The development of *t*-ZrO_2 is only observed after 45 minutes of oxidation at 560 °C and not upon prolonged oxidation at 500 °C. This suggests that the barrier for *t*-ZrO_2 nucleation at the reacting interface can only be surmounted at 560 °C. Distinct differences in the compositional gradients develop at the reacting alloy/am-(Zr,Al)-oxide interface during the oxidation experiments at 500 °C and 560 °C. This can explain the exclusive nucleation of *t*-ZrO_2 at 560 °C, and not at 500 °C, as follows.

The nucleation of *t*-ZrO_2 in the O-dissolved zone in the alloy substrate involves the mechanism of internal oxidation in binary alloys in the presence of an external oxide scale (*here:* am-(Zr,Al)-oxide), as originally proposed by Wagner [51] and reviewed in, for example, Refs. [52, 53]. The internal formation of *t*-ZrO_2 in the am-$Al_{0.44}Zr_{0.56}$ alloy is thermally activated at locations in the alloy (i.e. at depths below the reacting oxide/alloy interface) for which the solubility product K_{sp} of *t*-ZrO_2 is exceeded: i.e. $(a_{\mathrm{Zr}}) \times (a_{\mathrm{O}})^2 > K_{sp}$, where a_{Zr} and a_{O} are the activities of Zr and O in the alloy at the given location (depth) below the original surface. Upon oxidation at 560 °C, a distinct enrichment of dissolved O builds up in front of the Al-enrichment zone at the reacting interface (this is not evident at 500 °C): see Figure 4.7d. Thereby the solubility product K_{sp} may be surpassed, which can trigger the internal formation of *t*-ZrO_2, in the region immediately below the region of Al enrichment. Indeed the enrichments of Al and the driven-away O at the reacting interface are largest, at successive depths, after 45 minutes of oxidation at 560 °C (Figure 4.7d), which coincides with the observed onset of nucleation of *t*-ZrO_2 at the corresponding depth below the interface (Figure 4.4). Hence, the nucleation of *t*-ZrO_2 for the oxidation at 560 °C is caused by oxidation-induced compositional changes in the alloy below the reacting interface. Indeed, significant O-enrichment in the substrate at the reacting alloy/oxide interface cannot be detected *after* the nucleation of *t*-ZrO_2. The above consideration disregards the barrier to oxide nucleation associated with the creation of new internal interfaces between crystalline oxide nuclei and the alloy matrix, which introduces excess Gibbs energies to the system and, more importantly, here likely rules the type of (metastable) oxide phase to nucleate first (*here: t*-ZrO_2, see below).

Formation of *t*-ZrO_2 at the amorphous-oxide/amorphous-alloy interface has also been reported for the oxidation of Zr-Al-(Cu,Ni) metallic glasses in Ref. [54]. However, in that case the nucleation of *t*-ZrO_2 was preceded by the nucleation of nanocrystallites of an *intermetallic* compound at the oxide/alloy interface, which may be attributed to (also) oxidation-induced compositional changes in the alloy substrate [54]. The intermetallic nanocrystallites can provide seeds for the heterogeneous nucleation of *t*-ZrO_2, because the energy of the interface between the intermetallic (nano)crystallites and the external amorphous oxide layer is higher than that of the interface between the *t*-ZrO_2 crystallites and the amorphous oxide [54]. In the present work, the nucleation of crystalline intermetallic phases in the am-$Al_{0.44}Zr_{0.56}$ alloy during oxidation does not occur (cf. Section 4.6.1 in the supporting information), i.e. the amorphous state of the am-$Al_{0.44}Zr_{0.56}$ alloy is fully preserved upon prolonged oxidation up to 560 °C.

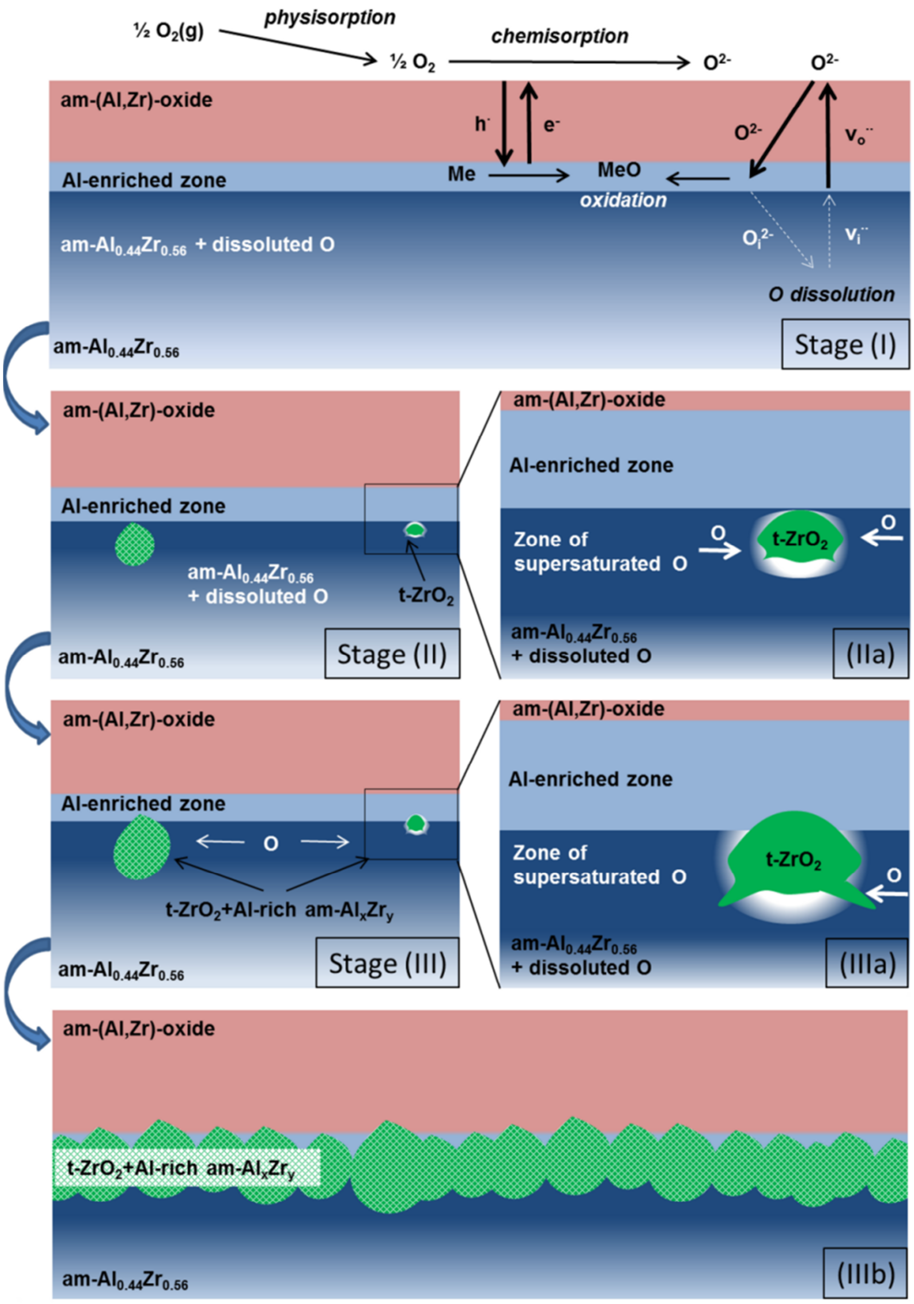

Figure 4.8: The oxidation mechanism of am-$Al_{0.44}Zr_{0.56}$: Schematic illustration of the oxidation stages of the am-$Al_{0.44}Zr_{0.56}$ alloy: **(I)** Growth of an amorphous (Al,Zr)-oxide layer of homogeneous composition and uniform layer thickness; pile-up of metallic Al in the substrate at the oxide/am-$Al_{0.44}Zr_{0.56}$ interface due to preferential oxidation of Zr followed by a region of O enrichment underneath (the oxygen is driven away from the region of Al enrichment due to reduced solubility of O), as observed at oxidation temperatures of 500 °C (up to an oxidation time of 300 minutes) and 560 °C (up to oxidation times of 45 minutes). **(II)** Nucleation of *t*-ZrO_2 at the amorphous oxide/am-$Al_{0.44}Zr_{0.56}$ alloy immediately underneath the Al-enriched zone due to local surpassing of the solubility product; **(IIa)**. **(III)** Further nucleation of *t*-ZrO_2 nuclei and growth of already formed *t*-ZrO_2 nuclei into the am-$Al_{0.44}Zr_{0.56}$ solid solution matrix: **(IIIa)**

fluctuations in the developing t-ZrO_2 morphology and the local compositions in the surrounding solid solution matrix (which is rich in Al and poor in Zr and O) destabilize the t-ZrO_2 growth front, resulting in a dendrite t-ZrO_2 morphology; **(IIIb)** the final state of the oxide microstructure, as developed upon oxidation of am-$Al_{0.44}Zr_{0.56}$ at 560 °C for 300 minutes: a laterally closed (quasi-)continuous oxide layer, consisting of interconnected t-ZrO_2 branches distributed in an Al-rich amorphous am-AlZr solid solution matrix, has formed below the amorphous oxide layer.

Bulk thermodynamics may be applied such that the crystalline oxide phase with the lowest (i.e. most negative) Gibbs energy of formation (per mole O) will preferentially be formed in O-supersaturated zones of the am-AlZr alloy (see Table 4.1). Consequently the formation of rhombohedral Al_2O_3 (α-Al_2O_3) should preferentially occur, although this thermodynamic preference is not very strong; compare the Gibbs energies of formation in Table 4.1. However, following Ostwald's rule of stages, the crystalline oxide phase that nucleates first may be a metastable polymorphic variant of the stable crystalline oxide phase, with energy closest to that of the initial state [55, 56]; for the present investigated system: cubic γ-Al_2O_3 (instead of α-Al_2O_3) [35] or t-ZrO_2 (instead of monoclinic α-ZrO_2) [27]. Remarkably, γ-Al_2O_3 and t-ZrO_2 have practically identical Gibbs energies of formation (see Table 4.1). It then follows that, thermodynamically, the nucleation of either γ-Al_2O_3 or t-ZrO_2 may be exclusively determined/selected by a relatively low interface energy of the oxide phase with the amorphous alloy matrix (see also Ref. [57]). The Zr-O bond strength is much higher than the Al-O bond strength,[4] which suggests a lower energy of the amorphous-alloy/t-ZrO_2 interface as compared to the amorphous-alloy/γ-Al_2O_3 interface (for a similar density of O at the two interface boundary planes [27]). It is thus concluded that the observed exclusive nucleation of t-ZrO_2 is ruled by interface energetics, in accordance with previously reported studies on the oxidation of pure crystalline Zr metal and (crystalline/amorphous) Zr-based alloys [59-61]. It has long been recognized that t-ZrO_2 nanocrystallites can be stabilized by their lower surface energy (as compared to the monoclinic phase) up to a critical crystallite size of roughly up to about 10 nm [62, 63]. It is conceivable that t-ZrO_2 nanocrystallites embedded in a foreign matrix can be

---

[4] The Zr–O bond dissociation energy of 753±21 kJ/mol is significantly higher than the Al-O bond dissociation energy of 481±8 kJ/mol [58].

stabilized up to even larger critical sizes by favorable interface energies with the surrounding matrix [27, 63].

4.4.3 Stage III: growth of dendritic-like *t*-ZrO_2

After nucleation of *t*-ZrO_2, the oxidation process at 560 °C (i.e. not at 500 °C) is characterized by the formation and growth of a (quasi-)continuous *t*-ZrO_2 interfacial layer below the external am-(Zr,Al)-oxide layer: see stage III in Figure 4.8. The (quasi-)continuous *t*-ZrO_2 interfacial layer consists of a branched structure of dendritically shaped *t*-ZrO_2 crystallites, immersed in an Al-enriched am-(Al,Zr) matrix phase.

After nucleation of the first *t*-ZrO_2 nanocrystallites in the alloy substrate close to the reacting interface (see Section 4.3.2), subsequent inward progression of the oxidation front is governed by the diffusional fluxes of dissolved O and metallic Zr in the alloy (amorphous solid solution) to continuously provide O and Zr concentrations (locally, where the *t*-ZrO_2 crystallites grow) in excess of those corresponding to the *t*-ZrO_2 solubility product in the alloy (see above and Refs. [52, 53]). The solubility of Al in *t*-ZrO_2 is negligibly small (< 2 at.% Al in monoclinic ZrO_2, even smaller in *t*-ZrO_2) [64, 65]. Consequently, nucleation and growth of *t*-ZrO_2 crystallites (by selective incorporation O and Zr from the supersaturated amorphous solid solution) is associated with the expulsion (segregation) of Al out of the region where the *t*-ZrO_2 crystal grows (see Figure 4.6). As a result, the growing *t*-ZrO_2 crystallites become embedded in an Al-enriched matrix, relatively poor in Zr and depleted in O, which impedes their further growth. Continued growth of the *t*-ZrO_2 crystals thus depends on local fluctuations of the evolving *t*-ZrO_2 crystallite morphology, as well as on (associated; see above) local compositional fluctuations in the surrounding alloy matrix. Local protrusions at the growing *t*-ZrO_2 surface, which are directed towards high dissolved-O concentrations, will preferentially grow and cause a destabilization of the growth front, resulting in a dendrite-like structure; see Stage III and its enlarged part IIIa in Figure 4.8 (see also Section 4.3.2.2). The developing *t*-ZrO_2 branches do not exhibit any distinct crystal facets, indicating that their morphology/growth is not governed by interface energetics. Corresponding nucleation and growth of further *t*-ZrO_2 proceeds until a laterally closed (quasi-)continuous interfacial *t*-ZrO_2 layer below the external am-(Zr,Al)-oxide layer has formed after an oxidation time of 300 minutes at 560 °C: see the relatively late development of Stage III in IIIb in Figure 4.8.

4.5 Conclusions

Upon (prolonged) oxidation of amorphous $Al_{0.44}Zr_{0.56}$ alloys at 500 °C and 560 °C under near-atmospheric conditions the alloy preserves its amorphous state. The oxidation mechanism can be subdivided into three stages:

Stage I: The formation of an amorphous (Zr,Al)-oxide layer of homogeneous composition and uniform layer thickness upon oxidation at 500 °C (up to 5 h) and 560 °C (up to 45 minutes). The amorphous oxide layers have the same nominal composition characterized by 10.8±0.8 at.% Al and 25.2±0.5 at.% Zr (balance O), practically independent of the oxidation time and temperature, which complies with a (local) minimum in the Gibbs energy of mixing for the homogeneous amorphous $(Al_2O_3)_x(ZrO_2)_y$ solid solution. The parabolic growth of the amorphous oxide layer is governed by the rate of oxygen diffusion via an anion-“vacancy” exchange diffusion mechanism.

An Al-enrichment in the alloy adjacent to the alloy/am-(Zr,Al)-oxide interface occurs upon oxidation at T = 560 °C for oxidation times up to 45 minutes, as induced by the preferential oxidation of Zr from the am-$Al_{0.44}Zr_{0.56}$ alloy. A concurrent expulsion of O from the region of Al enrichment to larger depths occurs as a consequence of a decreased O solubility in the Al-enriched solid solution.

Stage II: t-ZrO_2 nanocrystallites nucleate, after 45 minutes of oxidation at 560 °C, close to the interface between the am-$Al_{0.44}Zr_{0.56}$ alloy and the external amorphous oxide layer immediately underneath the region of Al enrichment. The nucleation of t-ZrO_2 at 560 °C is triggered by the supersaturation of the amorphous AlZr alloy in the O-enriched region with respect to the solubility product of t-ZrO_2. Neither bulk thermodynamics nor kinetics (Ostwald’s rule) can fully explain the exclusive occurrence of t-ZrO_2. The exclusive development of t-ZrO_2 can be ascribed to a favorable interface energy with the amorphous alloy matrix.

Stage III: Growth of the t-ZrO_2 crystallites (by selective incorporation of O and Zr from the supersaturated solid solution) is associated with the expulsion (segregation) of Al out of the region surrounding the growing t-ZrO_2 particles. As a result, the growing t-ZrO_2 crystallites become embedded in an Al-enriched matrix, poor in Zr and O, which impedes their further growth. Protrusions from the surface of the t-ZrO_2 crystallites preferentially grow towards oxygen-richer regions in the matrix and, consequently, the growth front becomes unstable and a dendrite morphology develops, governed by local fluctuations in the dissolved O concentration.

Acknowledgements

The authors are grateful to R. Völker for specimen preparation by magnetron sputtering, Dr. G. Richter for provision of thin-film facilities, U. Salzberger and W.-D. Lang for TEM specimen preparation, B. Siegle for AES investigation, K. Hahn for EFTEM investigation, Dr. F. Phillipp for part of the TEM investigation, and Prof. Dr. P.A. van Aken for provision of TEM facilities (all with MPI-IS).

4.6 Supporting Information

4.6.1 Characterizations of the as-deposited $Al_{0.44}Zr_{0.56}$ alloy

The X-ray diffraction (XRD) pattern (θ-2θ scan, Cu-$K\alpha$ radiation, Bruker D8 Discover diffractometer) of an as–deposited $Al_{0.44}Zr_{0.56}$ alloy is shown in Figure 4.9a; it reflects only a very broad intensity hump at 2θ ~ 36° (FWHM = 4.8°, fit with Topas Bruker AXS), which implies that the $Al_{0.44}Zr_{0.56}$ alloy is XRD amorphous. The bright field TEM (Philips CM 200, operated at 200 kV) image of a 50 nm thick as-deposited $Al_{0.44}Zr_{0.56}$ thin film[5] and the corresponding selected area electron diffraction pattern (SADP), shown in Figure 4.9b, reveal a homogenous phase structure in the bright field image and a diffuse amorphous halo in the corresponding SADP, and thereby confirm that the $Al_{0.44}Zr_{0.56}$ thin film is amorphous.

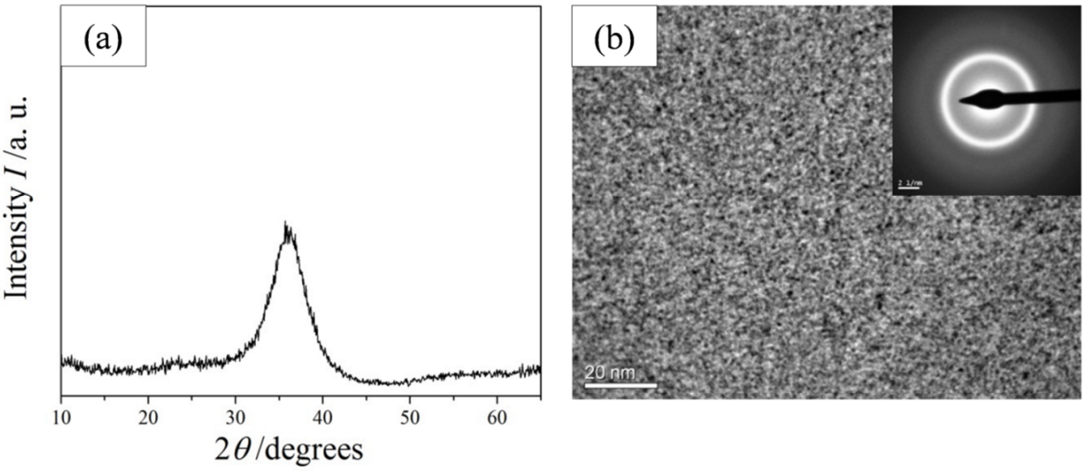

Figure 4.9: **(a)** XRD pattern (θ-2θ scan, Cu-$K\alpha$ radiation) recorded from the as-deposited am-$Al_{0.44}Zr_{0.56}$ alloy, **(b)** bright-field TEM micrograph of an as-deposited am-$Al_{0.44}Zr_{0.56}$ thin film. A selected area electron diffraction pattern (SADP) of the corresponding specimen is shown in the inset of (b).

---

[5] For the TEM characterization, approximately 50 nm thick am-$Al_{0.44}Zr_{0.56}$ thin films were sputter deposited for 4 minutes (using the same procedure as described in Sec. 2.1) onto a 20 nm thick amorphous SiO_2 membrane window (SIMPore Inc.).

4.6.2 Optical model fitting of the spectroscopic ellipsometry data; determination of the oxidation kinetics

To determine the oxidation kinetics from the measured spectra of $\Psi(\lambda, \varphi)$ and $\Delta(\lambda, \varphi)$, an optical model for the evolving alloy-substrate/oxide-layer system was constructed in the WVASE32 software package (version 3.770), which allowed linear-least squares fitting of measured and calculated spectra of $\Psi(\lambda, \varphi)$ and $\Delta(\lambda, \varphi)$, while employing the optical constants (i.e. the refractive index, $n(\lambda)$ and the extinction coefficient, $k(\lambda)$) and/or the thickness(es) of the formed oxide layer(s) as fit parameters. The constructed optical model incorporates an am-$Al_{0.44}Zr_{0.56}$ substrate covered with a double-layered structure, including an external (i.e. surface-adjacent) oxide layer of uniform thickness, L_{ox}, and an intermediate (interface-adjacent) layer of uniform layer thickness, L_{EMA}, which possesses optical properties in between those of the am-$Al_{0.44}Zr_{0.56}$ substrate and the surface oxide layer (see what follows).[6] The optical constants of the as-prepared am-$Al_{0.44}Zr_{0.56}$ alloy were straightforwardly determined at each wavelength from the experimentally measured $\Psi(\lambda, \varphi)$ and $\Delta(\lambda, \varphi)$ data of the as-deposited (i.e. non-oxidized)[7] am-$Al_{0.44}Zr_{0.56}$ specimen using a point-by-point fitting procedure in the WVASE software package (i.e. by fitting each wavelength separately with n and k as fit parameters). The refractive index $n(\lambda)$ of the transparent (i.e. $k(\lambda) = 0$ over the fitted wavelength range) surface oxide layer was described with a Cauchy function, i.e. $n(\lambda) = A+B/\lambda^2$, where A and B are constants. An effective medium approximation (EMA) layer, based on the Bruggeman formulation [66], was adopted to describe the optical properties of the intermediate layer, employing equal EMA fractions $f_{EMA} = 0.5$ for the optical constants of the surface oxide and the amorphous alloy. An EMA approach is generally applied to describe a wide range of “mixing” effects, such as surface and interface roughness, compositional or phase mixing and index of refraction grading [67]. In the present optical model, the intermediate EMA layer is introduced to account for the changes in the optical properties of the alloy at the reacting alloy/oxide interface,

---

[6] Note that the optical constants of the underlying Si substrate can be omitted in the optical model, because all light refracted in the 2 µm thick am-$Al_{0.44}Zr_{0.56}$ coating will be fully absorbed (i.e. the alloy coating can be conceived as an infinitely thick alloy substrate).

[7] In fact, the am-$Al_{0.44}Zr_{0.56}$ alloy substrate unavoidably possesses an *ultrathin* (below 3 nm) native oxide layer at its surface, which can be neglected in the present study, since only the (pseudo-)optical constants of the am-$Al_{0.44}Zr_{0.56}$ alloy substrate are required in the adopted data evaluation procedure.

as resulting from the combined processes of oxygen dissolution, preferential oxidation and phase mixing (see Sec. 4.3.3).

For each oxidation temperature, the measured spectra of $\Psi(\lambda, \varphi)$ and $\Delta(\lambda, \varphi)$ were simultaneously fitted for all oxidation times, while adopting a single set of Cauchy coefficients (A and B) and variable layer thicknesses L_{ox} and L_{EMA}. The thus obtained, optimized Cauchy constants equal A = 2.063, B = 0.02 µm^2 for an oxidation temperature of 560 °C and A = 2.033, B = 0.02 µm^2 for an oxidation temperature of 500 °C. Thus obtained exemplary values of the refractive index at $\lambda = 600$ nm are $n = 2.090$ at an oxidation temperature of 500 °C and $n = 2.119$ at an oxidation temperature of 560 °C. Hence the oxide layers formed at 500 °C and 560 °C have very similar optical properties. These refractive index values are considerably higher than that of α-Al_2O_3 ($n = 1.768$ at $\lambda = 600$ nm [68, 69]) and only slightly lower than that of crystalline t-ZrO_2 ($n = 2.192$ at $\lambda = 632.8$ nm [70]).

4.6.3 Cross-sectional TEM specimen preparation

A so-called 'Tripod polishing method' [71] was used to prepare cross-sectional TEM specimens. To this end, two pieces cut of the same specimen were glued together face-to-face (i.e. coating-side to coating-side). The thus-obtained sandwich was again cut into smaller pieces (2.5×1 mm^2). Next one side of a sandwich was plane-polished perpendicular to the glue plane (i.e. polish plane/plate perpendicular to the original film surface) until the specimen reached a thickness of 250 µm. The polishing was carried out with different grain-sized diamond lapping films, starting with 15 µm and ending with 0.5 µm grain size. Then the last polishing step was done with a soft felt pad wet by a colloidal silica suspension with a nominal grain size of 0.05 µm. Next the opposite (i.e. remaining non-polished) side of the specimen was polished with a slight tilting angle of 0.3° until interference fringes at the thinnest side of the now wedge-shaped specimen appeared (i.e. with a thickness below 10 µm). Finally ion-milling was performed using an Ar-ion polishing system (PIPSTM 691, Gatan) at 3 kV (13 mA) with an incident beam angle of 9°, until a hole was formed. At the edges of the ion-milled hole, electron transparent areas for cross-sectional TEM analysis had then been achieved.

4.6.4 Determination of the AES sensitivity factors

The employed relative sensitivity factors for metallic Al and Zr were straightforwardly determined for each measurement from the resolved peak-to-peak intensities recorded from the bulk am-$Al_{0.44}Zr_{0.56}$ alloy (i.e. using the recorded spectra at the end of each sputter-depth profile) and the known bulk composition. Relative sensitivity factors for oxidic Al, oxidic Zr and O were determined from the resolved peak-to-peak intensity ratios, as recorded under identical conditions from thermally-grown oxide scales on pure Al and Zr metal specimens (oxidation conditions: T_{ox}=500 °C, $pO_2=1\times10^5$ Pa, t_{ox}=300 minutes; see Sec. 4.2.2), assuming stoichiometric compositions for the grown Al_2O_3 and ZrO_2 layers. The relative O sensitivity factor was obtained as an average of the independently-determined relative sensitivity factors of O in Al_2O_3 and ZrO_2. This resulted in the following relative sensitivity factors S, with respect to pure Al (i.e. $S_{Al}=1$): $S_{Zr}=0.73$, $S_{Zr^{4+}}=0.56$, $S_{Al^{3+}}=0.67$, $S_O=1.16$.

4.7 References

[1] Inoue A., Takeuchi A., Acta Mater. **59** (2011) 2243.

[2] Wang W.H., Dong C., Shek C.H., Mater. Sci. Eng. R **44** (2004) 45.

[3] Inoue A., Sci. Rep. Res. Inst. Tohoku Univ. Ser. A-Phys. Chem. Metall. **42** (1996) 1.

[4] Zberg B., Uggowitzer P.J., Löffler J.F., Nat. Mater. **8** (2009) 887.

[5] Xing L.Q., Hufnagel T.C., Eckert J., Loser W., Schultz L., Appl. Phys. Lett. **77** (2000) 1970.

[6] Eckert J., Mattern N., Zinkevitch M., Seidel M., Mater. Trans. JIM **39** (1998) 623.

[7] Gebert A., Eckert J., Schultz L., Acta Mater. **46** (1998) 5475.

[8] Pekarskaya E., Löffler J.F., Johnson W.L., Acta Mater. **51** (2003) 4045.

[9] Liu C.T., Heatherly L., Easton D.S., Carmichael C.A., Schneibel J.H., Chen C.H., Wright J.L., Yoo M.H., Horton J.A., Inoue A., Metall. Mater. Trans. A **29** (1998) 1811.

[10] Xing L.Q., Li Y., Ramesh K.T., Li J., Hufnagel T.C., Phys. Rev. B **64** (2001) 180201.

[11] Eckert J., Das J., Pauly S., Duhamel C., J. Mater. Res. **22** (2007) 285.

[12] Köster U., Jastrow L., Mater. Sci. Eng. A-Struct. Mater. Prop. Microstruct. Process. **449** (2007) 57.

[13] Sun X., Schneider S., Geyer U., Johnson W.L., Nicolet M.A., J. Mater. Res. **11** (1996) 2738.

[14] Hsieh H.H., Kai W., Huang R.T., Pan M.X., Nieh T.G., Intermetallics **12** (2004) 1089.

[15] Zander D., Köster U., Mater. Sci. Eng. A-Struct. Mater. Prop. Microstruct. Process. **375** (2004) 53.

[16] Kimura H.M., Asami K., Inoue A., Masumoto T., Corros. Sci. **35** (1993) 909.

[17] Nijdam T.J., Jeurgens L.P.H., Sloof W.G., Mater. High. Temp. **20** (2003) 311.

[18] Kai W., Kao P.C., Lin P.C., Ren I.F., Jang J.S.C., Intermetallics **18** (2010) 1994.

[19] Wu Y., Song G.M., Nagase T., Umakoshi Y., J. Non-Cryst. Solids **357** (2011) 1136.

[20] Lim K.R., Park J.M., Park S.H., Na M.Y., Kim K.C., Kim W.T., Kim D.H., Appl. Phys. Lett. **104** (2014) 031604.

[21] Nijdam T.J., Jeurgens L.P.H., Sloof W.G., Acta Mater. **53** (2005) 1643.

[22] Panda E., Jeurgens L.P.H., Mittemeijer E.J., Corros. Sci. **52** (2010) 2556.

[23] Naumenko D., Gleeson B., Wessel E., Singheiser L., Quadakkers W.J., Metall. Mater. Trans. A **38A** (2007) 2974.

[24] Meier G.H., Jung K., Mu N., Yanar N.M., Pettit F.S., Abellan J.P., Olszewski T., Hierro L.N., Quadakkers W.J., Holcomb G.R., Oxid. Met. **74** (2010) 319.

[25] Liu L., Chan K.C., Appl. Phys. A-Mater. Sci. Process. **80** (2005) 1737.

[26] Hsieh H.H., Kai W., Jang W.L., Huang R.T., Lee P.Y., Wang W.H., Oxid. Met. **67** (2007) 179.

[27] Reichel F., Jeurgens L.P.H., Mittemeijer E.J., Acta Mater. **56** (2008) 659.

[28] Rahmel A., Schütze M., Quadakkers W.J., Mater. Corros. **46** (1995) 271.

[29] Soroka I.L., Vegelius J., Korelis P.T., Fallberg A., Butorin S.M., Hjorvarsson B., J. Nucl. Mater. **401** (2010) 38.

[30] Bakradze G., Jeurgens L.P.H., Mittemeijer E.J., J. Appl. Phys. **110** (2011) 024904.

[31] Lyapin A., Jeurgens L.P.H., Graat P.C.J., Mittemeijer E.J., J. Appl. Phys. **96** (2004) 7126.

[32] Egerton R.F. Electron Energy-Loss Spectroscopy in the Electron Microscope. New York: Plenum Press, 2011.

[33] Zhao C., Richard O., Bender H., Caymax M., De Gendt S., Heyns M., Young E., Roebben G., Van Der Biest O., Haukka S., Appl. Phys. Lett. **80** (2002) 2374.

[34] Teufer G., Acta Crystallogr. **15** (1962) 1187.

[35] Jeurgens L.P.H., Sloof W.G., Tichelaar F.D., Mittemeijer E.J., Phys. Rev. B **62** (2000) 4707.

[36] Jeurgens L.P.H., Wang Z.M., Mittemeijer E.J., Int. J. Mater. Res. **100** (2009) 1281.

[37] Weller K., Wang Z., Jeurgens L.P.H., Mittemeijer E.J., Acta Mater. **94** (2015) 134.

[38] Nijdam T.J., Jeurgens L.P.H., Sloof W.G., Acta Mater. **51** (2003) 5295.

[39] Chase Jr. M.W. NIST-JANAF Thermochemical Tables, 4th edition. Washington, DC: American Chemical Society, 1998.

[40] Nakamura R., Toda T., Tsukui S., Tane M., Ishimaru M., Suzuki T., Nakajima H., J. Appl. Phys. **116** (2014) 033504.

[41] Bakradze G., Jeurgens L.P.H., Acartürk T., Starke U., Mittemeijer E.J., Acta Mater. **59** (2011) 7498.

[42] Lyapin A., Jeurgens L.P.H., Mittemeijer E.J., Acta Mater. **53** (2005) 2925.

[43] Graat P.C.J., Somers M.A.J., Mittemeijer E.J., Z. Metallk. **93** (2002) 532.

[44] Abriata J.P., Garcés J., Versaci R., Bull. Alloy Phase Diagr. **7** (1986) 116.

[45] Ritchie I.G., Atrens A., J. Nucl. Mater. **67** (1977) 254.

[46] Dettenwanger F., Schumann E., Rakowski J., Meier G.H., Rühle M., Mater. Corros. **48** (1997) 23.

[47] Massalski T.B., Okamoto H., Subramanian P.R., Kacprzak L., editors. Binary alloy phase diagrams. Materials Park, Ohio: ASM International, 1990.

[48] Hussey R.J., Smeltzer W.W., J. Electrochem. Soc. **111** (1964) 564.

[49] Beck A.F., Heine M.A., Caule E.J., Pryor M.J., Corros. Sci. **7** (1967) 1.

[50] Hevesy G., Berglund V., J. Chem. Soc. **125** (1924) 2372.

[51] Wagner C., Z. Elektrochem. **63** (1959) 772.

[52] Rapp R.A., Corrosion **21** (1965) 382.

[53] Wallwork G.R., Rep. Prog. Phys. **39** (1976) 401.

[54] Lim K.R., Park J.M., Jee S.S., Kim S.Y., Kim S.J., Lee E.S., Kim W.T., Gebert A., Eckert J., Kim D.H., Corros. Sci. **73** (2013) 1.

[55] Threlfall T., Org. Process Res. Dev. **7** (2003) 1017.

[56] Schmalzried H., Z. Phys. Chemie-Int. J. Res. Phys. Chem. Chem. Phys. **217** (2003) 1281.

[57] Mittemeijer E.J. Fundamentals of Materials Science: The Microstructure–Property Relationship Using Metals as Model Systems. Berlin Heidelberg: Springer-Verlag, 2010.

[58] Darwent B.d.B. Bond dissociation energies in simple molecules. Washington: U.S. National Bureau of Standards, 1970.

[59] Bakradze G., Jeurgens L.P.H., Mittemeijer E.J., J. Phys. Chem. C **115** (2011) 19841.

[60] He L.F., Lin Z.J., Bao Y.W., Li M.S., Wang J.Y., Zhou Y.C., J. Mater. Res. **23** (2008) 359.

[61] Kai W., Ho T.H., Hsieh H.H., Chen Y.R., Qiao D.C., Jiang F., Fan G., Liaw P.K., Metall. Mater. Trans. A **39A** (2008) 1838.

[62] Garvie R.C., J. Phys. Chem. **69** (1965) 1238.

[63] Pitcher M.W., Ushakov S.V., Navrotsky A., Woodfield B.F., Li G.S., Boerio-Goates J., Tissue B.M., J. Am. Ceram. Soc. **88** (2005) 160.

[64] Stevens R. An Introduction to Zirconia. Twickenham UK: Magnesium Elektron Limited, 1986.

[65] Trinh D.H. Nanocrystalline Alumina-Zirconia Thin Films Grown by Magnetron Sputtering. Linköping University Electronic Presws: Linköping University, 2008.

[66] Woollam J.A. Guide to Using WVASE32^{TM}. Lincoln: J. A. Woollam Co., Inc., 2010.

[67] Vinodh M.S., Jeurgens L.P.H., Mittemeijer E.J., J. Appl. Phys. **100** (2006).

[68] M. N. Polyanskiy R.i.d., http://refractiveindex.info, accessed Jan. 23, 2014.

[69] Bass M., DeCusatis C., Enoch J., Lakshminarayanan V., Li G., MacDonald C., Mahajan V., Van Stryland E. Handbook of Optics, Third Edition Volume IV: Optical Properties of Materials, Nonlinear Optics, Quantum Optics: McGraw-Hill Professional, 2009.

[70] French R.H., Glass S.J., Ohuchi F.S., Xu Y.N., Ching W.Y., Phys. Rev. B **49** (1994) 5133.

[71] Ayache J., Beaunier L., Boumendil J., Ehret G., Laub D. Sample Preparation Handbook for Transmission Electron Microscopy: Methodology. Berlin: Springer, 2010.

Chapter 5

The effect of pre-oxidation treatment on the corrosion behavior of amorphous $Al_{1-x}Zr_x$ solid-solution alloys

Katharina Weller, T. Suter, Zumin Wang, Lars P. H. Jeurgens, Eric J. Mittemeijer

Abstract

The corrosion behavior of both as-deposited and pre-oxidized amorphous $Al_{1-x}Zr_x$ solid-solution alloys (x = 0.25, 0.32, 0.49, 0.65, 0.74) in 1 M HCl was investigated by the micro-electrochemical technique. The highly uniform microstructure of the sputter-deposited alloys is evidenced by the extreme reproducibility of consecutively measured potentiodynamic polarization curves on different surface areas (300 µm in diameter) of the same specimen. It was found that the native oxide layer on the **as-deposited** Al-rich $Al_{1-x}Zr_x$ alloys ($x < 0.49$) is much less stable upon anodization in 1 M HCl, which rapidly results in a total break-down of the protective character of the native Al-rich oxide layer. For higher Zr alloying contents, $x \geq 0.49$, the as-deposited alloys exhibit passive corrosion behavior due to the formation of a protective Zr-rich passive film on the *Zr-rich* alloy surface. The Al/Zr ratio in the resulting passive film is comparable to the Al/Zr ratio of the parent alloy. The **pre-oxidized** am-$Al_{1-x}Zr_x$ alloys all exhibited superior corrosion behavior as compared to their as-deposited pendants (without any sign of the onset of pitting corrosion), attaining passive current densities as low as 3.5×10^{-2} µA/cm^2 at 1000 mV. The superior corrosion resistance of the pre-oxidized alloys is attributed to a combination of characteristics of the thermally-grown amorphous $(Al_{0.33}Zr_{0.67})O_{1.83}$ overlayer: (*i*) a relatively high Zr fraction, (*ii*) a structurally and chemically uniform microstructure, (*iii*) a stable, minimal residual growth defect structure (in the surface region) established by a sufficiently large time of oxidation.

5.1 Introduction

Amorphous solid-solution alloys, which are constituted of a lower-melting-point metal M (e.g. Mg, Al, Cu, Ni) and a refractory metal R (e.g. W, Ta, Mo, Nb, Cr, Zr), further designated as am-$M_{1-x}R_x$ alloys, are known to provide unique material properties, such as superior corrosion resistance, high elastic strain limit, high strength and biocompatibility [1-3]. Generally, am-$M_{1-x}R_x$ solid-solution alloys cannot be prepared by conventional casting methods, because the melting point of the refractory metal by far exceeds the boiling point of the low-melting-point metal constituent and also the mutual solubility of M and R in the $M_{1-x}R_x$ liquid phase may be limited. Non-equilibrium processing routes, like mechanical alloying [4-6], ion beam mixing [7] and magnetron sputtering [8-10], are typically used to produce homogenous am-$M_{1-x}R_x$ solid-solution alloys, which are single-phase and fully amorphous over a relative large compositional range.

Al is a light metal and therefore Al-based alloys find manifold applications in technological areas where weight reduction is a major concern, such as in automotive and aerospace industries. Al metal provides good corrosion resistance in neutral environments, but actively dissolves in acidic and basic solutions and also is very susceptible to pitting corrosion in chloride-containing solutions [11, 12]. It has long been recognized that dissolution of a refractory metal like W, Ta, Mo, Nb, Cr or Zr in pure, crystalline Al (or Cu) drastically enhances its corrosion resistance, even in 1 M HCl solution (as typically used to evaluate the resistance of passivating metals and alloys to pitting corrosion) [3, 13, 14]. To realize high degrees of supersaturation, well beyond the solubility limit for crystalline Al, a homogenous *amorphous* solid-solution phase (instead of the (super)saturated crystalline fcc Al phase) can be applied which can be obtained by sputtering. For example, sputter-deposited $Al_{1-x}Zr_x$ alloys are amorphous over a relatively wide compositional range of $0.17 < x < 0.74$ [8, 15]. A high refractory-metal content in the am-$M_{1-x}R_x$ alloy, which is chemically interacting with the metal constituent in its first coordination shell [8], may block the active dissolution of the metal constituent from the am-$M_{1-x}R_x$ alloy and, at the same time, promote the formation of a structurally and compositionally uniform, passivating amorphous (oxyhydr-)oxide film in corrosive environments (see below and Refs. [13, 16-20]). Notably, corresponding *crystalline* $M_{1-x}R_x$ alloy modifications contain grain boundaries, dislocations and (possibly) phase boundaries, which can act as initiation sites for pitting corrosion [13, 15]. Hence, from a scientific point of view, am-$M_{1-x}R_x$ alloys offer a unique possibility to investigate (and to utilize) the sole effects of the alloy composition and the passive-film microstructure on the corrosion behavior [15].

The present study addresses the *local* corrosion behavior of both as-deposited and pre-oxidized amorphous $Al_{1-x}Zr_x$ solid-solution alloys of various compositions ($x = 0.25$, 0.32, 0.49, 0.65, 0.74; as prepared by magnetron sputtering) in 1 M HCl solution (pH = 0) by application of the electrochemical microcapillary technique [21-23]. The microcapillary method enables local measurements of (electrochemical) corrosion currents on a selected, very small area of the surface of the specimen (in this study: 300 µm in diameter) at an extraordinarily high current resolution in the fA range [21-23]. This is not possible for conventional electrochemical scanning techniques, where a much larger area of the specimen surface is immersed in the electrolyte (immersed area in the range of mm^2-cm^2). The electrochemical microcapillary technique thus allows assessment of the *intrinsic* corrosion behavior of passivating metal and alloy surfaces, which is not possible with large-scale electrochemical scanning methods for which, consequently, the measured corrosion behavior is generally affected by scratches, contaminations, local defects and other heterogeneities within the immersed area of the surface of the specimen.

Notably, Al has a considerably higher affinity for O (i.e. it has a much lower electronegativity) than e.g. Cu and Ni. Hence, whereas passive (oxyhydr-)oxide films (further denoted as *passive films*) on e.g. $Cu_{1-x}Zr_x$ and $Ni_{1-x}Zr_x$ alloys are mainly composed of Zr-(hydr-)oxide (thus resembling the good corrosion behavior of the Zr metal), passive films on $Al_{1-x}Zr_x$ alloys contain both Al and Zr cations [14, 15, 24, 25]. As already mentioned above, Al possesses poor corrosion resistance in chloride-containing solutions and superior corrosion resistance of the passivated $Al_{1-x}Zr_x$ alloy surface in 1 M HCl can only be provided when Al and Zr cations are *homogenously distributed* in the passive film (and thus no local Al enrichment occurs). According to the so-called graph theory [17, 18], under the above constraint of a homogenous film, a minimum (critical) Zr-cation fraction, $f_{\mathrm{Zr}}^{\mathrm{crit}}$, is required: $f_{\mathrm{Zr}}^{\mathrm{crit}} = n_{\mathrm{Zr^{ox}}}/(n_{\mathrm{Al^{ox}}} + n_{\mathrm{Zr^{ox}}}) \geq 0.16$ (where $n_{\mathrm{Al^{ox}}}$ and $n_{\mathrm{Zr^{ox}}}$ denote the molar fractions of Al and Zr in the passive film) in order to establish an *interconnected* network of -Zr-O(H)-Zr- bonding bridges, which are assumed to provide passivity of the $Al_{1-x}Zr_x$ alloy surface due to their enhanced chemical stability in acidic environments (as compared to –Al-O(H)-Al bonding bridges) [26]. In practice, even for $f_{\mathrm{Zr}}^{\mathrm{crit}} \geq 0.16$, local Al-enrichments in the passive film (i.e. by local phase separation) may exist and initiate pitting corrosion (since Al-oxide and Al-hydroxide phases are easily dissolvable at low *p*H) [9].

A recent study by our group on the thermal oxidation of the am-$Al_{1-x}Zr_x$ alloys has reported the thermodynamically-preferred formation of an amorphous ternary oxide phase with a singular homogenous composition of $(Al_{0.33}Zr_{0.67})O_{1.83}$, which is stable up to 500 °C [25]. Strikingly, the amorphous state and the composition of the thermally-grown $(Al_{0.33}Zr_{0.67})O_{1.83}$ solid-solution oxide phase are constant over a broad compositional range of the am-$Al_{1-x}Zr_x$ alloy ($0.32 \leq x \leq 0.74$) [25]. This thermally-stable, highly uniform amorphous $(Al_{0.33}Zr_{0.67})O_{1.83}$ overlayer could thus provide excellent corrosion resistance to the parent am-$Al_{1-x}Zr_x$ alloy substrate over this wide composition range (i.e. $0.32 \leq x \leq 0.74$). Therefore, in the present study, the corrosion behaviors of as-deposited and pre-oxidized am-$Al_{1-x}Zr_x$ alloys in 1 M HCl solution are investigated and compared as function of the composition parameter x. To the best of our knowledge, up to date, only few studies on the corrosion behavior of am-$Al_{1-x}Zr_x$ alloys (in chloride-containing solutions) have been reported, which show that the corrosion resistance increases with increasing Zr content in both the alloy and in the passive (Al,Zr)-oxyhydroxide film [3, 9, 14, 15]. However, in these previous studies, the effect of a controlled pre-oxidation treatment on the intrinsic corrosion behavior was not addressed. Moreover, all am-$Al_{1-x}Zr_x$ alloys studied until now exhibit pitting corrosion at high anodization potentials [14, 15] (which is not the case for am-$Al_{1-x}Zr_x$ alloys in the present study; see Sec. 5.3), indicating that the measurements reported in the literature were affected by compositional and/or structural inhomogeneities, scratches, contamination and/or other local defects in the as-deposited alloy and/or its passive oxide film.

5.2 Experimental procedures and data evaluation

5.2.1 Specimen preparation and oxidation

Amorphous $Al_{1-x}Zr_x$ (am-$Al_{1-x}Zr_x$) alloys in the form of 2 µm thick coatings were deposited by magnetron co-sputtering from pure elemental targets (Al: 99.9995 wt.%, Zr: 98.5 wt.%) on Si(100) wafers, which were pre-coated with an am-SiO_2 layer and an am-Si_3N_4 top layer, each 50 nm thick. Sputter deposition was performed in an ultrahigh-vacuum (UHV) sputter chamber by applying a constant power of 100 W to the Zr target and different constant powers to the Al target (P_{Al} = 20, 28, 53, 101, 147 W), resulting in the following alloy compositions: am-$Al_{0.26}Zr_{0.74}$, am-$Al_{0.35}Zr_{0.65}$, am-$Al_{0.51}Zr_{0.49}$, am-$Al_{0.68}Zr_{0.32}$, am-$Al_{0.75}Zr_{0.25}$ (as analyzed by inductively coupled plasma optical emission spectroscopy (ICP-OES)). Pure Zr and Al metal layers were deposited at target powers of 150 W and 200 W, respectively. Prior to deposition, the wafer surfaces were sputter-cleaned in-situ for 1 min by exposure to a low-energetic Ar^+ plasma. During deposition, specimen rotation was applied at a rotation speed of a few tens of cycles per minute. For a detailed description of the deposition process, see Ref. [25].

Pre-oxidation of the as-deposited am-$Al_{1-x}Zr_x$ (x = 0.25, 0.32, 0.49, 0.65, 0.74) alloys at a selected oxidation temperature, T_{ox}, in the range of 350 °C ≤ T_{ox} ≤ 400 °C was performed by enclosing specimen pieces (~ 7×14 mm^2) in a quartz ampoule (filled with pure oxygen at an oxygen pressure equivalent to $pO_2 = 1\times10^5$ Pa at T_{ox}) and subsequently introducing them into a preheated sandbath (TECHNE FB-08c). A detailed description of the oxidation procedure is given in Ref. [25].

5.2.2 Microstructural analysis

X-ray diffraction (XRD) analysis was applied to determine the phase constitution of the as-deposited and pre-oxidized am-$Al_{1-x}Zr_x$ specimens. To this end, θ-2θ scans were recorded over a 2θ-range of 10° to 65° in parallel-beam geometry on a Bruker D8 Discover diffractometer equipped with a Cu X-ray anode (40 kV/30 mA; Cu-$K\alpha$ radiation, λ = 1.54056 Å) with an X-ray lens in the primary beam path and a parallel-plate collimator and an energy-dispersive detector in the diffracted beam path [25, 27].

The chemical constitutions of the passive oxide layers formed on the as-deposited and pre-oxidized am-$Al_{1-x}Zr_x$ alloys in the ambient (i.e. the native oxide) and of those formed after anodization in 1 M HCl (see Sec. 5.2.3) were investigated by X-ray photoelectron spectroscopy (XPS) utilizing a Thermo VG Thetaprobe system (base pressure < $2\cdot10^{-8}$ Pa) applying monochromatic Al Kα radiation ($h\nu$ = 1486.68 eV, analysis area ~400 µm in diameter). To this end, the core-level spectra of the Al 2p (binding energy (BE) range: 67 - 83 eV), Zr 3d (BE range: 173 - 190 eV) and O 1s (BE range: 526 - 539 eV) photoelectron lines were recorded with a step size of 0.1 eV at a constant pass energy of 50 eV. The measured core-level spectra were first corrected for the analyzer transmission function after which a Shirley-type background was subtracted to correct for the background of inelastically scattered electrons. Next the (oxidic and hydroxidic[1]) O 1s and the (metallic and oxidic) Al 2p and Zr 3d chemical states were resolved by linear-least-squares peak fitting of the thus corrected spectra using the Thermo Scientific™ Avantage™ software. Quantification of the resolved peak-area intensities was performed using the same software (adopting the sensitivity factors supplied by the manufacturer).

The microstructure of the oxide layer formed on the pre-oxidized am-$Al_{1-x}Zr_x$ alloys, as well as the corresponding oxidation-induced compositional change in the parent alloy, were investigated by a combinatorial experimental approach, applying XPS (see above), Auger electron spectroscopy (AES), high-resolution transmission electron microscopy (HR-TEM) and spectroscopic ellipsometry: for details of the data acquisition and quantification procedures, the reader is referred to Refs. [24, 25, 29]. (In addition to the XPS analysis (see above) correspondingly detailed microstructural analysis of the native oxide layer on am-$Al_{1-x}Zr_x$ alloys has not been performed). In brief, composition-depth profiles of the oxide layer formed on the pre-oxidized am-$Al_{1-x}Zr_x$ alloys were recorded by Auger electron spectroscopy (AES) sputter-depth profiling using a JEOL JAMP 7830F Scanning Auger Microscope [25]. The microstructure, morphology and chemical composition of the pre-oxidized am-$Al_{1-x}Zr_x$ alloys were studied by cross-sectional transmission electron microscopy (TEM) analysis using a JEOL JEM-ARM200F scanning transmission electron microscope operating at 200 kV: see Ref. [24]. The thicknesses of the oxide layers grown by thermal oxidization on the am-$Al_{1-x}Zr_x$ coatings were determined by spectroscopic ellipsometry (SE) using a J. A. Woollam M-2000 spectroscopic ellipsometer [29].

5.2.3 Microscale electrochemical measurements

Microelectrochemical measurements were carried out on as-deposited and oxidized am-$Al_{1-x}Zr_x$ alloys using the electrochemical microcapillary technique [21-23, 30]. A schematic drawing of the experimental setup and microcell used in the experiments is shown in Figure 5.1. The microcell consists of a tapered glass capillary (with a diameter of 300 µm at the very tip), which is filled with the electrolyte (1 M HCl, *p*H = 0). The glass capillary has a silicon seal at the periphery of the very tip to hinder leaking out of electrolyte solution upon contacting the specimen surface. The microcell connects the

---

[1] By XPS it is possible to distinguish between O1s oxide and hydroxide signals [28]. The formation of a surficial hydroxide layer/phase (see Figure 5.3) on am-$Al_{1-x}Zr_x$ (before the anodization in 1 M HCl) is very likely due to storage at ambient conditions.

working electrode (i.e. the am-$Al_{1-x}Zr_x$ specimen) and the Pt counter electrode. All potentials are determined with respect to a saturated calomel electrode (SCE), which is connected to the microcell via an electrolytic bridge. For each measurement, first the microcell was carefully positioned on the specimen surface (selecting an optically perfect area using an optical microscope), after which the open circuit potential[2] (OCP) was recorded for 5 minutes. Next potentiodynamic polarization curves (i.e. the current density as a function of the applied potential) were recorded at a scan rate of 1 mVs^{-1} starting from a potential -250 mV below the recorded OCP. To examine the possible influence of surface heterogeneities on the (intrinsic) corrosion behavior and also to test the measurement reproducibility, a minimum of three different locations were measured on each specimen surface.

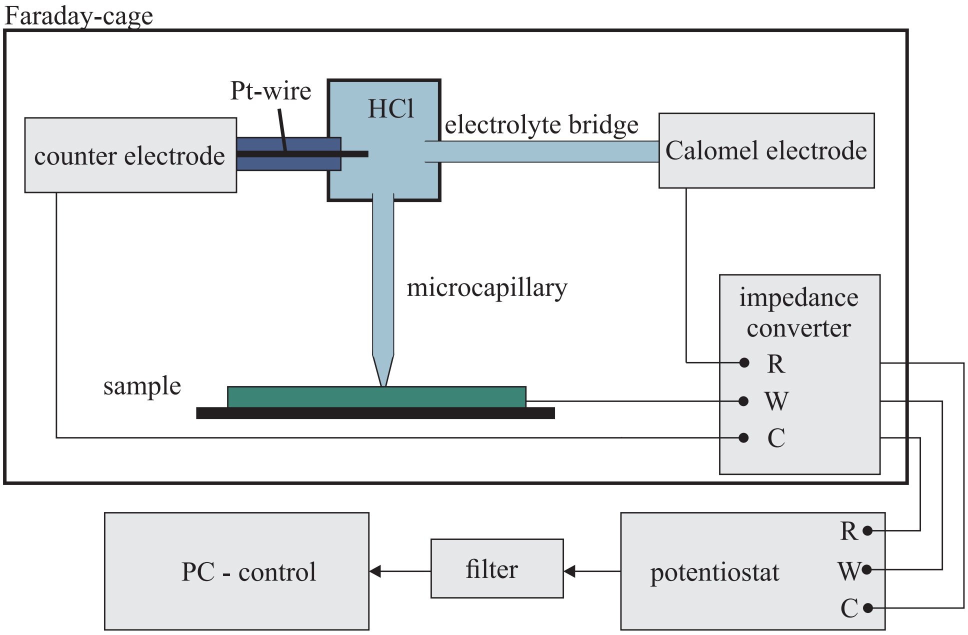

Figure 5.1: Schematic drawing of the experimental setup of the micro-electrochemical capillary technique (R: reference electrode, W: working electrode, C: counter electrode) (redrawn from [22]).

---

[2] The open circuit potential (OCP) is the potential of the working electrode (i.e. the specimen in contact with the electrolyte) relative to that of the reference electrode, in absence of an externally applied potential.

5.3 Results and Discussion

5.3.1 Microstructure of the as-deposited and pre-oxidized am-$Al_{1-x}Zr_x$ alloys

5.3.1.1 As-deposited am-$Al_{1-x}Zr_x$ alloys

A detailed experimental study of the atomic and electronic structure of the sputter-deposited am-$Al_{1-x}Zr_x$ alloys has been reported recently, showing that the am-$Al_{1-x}Zr_x$ alloys are XRD and TEM amorphous over the studied compositional range from $0.25 \leq x \leq 0.74$: see Ref. [8] and the diffractograms in Figure 5.2. The chemical composition of the native (air-formed) oxide layer on the am-$Al_{1-x}Zr_x$ alloys (prior to exposure to the electrolyte solution) has been studied by XPS (see Sec. 5.2.2). Exemplary reconstructions of the recorded Zr 3d, Al 2p and O1s core-level spectra of the as-deposited am-$Al_{0.51}Zr_{0.49}$ alloy are shown in Figure 5.3a, b and c, respectively. The XPS determined Al^{ox}/Zr^{ox} cationic ratios in the native oxide layer for the various (ICP-OES determined) alloy compositions are shown in Figure 5.4.

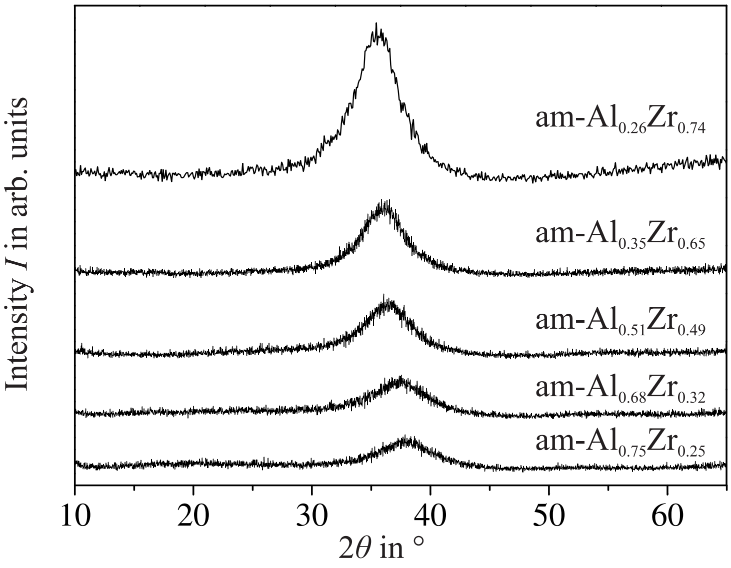

Figure 5.2: X-ray diffraction patterns (Cu-$K\alpha$ radiation) of the as-deposited $Al_{1-x}Zr_x$ alloys (x = 0.25, 0.32, 0.49, 0.65, 0.74) (adapted from [25] and extended).

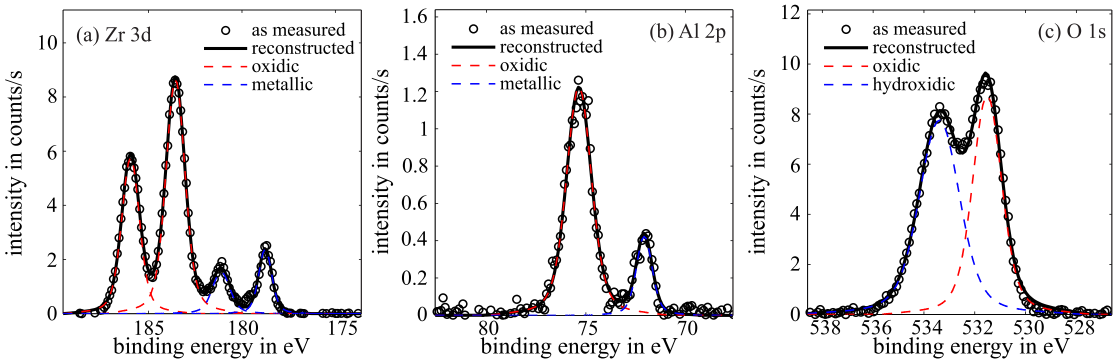

Figure 5.3: Reconstructions of the **(a)** Zr 3d, **(b)** Al 2p and **(c)** O 1s spectra, as recorded from the as-deposited am-$Al_{0.51}Zr_{0.49}$ alloy (as covered with a native oxide layer) by XPS.

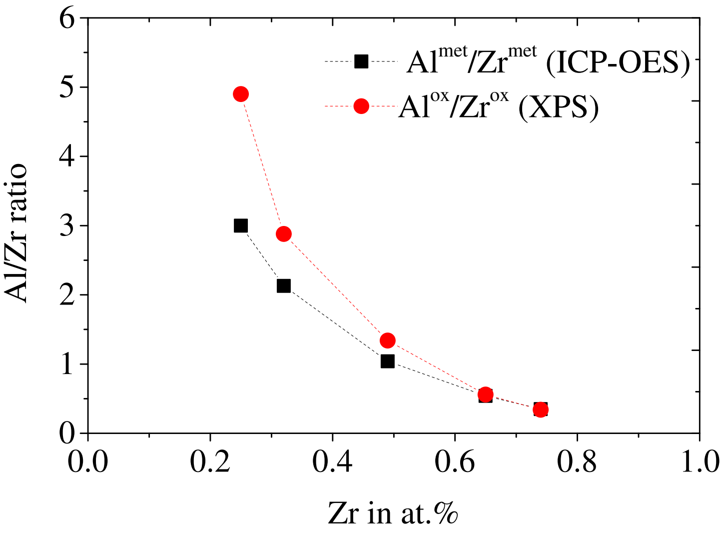

Figure 5.4: The metallic Al/Zr ratio in the am-$Al_{1-x}Zr_x$ alloy substrate (Al^{met}/Zr^{met}) as determined by ICP-OES measurements and the oxidic Al/Zr ratio in the native oxide layer as determined by XPS measurements, both as function of the atomic percentage of Zr in the substrate as determined by ICPS-OES.

It follows that the Al^{ox}/Zr^{ox} ratio in the native oxide film overall decreases with increasing Zr content in the am-$Al_{1-x}Zr_x$ alloy. For the Zr-rich am-$Al_{1-x}Zr_x$ alloys, the Al^{ox}/Zr^{ox} ratio of the native oxide layer is practically equal to the Al/Zr ratio of the bulk alloy, whereas for Al-rich am-$Al_{1-x}Zr_x$ alloys ($x \leq 0.49$) the native oxide film is enriched in Al as compared to the bulk alloy. This enrichment of Al in the native oxide film (as compared to the parent alloy) is attributed to the preferential oxidation of Al during the very fast (almost instantaneous) passivation of the Al-rich am-$Al_{1-x}Zr_x$ surfaces after their removal from the high-vacuum sputter chamber and exposure to air.

5.3.1.2 Pre-oxidized am-$Al_{1-x}Zr_x$ alloys

As discussed in Ref. [25], thermal oxidation of the am-$Al_{1-x}Zr_x$ alloys, for various alloy compositions ($0.32 \leq x \leq 0.74$) and oxidation temperatures in the range of $350 \leq T_{ox} \leq 500$ °C, results in the formation of an oxide layer of uniform thickness, which is composed of an amorphous oxide solid-solution phase with a singular composition of $(Al_{0.33}Zr_{0.67})O_{1.83}$, further denoted as am-$(Al_{0.33}Zr_{0.67})O_{1.83}$ overlayer. The amorphous state, the homogenous composition and the uniform thickness of the am-$(Al_{0.33}Zr_{0.67})O_{1.83}$ overlayer is evidenced by cross-sectional TEM analysis of the pre-oxidized am-$Al_{0.51}Zr_{0.49}$ alloy (after 10 hrs of pre-oxidation at 350 °C): see Figure 5.5. EELS elemental mapping of the TEM cross-section reveals a highly uniform distribution of Al, Zr and O in the am-$(Al_{0.33}Zr_{0.67})O_{1.83}$ overlayer: see Figure 5.5c, d and e. No phase separation in the oxide overlayer nor a devitrification of the parent alloy substrate could be detected (not even at the subnanometer scale): see Figure 5.5f.

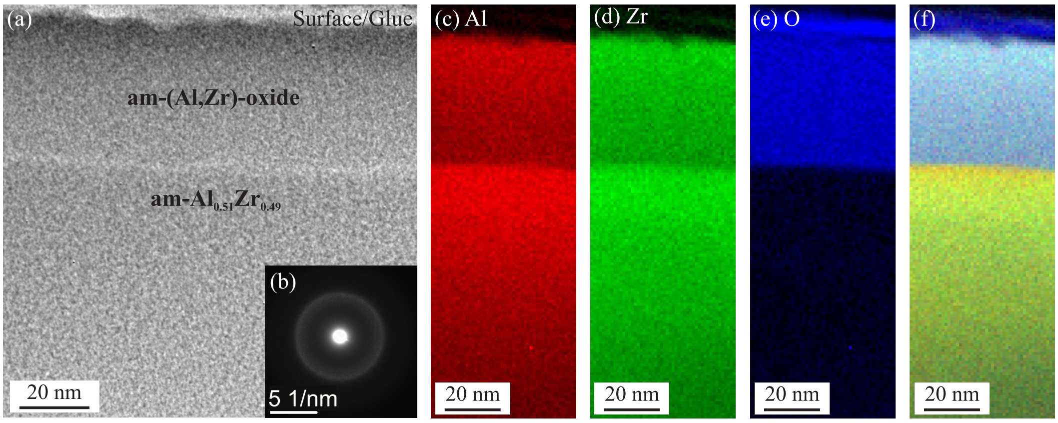

Figure 5.5: (a) Cross-sectional bright-field TEM image of am-$Al_{0.51}Zr_{0.49}$ oxidized at 400 °C for 10 h and **(b)** the corresponding selected area diffraction pattern (SADP), comprising both the amorphous alloy and the amorphous oxide phase (aperture diameter: ~ 130 nm). EELS elemental maps of **(c)** Al, **(d)** Zr, **(e)** O and **(f)** their combined image (O + Al + Zr) pertaining to the TEM cross-section of (a) (adapted from [25] and extended).

Composition-depth profiles of the pre-oxidized am-$Al_{0.35}Zr_{0.65}$, am-$Al_{0.51}Zr_{0.49}$ and am-$Al_{0.68}Zr_{0.32}$ alloys (as measured by AES) confirm the highly uniform distribution of Al, Zr and O also as a function of depth in the am-$(Al_{0.33}Zr_{0.67})O_{1.83}$ overlayers, as grown on the *Zr-rich* am-$Al_{1-x}Zr_x$ alloys: see Figure 5.6a (for $x = 0.65$) and Figure 5.6b (for $x = 0.49$). The am-$(Al_{0.33}Zr_{0.67})O_{1.83}$ overlayer on the *Al-rich* am-$Al_{0.68}Zr_{0.32}$ alloy exhibits an Al-enrichment at its outer surface (as compared to the Al^{ox}/Zr^{ox} cation ratio of 0.5 for the $(Al_{0.33}Zr_{0.67})O_{1.83}$ phase): see Figure 5.6c (for $x = 0.32$) and Ref. [25]. Such Al-enrichment at the oxidized alloy surface could affect the passivating corrosion behavior; see further Sec. 5.3.2.3.

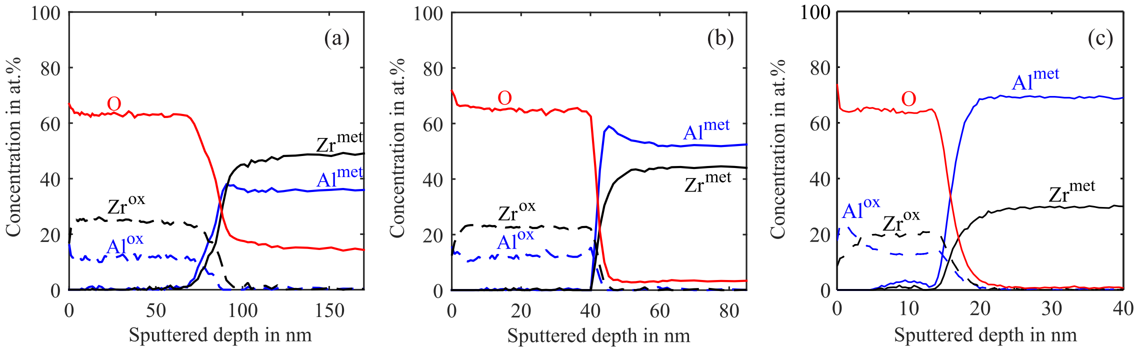

Figure 5.6: Composition-depth profiles of the **(a)** am-$Al_{0.35}Zr_{0.65}$, **(b)** am-$Al_{0.51}Zr_{0.49}$ and **(c)** am-$Al_{0.68}Zr_{0.32}$ alloys, all oxidized at 400 °C for 10 h, as recorded by AES sputter-depth profiling (adapted from [25] and extended).

5.3.2 Corrosion behavior of the am-$Al_{1-x}Zr_x$ alloys

5.3.2.1 Corrosion measurement characteristics and reproducibility

The micro-electrochemical technique enables potentiodynamic measurements of the kinetics of localized corrosion since only a small area of the specimen surface (*here:* 300 µm in diameter; see Sec. 5.2.3) is exposed to the electrolyte. The superior corrosion behavior of am-$M_{1-x}R_x$ solid-solution alloys is generally attributed to the absence of surface heterogeneities, since the am-$M_{1-x}R_x$ alloys and their passive films are supposed to be structurally and compositionally uniform. This implies that a series of potentiodynamic polarization curves, which are successively measured, by the micro-electrochemical technique, at different, small areas on the as-deposited or pre-oxidized am-$Al_{1-x}Zr_x$ alloy surface, should show similar (*intrinsic*) corrosion behaviors. Exemplary potentiodynamic polarization curves, as recorded at different surface areas on an as-deposited am-$Al_{0.68}Zr_{0.32}$ alloy and on a (at 350 °C for 10 h) pre-oxidized am-$Al_{0.51}Zr_{0.49}$ alloy, are presented in Figure 5.7a and b, respectively. Indeed, except for usual variation in the open circuit potential (OCP),[3] the measured potentiodynamic polarization curves are almost identical for a given alloy composition and surface condition, irrespective of the chosen measurement area on the specimen surface.

Evidently, by comparing Figure 5.7a and Figure 5.7b, the as-deposited am-$Al_{0.68}Zr_{0.32}$ alloy is less corrosion resistant (i.e. it exhibits a much higher current density in the passive regime) than the pre-oxidized am-$Al_{0.51}Zr_{0.49}$ alloy (for detailed discussion, see Sec. 5.3.2.3).

Since, for a given alloy composition and surface condition, the potentiodynamic measurements by the micro-capillary technique were always highly reproducible, only representative (instead of all repetitive) measurements for each alloy composition and surface condition will be displayed in the following sections.

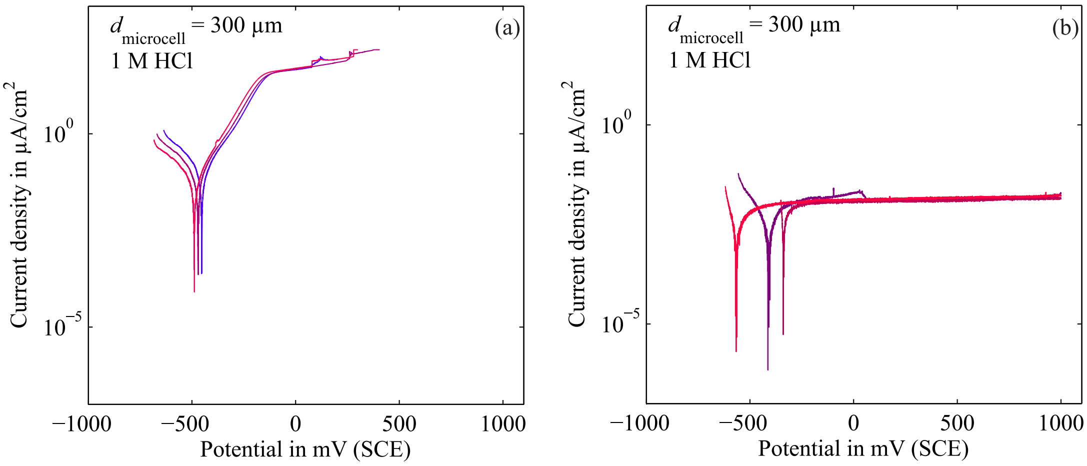

Figure 5.7: Potentiodynamic polarization curves of **(a)** the as-deposited am-$Al_{0.68}Zr_{0.32}$ alloy and **(b)** the oxidized am-$Al_{0.51}Zr_{0.49}$ alloy (oxidized for 10 h at 350 °C), as measured by the micro-capillary technique (in a 1 M HCl electrolyte solution).

---

[3] In particular for passive metals and alloys, the open circuit potential is variable, because of the extremely low anodic reaction rates, which makes the open circuit potential very susceptible to tiny variations in the cathodic reactivity by e.g. local concentration gradients of e.g. dissolved oxygen and chloride ions in the electrolyte solution, surface contamination, temperature variation, etc [31]. As observed in Figure 5.7, such shifts of the open circuit potential are not accompanied with change of the overall shape of the potentiodynamic polarization curves.

5.3.2.2 Corrosion behavior of the as-deposited am-$Al_{1-x}Zr_x$ alloy

The corrosion behavior of as-deposited am-$Al_{1-x}Zr_x$ alloys (i.e. with an air-formed native oxide film on its surface, further denoted as *native oxide film*) as function of the alloy composition (i.e. x = 0.26, 0.35, 0.51, 0.68, 0.75) was investigated by the micro-electrochemical technique (see Sec. 5.2.3). As examples the potentiodynamic polarization curves recorded from the as-deposited am-$Al_{1-x}Zr_x$ (x = 0.74, 0.49, 0.25) alloys in 1 M HCl (pH = 0) are shown in Figure 5.8a. The potentiodynamic polarization curves of the sputter-deposited (pure, polycrystalline) Al and Zr references have also been plotted in this figure for comparison.

The potentiodynamic polarization curves, as recorded for all investigated alloys, all exhibit an increase of the current density (directly above OCP) with increasing potential upon anodization in 1 M HCl (pH = 0). Al oxide is only stable in the pH range from 4 to 9 and dissolves easily in hydrochlorid acid with pH = 0 [32-35]. Consequently, a break-down of the native Al oxide layer on pure, crystalline Al in 1 M HCl (at pH = 0) is expected. Indeed, the sputter-deposited pure, crystalline Al layer (covered with a native amorphous Al oxide layer with a thickness of few nm; cf. Ref. [36]) exhibits an initial, fast increase of the current density (> OCP), rapidly followed by a total break-down (i.e. steep rise of the current density out of the measurement scale[4]) of the protective character of the native Al-oxide layer. A passive corrosion behavior, as characterized by small to very small current densities (below 10^0 µA/cm^2) in the anodic region at, say, 200 mV above the OCP, sets in with increasing Zr alloying content of the am-$Al_{1-x}Zr_x$ alloys and is most pronounced for pure crystalline Zr (see Figure 5.8a).

The enhancement of the corrosion resistance of the am-$Al_{1-x}Zr_x$ alloy with increasing Zr alloying content has been illustrated by plotting the measured current density at an applied potential of +200 mV above the OCP as function of the Zr alloying content in Figure 5.8b. A distinct decrease of the anodic current density with increasing alloying Zr content, which is concomitant with an increasing Zr content in the native oxide layer (see Sec. 5.3.1.1 and Figure 5.4), is observed: from 1.5×10^2 µA/cm^2 for pure crystalline Al to 9.1×10^{-1} µA/cm^2 for am-$Al_{0.51}Zr_{0.49}$ (and to 2.7×10^{-2} µA/cm^2 for pure crystalline Zr). It is concluded that the formation of a *protective* passive film on the am-

---

[4] In the applied measurement setup, the upper limit of the current density was set to 10^2 µA/cm^2. In reality, even higher current densities are expected for Al metal in 1 M HCl solution.

$Al_{1-x}Zr_x$ alloy surfaces in 1 M HCl requires a minimum (critical) Zr alloying content of $x \geq 0.49$ (based on a criteria of a passive current density < 10^0 µA/cm^2 in the anodic region 200 mV above the OCP; see Figure 5.8b).

For the am-$Al_{1-x}Zr_x$ alloys with $x \geq 0.49$, the respective passive current density at an applied potential of about 500 mV (vs. SCE) attains a somewhat higher, but nearly constant, current density of about 2×10^1 µA/cm^2, independent of the alloy composition. The value of this constant passive current density is similar to that of stainless steel [22] and also comparable to the measured current density of the sputter-deposited Zr metal at a potential of 1000 mV: see Figure 5.8a.

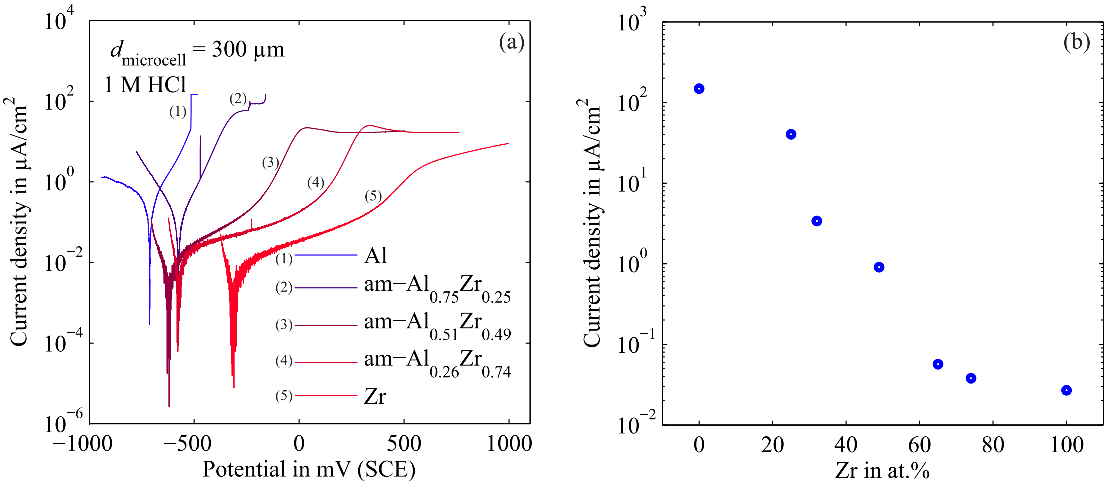

Figure 5.8: (a) Potentiodynamic polarization curves of the sputter-deposited pure, crystalline Al, the am-$Al_{1-x}Zr_x$ alloys (x = 0.25, 0.49, 0.74) and the sputter-deposited pure, crystalline Zr layer, as measured by the micro-electrochemical technique (in a 1 M HCl electrolyte solution). **(b)** The measured current density (mean value as calculated from all recorded potentiodynamic polarization curves) of the am-$Al_{1-x}Zr_x$ alloys at +200 mV above the open circuit potential (OCP) as function of the Zr content.

The improved corrosion resistance of the am-$Al_{1-x}Zr_x$ alloys with increasing Zr content in the parent alloy and its native oxide film suggests the formation of a, with increasing Zr alloying content, more and more ‘passive’ amorphous (Al,Zr)-(oxyhydr-)oxide film by anodization in 1 M HCl. The native oxide layers on the am-$Al_{1-x}Zr_x$ alloys contain an increasing amount of Zr cations with increasing Zr alloying content (see Section 5.3.1.1 and Figure 5.4). It is therefore very likely that the composition of the ‘passive’ amorphous (Al,Zr)-(oxyhydr-)oxide films formed upon anodization in 1 M HCl also exhibit a Zr content increasing with increasing Zr content of the substrate.

Indeed, as indicated by XPS analysis in this study, the Al^{ox}/Zr^{ox} ratio in the passive (Zr,Al)-(oxyhydr-)oxide layer formed on the as-deposited Zr-rich am-$Al_{1-x}Zr_x$ alloys during anodization in 1 M HCl is similar to the Al/Zr ratio of the respective parent alloy substrate (in accordance with Ref. [14]). For example, for the as-deposited am-$Al_{0.51}Zr_{0.49}$ alloy, the native oxide film has an overall Al^{ox}/Zr^{ox} ratio of 1.34 (Figure 5.4), which decreased to an Al^{ox}/Zr^{ox} ratio of 0.97 after anodization to 500 mV (i.e. for the as-deposited am-$Al_{0.51}Zr_{0.49}$ alloy, the Zr content in the passive film formed by anodization is even increased with respect to its native oxide film).

Improved corrosion resistance of am-$Al_{1-x}Zr_x$ alloys with increasing Zr content in both the alloy and its passive film (as formed by anodization) is in accordance with Ref. [14], where *macro-electrochemical* measurements of sputter-deposited Al-Zr alloys, pure, crystalline Al and pure, crystalline Zr in 1 M HCl showed a decrease of the passive current density with increasing Zr alloying content [14]. Additionally, very likely due to the macro-electrochemical measurement set-up, the occurrence of pitting corrosion above a certain critical pitting potential was observed for the sputter-deposited Al-Zr alloys and pure, crystalline Al and Zr after exceeding a critical potential [14]. This finding strongly contrasts with the results of the present corrosion study of sputter-deposited am-$Al_{1-x}Zr_x$ alloys by the *micro-electrochemical* technique which only reveals systematic pitting corrosion for the Al-richest am-$Al_{1-x}Zr_x$ alloy ($x = 0.26$). Supposing that the matrix oxide films in the previous study [14] were of the same quality (homogeneity) as in the present work, it can be concluded that macro-scale electrochemical measurements as performed in Ref. [14] are indeed (cf. Section 5.1) much more susceptible to microstructural heterogeneities at the specimen surface, such as scratches and surface contamination, which can be avoided by the selection of appropriate locations on the surface upon applying the micro-electrochemical technique as in the present work.

5.3.2.3 Corrosion behavior of the pre-oxidized am-$Al_{1-x}Zr_x$ alloy

To study the effect of the *composition* of the thermally-grown oxide layer (without the influence of a possibly interfering oxide-layer thickness effect), the pre-oxidation conditions for the am-$Al_{1-x}Zr_x$ alloys were chosen such that comparable oxide-layer thicknesses are obtained for the different alloy compositions: e.g. 16.0 nm for the pre-oxidized am-$Al_{0.68}Zr_{0.32}$ alloy (oxidized at 400 °C for 10 h), 19.3 nm for pre-oxidized am-$Al_{0.51}Zr_{0.49}$ alloy (oxidized at 400 °C for 53 minutes) and 17.2 nm for the pre-oxidized am-$Al_{0.35}Zr_{0.65}$ alloy (oxidized at 400 °C for 32 minutes). Potentiodynamic polarization curves of such pre-oxidized am-$Al_{1-x}Zr_x$ alloys are presented in Figure 5.9. The pre-oxidized am-$Al_{1-x}Zr_x$ alloys show superior corrosion behavior as compared to the as-deposited am-$Al_{1-x}Zr_x$ alloys (compare Figure 5.8a and Figure 5.9). The passive current density on the pre-oxidized am-$Al_{1-x}Zr_x$ alloys is of the order 10^{-1} µA/cm^2 or below upon anodization up to 1000 mV. This is significantly lower than the already very low passive current density of the order 10^1 µA/cm^2 (at 500 mV vs. SCE) attained for the as-deposited Zr-rich am-$Al_{1-x}Zr_x$ alloys (see Figure 5.8a and Sec. 5.3.2.1).

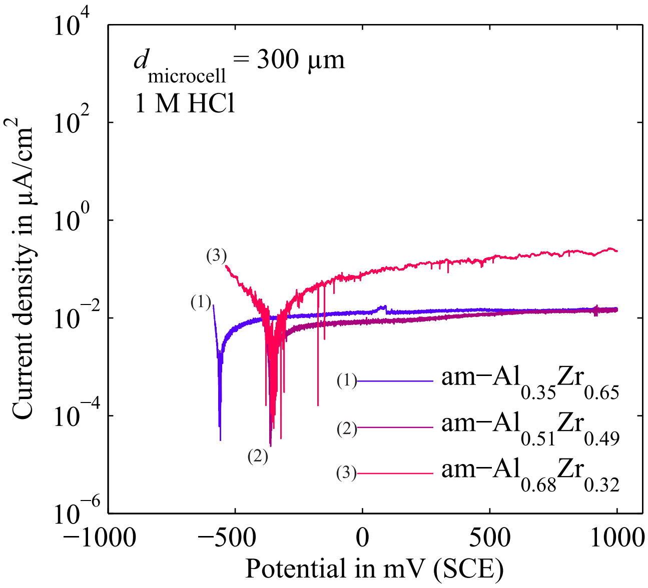

Figure 5.9: Potentiodynamic polarization curves of the pre-oxidized am-$Al_{0.35}Zr_{0.65}$ (pre-oxidized at 400 °C for 32 minutes, oxide layer thickness 17.2 nm), am-$Al_{0.51}Zr_{0.49}$ (pre-oxidized at 400 °C for 53 minutes, oxide layer thickness 19.3 nm) and am-$Al_{0.68}Zr_{0.32}$ (pre-oxidized at 400 °C for 10 h, oxide layer thickness 16.0 nm) alloys.

The potentiodynamic polarization curve of the Al-rich am-$Al_{0.68}Zr_{0.32}$ alloy reveals a higher passive current density (2×10^{-1} µA/cm^2 at 1000 mV vs. SCE) by anodization than the pre-oxidized am-$Al_{0.51}Zr_{0.49}$ and am-$Al_{0.35}Zr_{0.65}$ alloys (1.5×10^{-2} µA/cm^2 and 1.4×10^{-2} µA/cm^2 (at 1000 mV vs. SCE), respectively). Since an effect of the oxide layer thickness on the passive current density can be neglected (see above), the observed difference in the passive current density is very likely due to different compositions in the surface regions of the thermally-grown amorphous oxide layers. The pre-oxidized am-$Al_{0.51}Zr_{0.49}$ and am-$Al_{0.35}Zr_{0.65}$ alloys show an Al^{ox}/Zr^{ox} ratio of about 0.8 and 0.6, respectively, in their surficial oxide layer (depth < 3 nm) with an oxidic Al concentration of about 13-14 at.% (Figure 5.6a and b). In contrast, a twice as high concentration of oxidic Al of roughly 22 at.% with respect to the oxidic Zr content (Al^{ox}/Zr^{ox} ratio ~ 2), has been detected in the surface region (depth < 3 nm) of the amorphous oxide layer on the pre-oxidized Al-rich am-$Al_{0.68}Zr_{0.32}$ alloy (Figure 5.6c). The observed 'higher' passive current density for the pre-oxidized am-$Al_{0.68}Zr_{0.32}$ alloy is thus attributed to the relatively high oxidic Al content (in the surface region) of the 16-nm-thick thermally-grown oxide layer, in accordance with the observed dependence on Zr content of the corrosion behavior of the as-deposited am-$Al_{1-x}Zr_x$ alloys (see Section 5.3.2.2).

The effect of the amorphous *oxide-layer thickness* has been investigated by varying the oxidation time. Potentiodynamic polarization curves were recorded on the am-$Al_{0.51}Zr_{0.49}$ alloy, as pre-oxidized at 350 °C for different oxidation times (60, 150, 300, 450 and 600 minutes): see Figure 5.10a and b. The potentiodynamic polarization curve for the as-deposited am-$Al_{0.51}Zr_{0.49}$ alloy has been included in Figure 5.10a for comparison. The thickness of the am-$(Al_{0.33}Zr_{0.67})O_{1.83}$ overlayer (grown at 350 °C) and the corresponding passive current density, as observed at an applied potential in the range of 990 mV – 1000 mV, is shown as a function of the pre-oxidation time in Figure 5.10b. This indicates a higher stability of the thicker (and possibly more uniform) amorphous oxide layers, formed by thermal oxidation on am-$Al_{0.51}Zr_{0.49}$. The measured passive current density for the as-deposited am-$Al_{0.51}Zr_{0.49}$ alloy, as initially covered with a thin native oxide layer, is about 2×10^1 µA/cm^2, as taken from the plateau of the current density at about 500 mV (vs. SCE, see Figure 5.8b). Upon controlled formation of a 12.2 nm-thick amorphous oxide layer on the am-$Al_{0.51}Zr_{0.49}$ alloy by pre-oxidation at 350 °C for 60 minutes, the passive current density decreases considerably to about 3.5×10^{-2} µA/cm^2 (at 1000 mV (vs. SCE)): see Figure 5.10b. With increasing oxidation time up to 150 minutes and accompanied growth of the oxide layer thickness, a further decrease in the current density, i.e. a better corrosion resistance, is detected. However, as observed in Figure 5.10b, the passive current density (at 1000 mV (vs. SCE)) does not decrease any further for oxidation times exceeding 150 minutes, although the oxide layer still thickens. This implies that, up to a thickness of about 15 nm, the amorphous oxide-layer thickness has a distinct (indirect; see below) influence on the corrosion behavior.

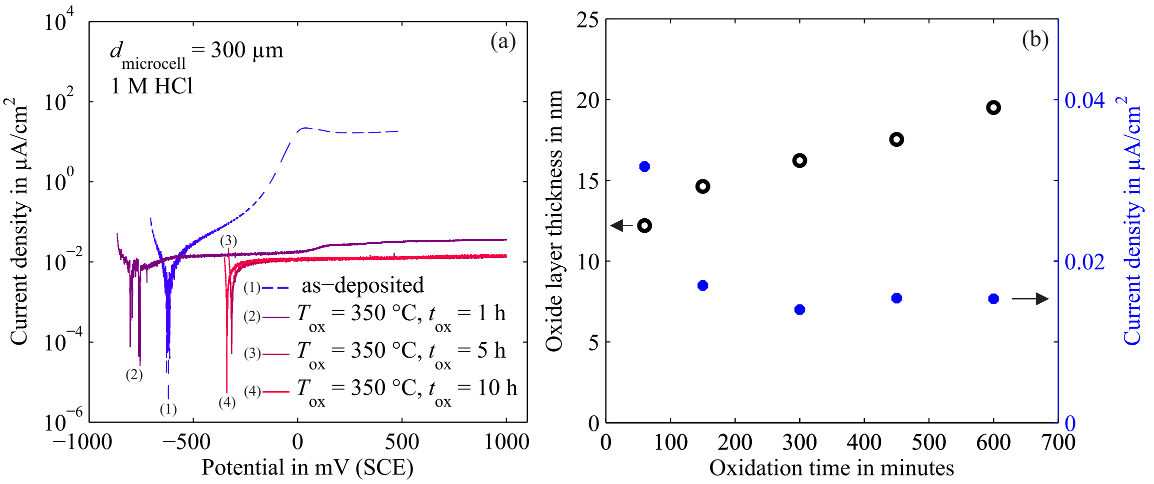

Figure 5.10: (a) Potentiodynamic polarization curves of pre-oxidized am-$Al_{0.51}Zr_{0.49}$ alloy surfaces, as prepared by pre-oxidation treatments at 350 °C for different times (i.e. 1 h, 5 h and 10 h). The potentiodynamic polarization curve for the as-deposited am-$Al_{0.51}Zr_{0.49}$ is also shown for comparison. **(b)** The thickness of the thermally-grown am-$(Al_{0.33}Zr_{0.67})O_{1.83}$ overlayer (grown at 350 °C) and the (averaged) corresponding current density, beyond OCP in the passive region at an applied potential in the range of 990 mV – 1000 mV, as function of the pre-oxidation time.

Although the thermally-grown amorphous oxide on the am-$Al_{1-x}Zr_x$ alloy is already very homogenous ‘by definition’ (e.g. no grain boundaries, no dislocations and no second phases etc.), its corrosion resistance may be increased by removing residual growth defects (e.g. compositional fluctuations, O vacancy-like defects) in the thermally-grown oxide layer by tempering at elevated temperatures [37]. This effect may explain the decrease in the passive current density with increasing oxidation/tempering time up to 150 minutes (see Figure 5.10b). For oxidation/tempering times beyond 150 minutes at 350 °C a stable density of ‘defects’ in the (surface region of the) still growing amorphous oxide layer appears to have been attained.

Finally, it is remarked that the application of supersaturated am-$M_{1-x}R_x$ alloys and metallic glasses in corrosive environments is often obstructed by their limited thermal stability [38]; long-term operation at elevated temperatures may lead to partial devitrification (inducing local compositional fluctuations and nucleation of nano-crystalline precipitates), thereby deteriorating their corrosion resistance. In this regard, it is emphasized that the thermal stability of the studied am-$Al_{1-x}Zr_x$ alloys (in air) is highest for am-$Al_{0.51}Zr_{0.49}$ (670 °C): e.g. the Al-rich am-$Al_{1-x}Zr_x$ alloys are stable up to 300 °C (for $x = 0.25$) and the Zr-rich am-$Al_{1-x}Zr_x$ alloys preserve their amorphous state up to 410 °C (for $x = 0.74$) [8]. The thermally-grown am-$(Al_{0.33}Zr_{0.67})O_{1.83}$ overlayers, on the other hand, are stable (in air) up to 500 °C [24], which could allow application of the pre-oxidized am-$Al_{1-x}Zr_x$ alloy coatings at temperatures up to 500 °C.

5.4 Conclusions

The local corrosion behavior of as-deposited and pre-oxidized am-$Al_{1-x}Zr_x$ solid-solution alloys in a 1 M HCl electrolyte solution (*p*H = 0) was investigated by the electrochemical micro-capillary technique. A very high reproducibility of the potentiodynamic polarization measurements on the as-deposited and pre-oxidized am-$Al_{1-x}Zr_x$ alloy surfaces was observed (without any signs of the onset of pitting corrosion at high applied potential), indicating that the as-deposited and thermally-oxidized am-$Al_{1-x}Zr_x$ alloy substrates are structurally and compositionally highly uniform.

For the **as-deposited** am-$Al_{1-x}Zr_x$ alloys ($x = 0.25, 0.32, 0.49, 0.65, 0.74$), as initially covered with a very thin native oxide film, the formation of a *protective* passive film in 1 M HCl requires a minimum (critical) Zr alloying content of $x = 0.49$ (based on the criterion of a passive current density $< 10^0$ µA/cm^2 at an applied potential ~ 200 mV above OCP). For $x < 0.49$, anodization in 1 M HCl rapidly results in a total break-down of the protective character of the native Al-rich oxide layer. A passive corrosion behavior, as characterized by current densities below 10^0 µA/cm^2 (at 200 mV above OCP), sets in with increasing Zr alloying content and is best for pure crystalline Zr. The passive film formed on the Zr-rich am-$Al_{1-x}Zr_x$ alloys have an Al^{ox}/Zr^{ox} ratio similar to that of the parent alloy substrate. For $x \geq 0.49$, the passive current density attains a nearly constant value of 2×10^1 µA/cm^2 at an applied potential of 500 mV, independent of the alloy composition, which is similar to that of stainless steel and sputter-deposited pure, crystalline Zr.

The **pre-oxidized** am-$Al_{1-x}Zr_x$ alloys exhibit superior corrosion behavior in 1 M HCl as compared to the as-deposited (i.e. untreated) am-$Al_{1-x}Zr_x$ alloys. The pre-oxidized am-$Al_{1-x}Zr_x$ alloys exhibit passive current densities as low as 3.5×10^{-2} µA/cm^2 upon anodization up to 1000 mV (without any signs of the onset of pitting corrosion). The passive current density becomes independent of the am-$(Al_{0.33}Zr_{0.67})O_{1.83}$ overlayer thickness for sufficiently long oxidation times of oxidation, which is ascribed to the establishment of a minimal residual growth defect structure in (the surface region of) the oxide film.

The chemical stability and excellent barrier properties of the thermally-grown am-$(Al_{0.33}Zr_{0.67})O_{1.83}$ overlayer are thus attributed to (*i*) a relatively high nominal Zr content in the surface region of the surficial oxide layer, (*ii*) chemical and structural homogeneity of the am-$(Al_{0.33}Zr_{0.67})O_{1.83}$ overlayer, as well as (*iii*) a stable, minimal residual growth defect structure (in the surface region) established by a sufficiently large time of oxidation (i.e. for times larger than 150 minutes at 350 °C).

Acknowledgements

The authors are grateful to F. Thiele and R. Völker for sputter deposition of the am-$Al_{1-x}Zr_x$ alloys, Dipl.-Ing. B. Siegle for AES measurements, M. Wieland for XPS measurements, U. Salzberger and W.-D. Lang for TEM specimen preparation, Dr. W. Sigle, Dipl.-Ing. P. Kopold and Dipl.-Ing. K. Hahn for TEM investigation (all with the Max Planck Institute for Intelligent Systems). We also thank Dr. P. Schmutz (EMPA) for useful discussions on passive film formation during anodization.

5.5 References

[1] Chen Q., Liu L., Zhang S.-M., Front. Mater. Sci. China **4** (2010) 34.

[2] Kakiuchi H., Inoue A., Onuki M., Takano Y., Yamaguchi T., Mater. Trans. **42** (2001) 678.

[3] Hashimoto K., Park P.Y., Kim J.H., Yoshioka H., Mitsui H., Akiyama E., Habazaki H., Kawashima A., Asami K., Grzesik Z., Mrowec S., Mater. Sci. Eng. A-Struct. Mater. Prop. Microstruct. Process. **198** (1995) 1.

[4] Fecht H.J., Han G., Fu Z., Johnson W.L., J. Appl. Phys. **67** (1990) 1744.

[5] Ma E., Brunner F., Atzmon M., J. Phase Equilib. **14** (1993) 137.

[6] Sheng H.W., Lu K., Ma E., J. Appl. Phys. **85** (1999) 6400.

[7] Rehn L.E., Okamoto P.R., Pearson J., Bhadra R., Grimsditch M., Phys. Rev. Lett. **59** (1987) 2987.

[8] Weller K., Zotov N., Wang Z.M., Jeurgens L.P.H., Mittemeijer E.J., J. Non-Cryst. Solids **427** (2015) 104.

[9] Hashimoto K., Kumagai N., Yoshioka H., Kim J.H., Akiyama E., Habazaki H., Mrowec S., Kawashima A., Asami K., Corros. Sci. **35** (1993) 363.

[10] Yoshioka H., Yan Q., Habazaki H., Kawashima A., Asami K., Hashimoto K., Corros. Sci. **31** (1990) 349.

[11] Vargel C. Corrosion of aluminium. Amsterdam: Elsevier, 2004.

[12] Davis J.R., editor Corrosion of aluminum and aluminum alloys. Materials Park, OH: ASM International, 1999.

[13] Lucente A.M., Scully J.R., J. Electrochem. Soc. **155** (2008) C234.

[14] Yoshioka H., Habazaki H., Kawashima A., Asami K., Hashimoto K., Corros. Sci. **33** (1992) 425.

[15] Yoshioka H., Habazaki H., Kawashima A., Asami K., Hashimoto K., Electrochim. Acta **36** (1991) 1227.

[16] Hashimoto K., Habazaki H., Akiyama E., Yoshioka H., Kim J.H., Park P.Y., Kawashima A., Asami K., Science reports of the Research Institutes, Tohoku University. Ser. A, Physics, chemistry and metallurgy **42** (1996) 99.

[17] McCafferty E., Corros. Sci. **42** (2000) 1993.

[18] McCafferty E., Corros. Sci. **44** (2002) 1393.

[19] Ott N., Beni A., Ulrich A., Ludwig C., Schmutz P., Talanta **120** (2014) 230.

[20] Beni A., Ott N., Pawelkiewicz M., Warde M., Young K., Bauer B., Rajput P., Detlefs B., Zegenhagen J., McGrath R., Barthes-Labrousse M.-G., Jeurgens L.P.H., Schmutz P., Electrochemistry Communications **46** (2014) 13.

[21] Bohni H., Suter T., Schreyer A., Electrochim. Acta **40** (1995) 1361.

[22] Suter T., Bohni H., Electrochim. Acta **42** (1997) 3275.

[23] Suter T., Bohni H., Electrochim. Acta **47** (2001) 191.

[24] Weller K., Jeurgens L.P.H., Wang Z.M., Mittemeijer E.J., Acta Mater. **87** (2015) 187.

[25] Weller K., Wang Z., Jeurgens L.P.H., Mittemeijer E.J., Acta Mater. **94** (2015) 134.

[26] McCafferty E., J. Electrochem. Soc. **151** (2004) B82.

[27] Mittemeijer E.J., Welzel U. Modern diffraction methods. Weinheim: Wiley-VCH, 2013 (Chapter 12).

[28] Zähr J., Oswald S., Türpe M., Ullrich H.J., Füssel U., Vacuum **86** (2012) 1216.

[29] Weller K., Wang Z., Jeurgens L.P.H., Mittemeijer E.J., Acta Mater., in press.

[30] Suter T. Mikroelektrochemische Untersuchungen bei austenitischen 'rostfreien' Stählen. vol. Ph. D: ETH Zürich, 1997.

[31] Marcus P. Corrosion mechanisms in theory and practice: CRC Press, 2011.

[32] DeRose J., Suter T., Bałkowiec A., Michalski J., Kurzydlowski K., Schmutz P., Corros. Sci. **55** (2012) 313.

[33] Brett C.M.A., Corros. Sci. **33** (1992) 203.

[34] Beck T.R., Electrochim. Acta **33** (1988) 1321.

[35] Szklarska-Smialowska Z., Corros. Sci. **41** (1999) 1743.

[36] Reichel F., Jeurgens L.P.H., Mittemeijer E.J., Acta Mater. **56** (2008) 2897.

[37] Luborsky F. Amorphous metallic alloys: Butterworth and Co (Publishers): London, UK, 1983.

[38] Liu B., Liu L., Materials Science and Engineering: A **415** (2006) 286.

Chapter 6

Summary

Many properties of a material are directly related to the surficial oxide film, which inevitably forms in contact with an oxidizing gaseous or liquid environment. Hence the material properties can be controlled by tailoring the oxidation conditions (temperature, time, oxygen pressure), which requires fundamental understanding of the oxidation process. The oxidation behavior, and specifically the microstructural evolution of the growing oxide film, can be influenced directly by alloying. However, *crystalline* metallic alloys usually can only form solid solutions in (sometimes very) narrow composition ranges and thus the possibilities to tailor the oxidation behavior and thereby the oxide properties by selective variation of *only* the alloy composition (i.e. without subsequent variation of the alloy microstructure) are generally severely limited for crystalline alloys. *Amorphous* alloys (or metallic glasses), on the other hand, can be prepared as (supersaturated) solid solutions over very wide composition ranges for many alloy systems. Until now, the oxidation behavior of amorphous metallic materials has received much less attention than the oxidation behavior of crystalline materials and, consequently, a thorough understanding of the oxidation mechanisms of amorphous alloys is lacking.

The present thesis presents a comprehensive investigation of the thermal oxidation of amorphous Al_xZr_{1-x} (am-Al_xZr_{1-x}) alloys ($0.26 \leq x \leq 0.68$). The oxide composition and microstructure, as well as the oxidation kinetics and oxidation mechanism of am-Al_xZr_{1-x} alloys upon thermal oxidation at relatively low oxidation temperatures of 350 – 400 °C (see Chapter 2 and 3, respectively) and at high oxidation temperatures of 500 – 560 °C (see Chapter 4) have been investigated. To this end, 2-μm thick am-Al_xZr_{1-x} coatings ($0.26 \leq x \leq 0.68$), as prepared by magnetron-cosputtering on 50 nm SiO_2/50 nm Si_3N_4/Si wafers, were oxidized in a temperature range of T = 350 °C – 560 °C at $p_{O2} = 10^5$ Pa for up to 10 h. The phase and microstructural development upon oxidation of am-Al_xZr_{1-x} alloys, as well as the oxidation-induced changes in the alloy substrate, were investigated by a combinatorial experimental approach using X-ray diffraction (XRD), cross-sectional (analytical) transmission electron microscopy (TEM), Auger electron spectroscopy (AES) sputter-depth profiling and spectroscopic ellipsometry (SE).

Finally, the corrosion behavior of as-deposited and oxidation-treated am-Al_xZr_{1-x} alloys have been investigated as function of the alloy composition and oxidation conditions (Chapter 5).

An amorphous (Al,Zr)-oxide layer of homogenous composition and uniform thickness develops on the am-Al_xZr_{1-x} alloys during oxidation of am-Al_xZr_{1-x} alloys ($0.26 \leq x \leq 0.68$) at 350 °C – 400 °C (**Chapter 2**). The occurrence of an amorphous state (rather than a bulk-preferred crystalline state) could be attributed to the relatively high nucleation barriers for the crystalline oxide phases(s), as arising from interface energetics, kinetic obstructions of diffusional transport and structural rearrangements in the oxidizing alloy as required for the development of crystalline compounds (as ZrO_2 and Al_2O_3). Surprisingly, the grown amorphous (Al,Zr)-oxide layers have a single homogenous composition $(Al_{0.33}Zr_{0.67})O_{1.83}$, independent of the parent alloy composition and the applied oxidation temperature (see Figure 6.1a). The practically singular composition of the amorphous oxide phase, $(Al_{0.33}Zr_{0.67})O_{1.83}$, can be explained on a fully thermodynamic basis: Conceiving the amorphous ternary oxide phase as a liquid oxide-oxide solution phase, which is supercooled to low (oxidation) temperatures, the equilibrium of the amorphous solid solution phase and the amorphous oxide phase is realized for a wide range of composition of the solid solution and amorphous oxide phase, $(Al_{0.33}Zr_{0.67})O_{1.83}$, with practically constant composition of the oxide phase as a consequence of the deep minimum of the Gibbs energy of formation for the am-(Al,Zr)-oxide phase, $\Delta G^{\text{am-(Al,Zr)-oxide}}$, occurring at a composition of $(AlO_{1.5})_{0.33}(ZrO_2)_{0.67}$. A three-dimensional representation of the Gibbs energy surfaces $\Delta G^{\text{am-AlZr[O]}}$ and $\Delta G^{\text{am-(Al,Zr)-oxide}}$, for the concurring amorphous Al-Zr alloy phase and amorphous oxide phase, respectively, has been constructed schematically; see Figure 6.1b. Thus the role of thermodynamics in controlling the developing oxide phase composition, even for the growth of *amorphous* oxides occurring under conditions (far) away from genuine thermodynamic equilibrium for bulk phases has been evidenced.

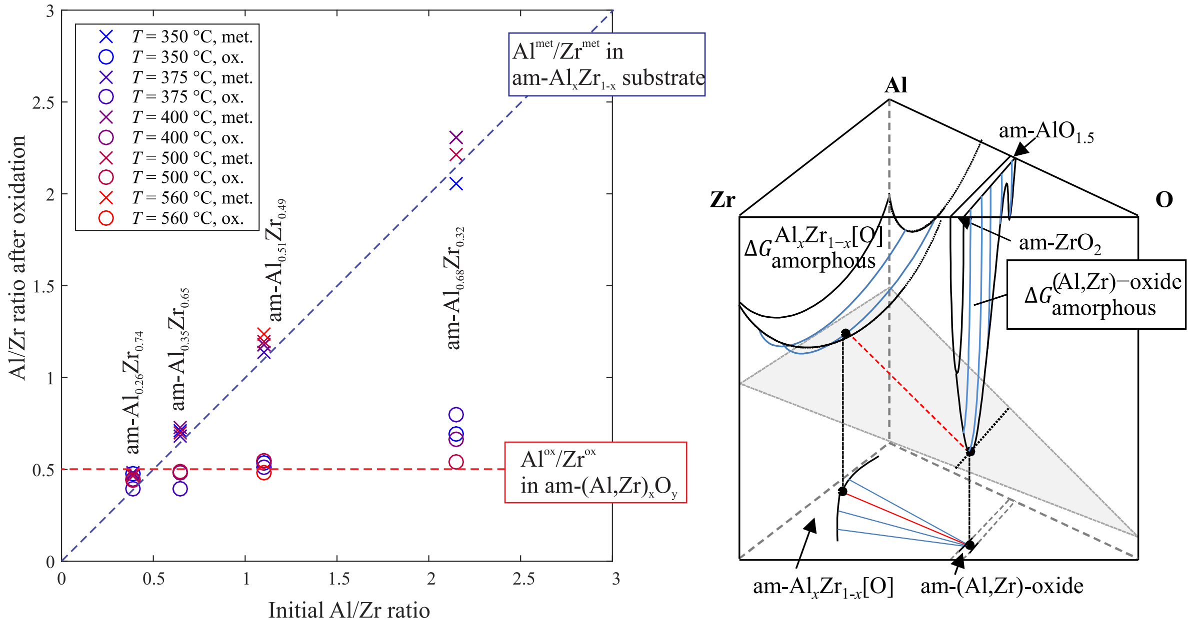

a) **b)**

Figure 6.1: **a)** The Al^{ox}/Zr^{ox} ratio in the grown amorphous oxide (unfilled circles) and the Al^{met}/Zr^{met} ratio in the original am-Al_xZr_{1-x} substrate (crosses) upon thermal oxidation of am-Al_xZr_{1-x} alloys of different (initial) compositions at the temperatures indicated. **b)** Schematic ternary phase diagram of Al, Zr and O pertaining to a temperature in the range of 350 °C – 400 °C.

The oxidation kinetics of the am-Al_xZr_{1-x} alloys ($0.26 \leq x \leq 0.68$) (**Chapter 3**), as determined by SE, were found to accelerate pronouncedly with increasing Zr content in the am-Al_xZr_{1-x} alloy, which is due to (*i*) the increase of the solubility of O in the alloy with increasing Zr content and (*ii*) the increase of the mobility of Al in the (O-dissolved region of the) am-Al_xZr_{1-x} alloy with increasing Zr content. Parabolic oxide-film growth kinetics occurs for Al-rich am-Al_xZr_{1-x} alloys ($x \geq 0.51$) (cf. Figure 6.2), whereas linear oxide-film growth kinetics prevails for Zr-rich am-Al_xZr_{1-x} alloys ($x < 0.35$). The am-$Al_{0.35}Zr_{0.65}$ alloy takes an intermediate position. The parabolic oxide-film growth kinetics of the am-$Al_{0.51}Zr_{0.49}$ (Al/Zr ratio = 1.0) and am-$Al_{0.68}Zr_{0.32}$ (Al/Zr ratio = 2.1) alloy substrates (with an Al/Zr ratio much higher than the thermodynamically-preferred Al^{ox}/Zr^{ox} ratio of 0.5) implies a diffusion-controlled oxide-growth behavior. The oxide-film growth rate can be governed by the rate of oxygen diffusion through the growing oxide layer and/or by the backward diffusion of Al from the reacting oxide/alloy interface towards the interior of the alloy (as a consequence of the exclusive formation of the thermodynamically-preferred am-$(AlO_{1.5})_{0.33}(ZrO_2)_{0.67}$ phase). For high Zr contents of the am-Al_xZr_{1-x} alloy, the diffusion processes in oxide film and substrate have become that fast that the oxide-film growth rate is governed by the reactive formation of the thermodynamically preferred am-$(AlO_{1.5})_{0.33}(ZrO_2)_{0.67}$ oxide phase at the oxide layer/substrate interface: linear oxide-film growth kinetics occurs.

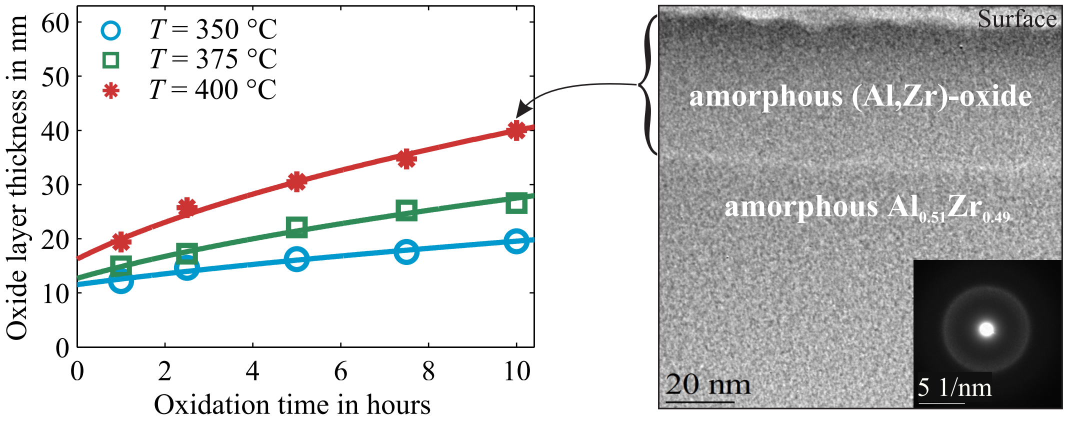

(a) (b)

Figure 6.2: (a) Oxide-film thickness of am-$Al_{0.51}Zr_{0.49}$ as function of the oxidation time in a temperature range of 350 °C to 400 °C. **(b)** Cross-sectional bright-field TEM image of am-$Al_{0.51}Zr_{0.49}$ oxidized at 400 °C for 10 h.

Upon prolonged oxidation of amorphous $Al_{0.44}Zr_{0.56}$ alloys at 500 °C and 560 °C at p_{O2} = 1×10^5 Pa, a three-stage oxidation mechanism is disclosed (**Chapter 4**). During early stages of oxidation of amorphous $Al_{0.44}Zr_{0.56}$ alloys upon exposure to pure O_2(g) at 500 °C (up to 5 h) and 560 °C (up to 45 minutes) the formation of an amorphous (Zr,Al)-oxide layer of homogeneous composition and uniform thickness has been observed, while the underlying alloy preserves its amorphous state (Stage I). The amorphous (Zr,Al)-oxide layers are enriched in Zr with respect to the alloy substrate and have the same composition, practically independent of the oxidation time and temperature, which complies with a distinct (local) minimum in the Gibbs energy of mixing for the liquid oxide-oxide solution phase (cf. Chapter 2). An Al-enrichment in the alloy adjacent to the alloy/am-(Zr,Al)-oxide interface occurs upon oxidation at T = 560 °C for oxidation times up to 45 minutes, as induced by the preferential oxidation of Zr from the am-$Al_{0.44}Zr_{0.56}$ alloy. A concurrent expulsion of O from the region of Al enrichment to larger depths occurs as a consequence of a decreased O solubility in the Al-enriched solid solution.

Upon prolonged oxidation of amorphous $Al_{0.44}Zr_{0.56}$ alloys at 560 °C ($t \geq 45$ minutes), a crystalline tetragonal ZrO_2 (t-ZrO_2) phase nucleates, while the alloy remains amorphous (Stage II). The nucleation and growth of t-ZrO_2 at 560 °C occurs exclusively close to the interface between the initially formed amorphous (Zr,Al)-oxide layer and the alloy, immediately underneath the region of Al enrichment in the substrate, triggered by oxidation-induced compositional changes in the alloy below the reacting alloy/oxide interface and a favorable energy of the interface between t-ZrO_2 crystallites and the amorphous alloy matrix.

Growth of the t-ZrO_2 crystallites (by selective incorporation of O and Zr from the supersaturated solid solution) is associated with the expulsion (segregation) of Al into the region surrounding the growing t-ZrO_2 particles (Stage III). As a result, the growing t-ZrO_2 crystallites become embedded in an Al-enriched matrix, poor in Zr and O, which impedes their further growth. Protrusions from the surface of the t-ZrO_2 crystallites preferentially grow towards oxygen-richer regions in the matrix and, consequently, the growth front becomes unstable and a dendrite morphology develops, governed by local fluctuations in the dissolved O concentration. The growing t-ZrO_2 oxide crystallites eventually laterally coalesce to form a continuous layer constituted of branches of dendrite-shaped t-ZrO_2 phase crystallites surrounded by an Al-rich amorphous Al-Zr alloy matrix, beneath the amorphous (Al,Zr)-oxide layer (Figure 6.3).

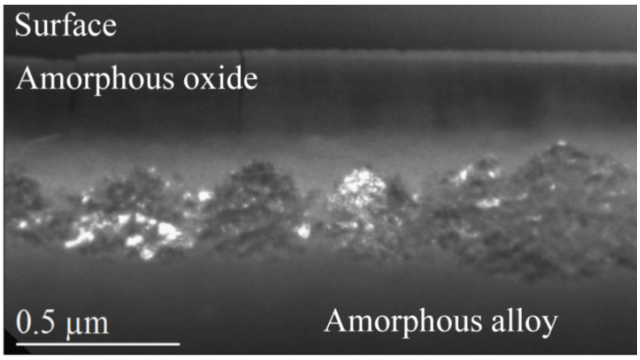

Figure 6.3: Dark-field TEM image of a cross-section of the am-$Al_{0.44}Zr_{0.56}$ specimen oxidized at 560 °C ($p_{O2} = 1\times10^5$ Pa) for 180 minutes.

Investigations of the corrosion resistance of untreated and pre-oxidized am-$Al_{1-x}Zr_x$ alloys (x = 0.25, 0.32, 0.49, 0.65, 0.74) by the electrochemical micro-capillary technique evidence an excellent corrosion resistance of the pre-oxidized am-$Al_{1-x}Zr_x$ alloys (**Chapter 5**). For the as-deposited am-$Al_{1-x}Zr_x$ alloys, as initially covered with a very thin native oxide film, the formation of a *protective* passive film in 1 M HCl requires a minimum (critical) Zr alloying content of $x = 0.49$. For $x < 0.49$, anodization in 1 M HCl rapidly results in a total break-down of the protective character of the native Al-rich oxide layer. A passive corrosion behavior, as characterized by current densities below 10^0 µA/cm^2 (at 200 mV above the open circuit potential (OCP)), sets in with increasing Zr alloying content and is best for pure crystalline Zr. The passive film formed on the Zr-rich am-$Al_{1-x}Zr_x$ alloys have an Al^{ox}/Zr^{ox} ratio similar to that of the parent alloy substrate. For $x \geq 0.49$, the passive current density attains a nearly constant value of 2×10^1 µA/cm^2 at an applied potential of 500 mV, independent of the alloy composition, which is similar to that of stainless steel and sputter-deposited pure, crystalline Zr.

The pre-oxidized am-$Al_{1-x}Zr_x$ alloys exhibit superior corrosion behavior in 1 M HCl as compared to the as-deposited (i.e. untreated) am-$Al_{1-x}Zr_x$ alloys (see Figure 6.4a). The pre-oxidized am-$Al_{1-x}Zr_x$ alloys exhibit passive current densities as low as 3.5×10^{-2} µA/cm^2 upon anodization up to 1000 mV (without any signs of the onset of pitting corrosion). The passive current density becomes independent of the am-$(Al_{0.33}Zr_{0.67})O_{1.83}$ overlayer thickness for sufficiently long times of oxidation, which is ascribed to the establishment of a minimal residual growth defect structure in (the surface region of) the oxide film (see Figure 6.4b).

The chemical stability and excellent barrier properties of the thermally-grown am-$(Al_{0.33}Zr_{0.67})O_{1.83}$ overlayer are thus attributed to (*i*) a relatively high nominal Zr content in the surface region of the surficial oxide layer, (*ii*) chemical and structural homogeneity of the am-$(Al_{0.33}Zr_{0.67})O_{1.83}$ overlayer, as well as (*iii*) a stable, minimal residual growth defect structure (in the surface region) established by a sufficiently large time of oxidation (i.e. for times larger than 150 minutes at 350 °C). Controlled pre-oxidation treatments of sputter-deposited amorphous Al_xZr_{1-x} coatings may thus offer a promising route for the development of a new generation of corrosion-resistant amorphous-alloy-based coating systems.

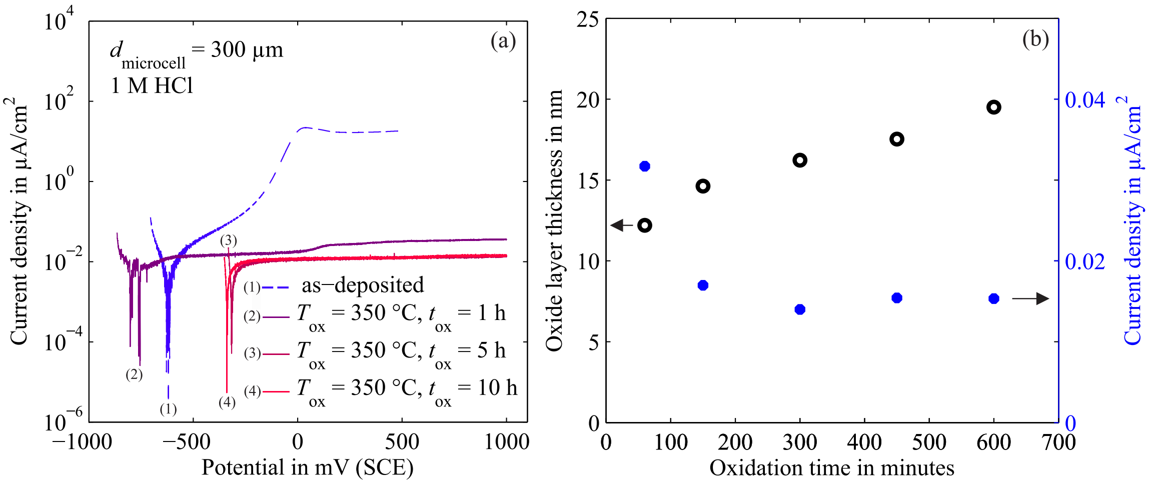

Figure 6.4: (a) Potentiodynamic polarization curves of pre-oxidized am-$Al_{0.51}Zr_{0.49}$ alloy surfaces, as prepared by pre-oxidation treatments at 350 °C for different times (i.e. 1 h, 5 h and 10 h). The potentiodynamic polarization curve for the as-deposited am-$Al_{0.51}Zr_{0.49}$ is also shown for comparison. **(b)** The thickness of the thermally-grown am-$(Al_{0.33}Zr_{0.67})O_{1.83}$ overlayer (grown at 350 °C) and the (averaged) corresponding current density, beyond OCP in the passive region at an applied potential in the range of 990 mV – 1000 mV, as function of the pre-oxidation time.

Chapter 7

Zusammenfassung

Viele Eigenschaften eines Materials werden direkt von der Oxidschicht, welche sich unvermeidlich bei Kontakt mit einer oxidierenden gasförmigen oder flüssigen Umgebung an der Oberfläche bildet, beeinflusst. Folglich können diese Materialeigenschaften durch kontrollierte Oxidationsbedingungen (Temperatur, Zeit, Sauerstoffdruck) gesteuert werden. Dies erfordert jedoch ein grundlegendes Verständnis der ablaufenden Oxidationsprozesse. Das Oxidationsverhalten und insbesondere die Entwicklung der Mikrostruktur des wachsenden Oxidfilms können direkt durch Legieren beeinflusst werden. Allerdings ist für *kristalline* metallische Legierungen die Bildung von Festkörperlösungen in der Regel auf (manchmal sehr) enge Zusammensetzungsbereiche begrenzt; somit ist die Möglichkeit das Oxidationsverhalten und dadurch auch die Materialeigenschaften lediglich durch eine Variation der Legierungszusammensetzung (das heißt ohne eine einhergehende Variation der Mikrostruktur der Legierung) für kristalline Legierungen zu beeinflussen stark eingeschränkt. *Amorphe* Legierungen oder metallische Gläser können für viele Legierungssysteme in sehr weiten Zusammensetzungsbereichen gebildet werden. Bislang wurde dem Oxidationsverhalten von amorphen Metallen im Vergleich zu dem Oxidationsverhalten von kristallinen Metallen wenig Aufmerksamkeit gewidmet. Folglich fehlt ein grundlegendes Verständnis des Oxidationsmechanismus von amorphen Legierungen.

Die vorliegende Doktorarbeit stellt eine umfassende Untersuchung der thermischen Oxidation von amorphen Al_xZr_{1-x} (am-Al_xZr_{1-x}) Legierungen ($0.26 \leq x \leq 0.68$) dar. Es wurden Zusammensetzung und Mikrostruktur der auftretenden Oxidphase(n), sowie Oxidationskinetik und Oxidationsmechanismus von am-Al_xZr_{1-x} Legierungen, bei relativ niedrigen Oxidationstemperaturen von 350 – 400 °C (siehe Kapitel 2 bzw. 3) und bei hohen Oxidationstemperaturen von 500 – 560 °C (siehe Kapitel 4), untersucht. Zu diesem Zweck wurden 2 μm dicke am-Al_xZr_{1-x} Schichten ($0.26 \leq x \leq 0.68$), welche mittels Magnetron-Sputtern auf 50 nm SiO_2/50 nm Si_3N_4/Si Wafer hergestellt wurden, in einem Temperaturbereich von 350 °C bis 560 °C und unter einem Druck von $p_{O2} = 10^5$ Pa für bis zu 10 Stunden oxidiert. Die Phasen- und

Gefügeentwicklung von oxidierten am-Al_xZr_{1-x} Legierungen, sowie die oxidationsinduzierten Veränderungen in der Legierung, wurden mittels Kombination von Röntgenbeugung (XRD), analytischer Transmissionselektronenmikroskopie (TEM) an Querschnittsproben, Augerelektronenspektroskopie (AES) zur Erstellung von Konzentrationstiefenprofilen und spektroskopischer Ellipsometrie (SE) untersucht. Abschließend wurde das Korrosionsverhalten von am-Al_xZr_{1-x} Legierungen direkt nach der Herstellung sowie nach Oxidation als Funktion der Legierungszusammensetzung und der Oxidationsbedingungen untersucht (Kapitel 5).

Bei der Oxidation von am-Al_xZr_{1-x} Legierungen ($0.26 \leq x \leq 0.68$) bei 350 °C – 400 °C **(Kapitel 2)** entwickelt sich eine amorphe (Al,Zr)-Oxidschicht mit homogener Zusammensetzung und gleichmäßiger Dicke auf den am-Al_xZr_{1-x} Legierungen. Das Auftreten einer amorphen Phase (anstelle der thermodynamisch-bevorzugten kristallinen Phase) lässt sich durch eine relativ hohe Keimbildungsbarriere für die kristallinen Oxidphase(n) erklären, welche auf die Energieerhöhung bei Ausbildung von Grenzflächen, auf die Behinderung von Diffusionstransporten und von strukturellen Änderungen, nötig zur Bildung kristalliner Oxidverbindungen (ZrO_2 and Al_2O_3), zurückgeführt wird. Überraschenderweise zeigen die entstandenen amorphen (Al,Zr)-Oxidschichten eine einheitliche homogene Zusammensetzung $(Al_{0.33}Zr_{0.67})O_{1.83}$, unabhängig von der Zusammensetzung des Ausgangsmaterials und der Oxidationstemperatur (siehe Abbildung 7.1a). Die praktisch einheitliche Zusammensetzung der unterschiedlichen amorphen Oxidschichten, $(Al_{0.33}Zr_{0.67})O_{1.83}$, kann auf Grundlage der Thermodynamik des Systems erklärt werden: Die amorphe ternäre Oxidphase lässt sich mit einer flüssigen Oxid-Oxid-Lösungsphase beschreiben, welche sich bei den niedrigen (Oxidations-)Temperaturen in einem unterkühlten Zustand befindet. Bei Bildung dieser Oxidphase während der Oxidation der amorphen Legierung stellt sich über einen weiten Zusammensetzungsbereich der amorphen Legierung ein thermodynamisches Gleichgewicht zwischen der amorphen Festkörperlösung und der amorphen Oxidphase ein, bei welchem letztere eine praktisch konstante Zusammensetzung aufweist als Konsequenz eines tiefen Minimums der Gibbs-Energie der amorphen (Al,Zr)-Oxid-Phase, $\Delta G^{\text{am-(Al,Zr)-oxide}}$, bei einer Zusammensetzung von $(AlO_{1.5})_{0.33}(ZrO_2)_{0.67}$. Dieser Sachverhalt wurde mittels schematischer dreidimensionaler Gibbs-Energie-Flächen für die amorphe Festkörperlösung $\Delta G^{\text{am-AlZr[O]}}$ und die amorphe (Al,Zr)-Oxidphase $\Delta G^{\text{am-(Al,Zr)-oxide}}$ veranschaulicht (Abbildung 7.1b). Dadurch konnte der Einfluss der Thermodynamik auf die Zusammensetzung der sich entwickelten Oxidphase aufgezeigt werden, auch für das Wachstum einer metastabilen, *amorphen* Oxidphase unter Bedingungen weit entfernt vom eigentlichen thermodynamischen Gleichgewicht des Systems.

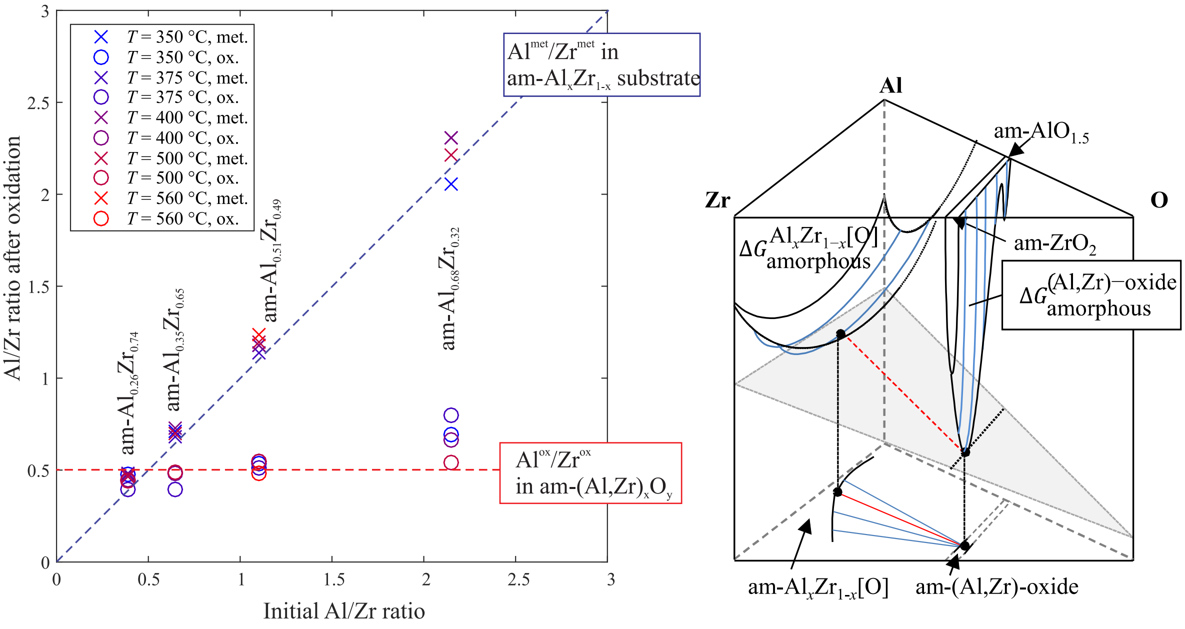

a) **b)**

Abbildung 7.1: **a)** Das Al^{ox}/Zr^{ox}-Verhältnis in der entstandenen amorphen Oxidphase (Kreise) und das Al^{met}/Zr^{met}-Verhältnis in der ursprünglichen am-Al_xZr_{1-x}-Legierung (Kreuze) nach der thermischen Oxidation von am-Al_xZr_{1-x} Legierungen verschiedenster (Ausgangs-)Zusammensetzungen bei den jeweils angegebenen Oxidationstemperaturen. **b)** Schematisches ternäres Phasendiagramm von Al, Zr und O im Temperaturbereich von 350 – 400 °C.

Die mittels spektroskopischer Ellipsometrie bestimmte Oxidationskinetik von am-Al_xZr_{1-x}-Legierungen ($0.26 \leq x \leq 0.68$) **(Kapitel 3)** zeigt eine Beschleunigung mit steigendem Zr-Gehalt in der am-Al_xZr_{1-x} Legierung. Dies wird (i) einer Zunahme der Löslichkeit von O mit steigendem Zr-Gehalt in der Legierung und (ii) einer Zunahme der Mobilität von Al mit steigendem Zr-Gehalt in der (sauerstoffangereicherten) am-Al_xZr_{1-x} Legierung zugeschrieben. Die Wachstumskinetik der Oxidschichten für die Oxidation von Al-reichen am-Al_xZr_{1-x} Legierungen ($x \geq 0.51$) folgt einem parabolischen Wachstumsgesetz (siehe Abbildung 7.2), wohingegen bei der Oxidation von Zr-reichen am-Al_xZr_{1-x}-Legierungen ($x < 0.35$) ein lineares Wachstumsgesetz der Oxidschichten auftritt. Die am-$Al_{0.35}Zr_{0.65}$-Legierung nimmt dabei eine Zwischenposition ein. Das parabolische Wachstum der Oxidschichten der am-$Al_{0.51}Zr_{0.49}$ (Al/Zr-Verhältnis = 1.0) und am-$Al_{0.68}Zr_{0.32}$ (Al/Zr-Verhältnis = 2.1) Legierungen (welche somit ein Al/Zr-Verhältnis größer als das thermodynamisch bevorzugte Al^{ox}/Zr^{ox} Verhältnis von 0.5 der amorphen Oxidphase aufweisen) deutet auf ein diffusionskontrolliertes Wachstumsverhalten der Oxidschichten hin. Die Wachstumskinetik der Oxidschicht kann einerseits durch den Sauerstofftransport durch die wachsende Oxidschicht hindurch und/oder andererseits durch die Diffusion von Al von der Reaktionsgrenzfläche Oxid/Legierung in tieferliegende Bereiche der Legierung hinein (bedingt durch die Bildung der thermodynamisch bevorzugten Oxidphase am-$(AlO_{1.5})_{0.33}(ZrO_2)_{0.67}$) bestimmt werden. Bei höherem Zr-Gehalt in der am-Al_xZr_{1-x} Legierung sind die Diffusionsprozesse in der Oxidschicht und in der Legierung so schnell, dass die Wachstumskinetik der Oxidschicht durch die Bildungsrate der thermodynamisch-bevorzugten am-$(AlO_{1.5})_{0.33}(ZrO_2)_{0.67}$-Phase an der Oxid/Legierung-Grenzfläche bestimmt wird. Dies hat eine lineare Wachstumskinetik der Oxidschicht zufolge.

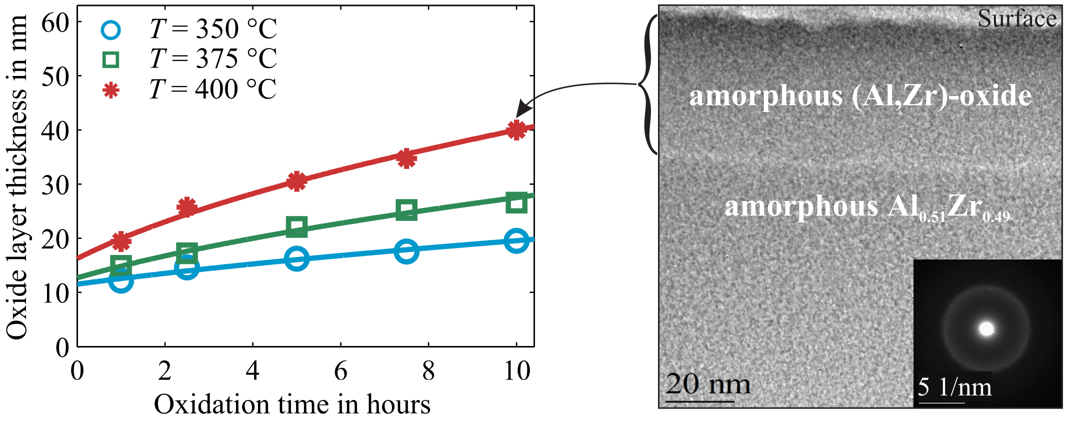

(a) (b)

Abbildung 7.2: (a) Oxidschichtdicke der am-$Al_{0.51}Zr_{0.49}$ Legierung als Funktion der Oxidationszeit in einem Temperaturbereich von 350 – 400 °C. **(b)** Hellfeld-TEM-Bild einer Querschnittsprobe einer am-$Al_{0.51}Zr_{0.49}$ Legierung, welche bei 400 °C für 10 h oxidiert wurde.

Das Oxidationsverhalten von amorphen $Al_{0.44}Zr_{0.56}$ Legierungen bei 500 – 560 °C und $p_{O2} = 1\times10^5$ Pa zeigt einen dreistufigen Oxidationsmechanismus **(Kapitel 4)**. Während des Anfangsstadiums der Oxidation von amorphen $Al_{0.44}Zr_{0.56}$ Legierungen bei 500 °C (bis zu 5 Stunden) und bei 560 °C (bis zu 45 Minuten) wurde zunächst die Bildung einer amorphen (Al,Zr)-Oxidschicht beobachtet (Stufe I), welche eine homogene Zusammensetzung und eine gleichmäßige Dicke aufweist. Währenddessen behält die darunterliegende Legierung ihren amorphen Zustand bei. Die amorphen (Al,Zr)-Oxidschichten sind im Vergleich zu der Ausgangslegierungszusammensetzung mit Zr angereichert und haben dieselbe Zusammensetzung unabhängig von Oxidationszeit und –temperatur. Dies spricht für ein stark ausgeprägtes lokales Minimum der Gibbs-Energie der Oxid-Oxid-Lösungsphase (siehe Kapitel 2). Während der Oxidation der am-$Al_{0.44}Zr_{0.56}$ Legierung bei 560 °C bis zu 45 Minuten wird durch die bevorzugte Oxidation von Zr eine Al-Anreicherung in der Legierung direkt unter der Grenzfläche Oxid/Legierung beobachtet. Gleichzeitig tritt eine Verdrängung von O aus dem Bereich der Al-Anreicherung in tieferliegende Bereiche der Legierung auf, ausgelöst durch eine herabgesetzte Sauerstofflöslichkeit in der Al-angereicherten Festkörperlösung.

Bei längeren Oxidationszeiten der amorphen $Al_{0.44}Zr_{0.56}$ Legierung bei 560 °C ($t \geq$ 45 Minuten) bildet sich eine kristalline tetragonale ZrO_2 Phase (t-ZrO_2), wohingegen die amorphe Legierung ihre amorphe Struktur weiterhin beibehält (Stufe II). Keimbildung und Wachstum der t-ZrO_2 Phase bei 560 °C findet ausschließlich nahe der Grenzfläche zwischen der bereits entstandenen amorpher (Zr,Al)-Oxidschicht und der amorphen Legierung, unmittelbar unter dem Bereich der Al-Anreicherung in der amorphen Legierung statt. Die t-ZrO_2 Phase entsteht aufgrund der oxidationsinduzierten Zusammensetzungsveränderung in der Legierung direkt unterhalb der Grenzfläche und einer günstigen Grenzflächenenergie zwischen t-ZrO_2 Kristallit und amorpher Legierungsmatrix.

Das Wachstum der t-ZrO_2 Kristallite (durch selektiven Einbau von O und Zr aus der übersättigten Festkörperlösung) geht einher mit der Verdrängung (Segregation) von Al in die Bereiche rund um die wachsenden t-ZrO_2-Partikel (Stufe III). Demzufolge werden die wachsenden t-ZrO_2 Kristallite von einer zunehmend mit Al angereicherten und an Zr und O verarmten Legierungsmatrix umgeben, welche das weitere Wachstum der t-ZrO_2 Kristallite behindert. Einzelne Ausbuchtungen der t-ZrO_2 Kristallite wachsen bevorzugt in sauerstoffreichere Regionen der Legierungsmatrix hinein; folglich kommt es zu einer Destabilisierung der Wachstumsfront. Dies führt zu der Ausbildung einer dendritischen Morphologie verursacht durch lokale Konzentrationsschwankungen des gelösten Sauerstoffs. Schlussendlich stoßen die wachsenden t-ZrO_2 Kristallite aneinander und bilden eine kontinuierliche Schicht unter der anfänglich gebildeten amorphen (Al,Zr)-Oxidschicht aus, welche aus dendritförmigen t-ZrO_2 Kristalliten umgeben von einer Al-reichen Legierungsmatrix besteht (siehe Abbildung 7.3).

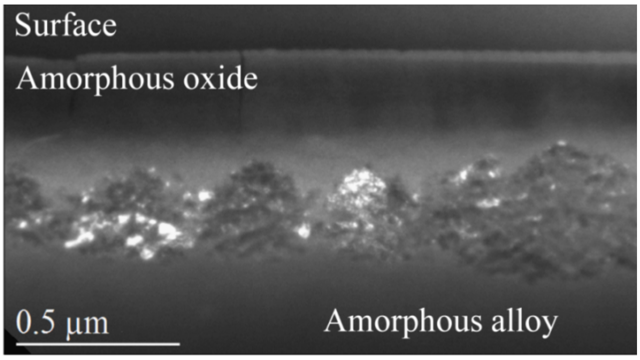

Abbildung 7.3: Dunkelfeld-TEM-Bild eines Querschnitts der am-$Al_{0.44}Zr_{0.56}$-Probe, welche bei 560 °C ($p_{O2} = 1\times10^5$ Pa) für 180 Minuten oxidiert wurde.

Die Untersuchung der Korrosionsbeständigkeit von unbehandelten und oxidierten am-$Al_{1-x}Zr_x$-Legierungen (x = 0.25, 0.32, 0.49, 0.65, 0.74) mittels elektrochemischer Mikrokapillartechnik zeigte eine ausgezeichnete Korrosionsbeständigkeit der oxidierten am-$Al_{1-x}Zr_x$ Legierungen **(Kapitel 5)**. Für unbehandelte am-$Al_{1-x}Zr_x$-Legierungen, welche anfänglich eine sehr dünne natürliche Oxidschicht aufweisen, wird ein minimaler (kritischer) Zr-Gehalt von x = 0.49 für die Bildung einer schützenden Passivschicht in 1 M HCl benötigt. Ist der Zr-Gehalt in den unbehandelten am-$Al_{1-x}Zr_x$-Legierungen $x < 0.49$, führt die Anodisierung in 1 M HCl rasch zu einem vollständigen Verlust des schützenden Charakters der Al-reichen natürlichen Oxidschicht. Mit zunehmendem Zr-Legierungsgehalt setzt ein passives Korrosionsverhalten, gekennzeichnet durch Stromdichten unter 10^0 µA/cm^2 (bei 200 mV über dem Ruhepotential (OCP)), ein und ist am besten für reines kristallines Zr. Der Passivfilm, der sich auf Zr-reichen am-$Al_{1-x}Zr_x$ Legierungen ausbildet, hat ein Al^{ox}/Zr^{ox} Verhältnis ähnlich dem der Ausgangslegierung. Für am-$Al_{1-x}Zr_x$ Legierungen mit $x \geq 0.49$ erreicht die Passivstromdichte bei einem angelegten Potential von 500 mV einen nahezu konstanten Wert von 2×10^1 µA/cm^2, unabhängig von der Legierungszusammensetzung. Diese Passivstromdichte ist vergleichbar mit der von rostfreiem Stahl und von sputterabgeschiedenen reinen kristallinen Zr-Schichten.

Die oxidierten am-$Al_{1-x}Zr_x$-Legierungen besitzen eine hervorragende Korrosionsbeständigkeit in 1 M HCl im Vergleich zu den unbehandelten am-$Al_{1-x}Zr_x$ Legierungen (siehe Abbildung 7.4a). Die oxidierten am-$Al_{1-x}Zr_x$-Legierungen weisen sehr niedrige Passivstromdichten mit Minimalwerten bis zu 3.5×10^{-2} µA/cm^2 bei Anodisierung bis zu 1000 mV auf (ohne jegliche Anzeichen für beginnende

Lochfraßkorrosion). Für ausreichend lange Oxidationszeiten wird die Passivstromdichte unabhängig von der Dicke der am-$(Al_{0.33}Zr_{0.67})O_{1.83}$-Schicht. Dies wird einer minimalen Anzahl an verbleibenden Wachstumsdefekten an der Oberfläche des Oxidfilms zugeschrieben (siehe Abbildung 7.4b).

Die chemische Stabilität und die ausgezeichnete Schutzwirkung der thermisch gewachsenen am-$(Al_{0.33}Zr_{0.67})O_{1.83}$-Schicht sind somit (*i*) dem relativ hohen nominellen Zr-Gehalt im oberflächennahen Bereich der Oxidschicht, (*ii*) der chemischen und strukturellen Homogenität der am-$(Al_{0.33}Zr_{0.67})O_{1.83}$-Schicht und (*iii*) einer minimalen Anzahl an verbleibenden Wachstumsdefekten (im oberflächennahen Bereich der Oxidschicht), verursacht durch eine ausreichend lange Oxidationszeit (t >150 Minuten bei 350 °C), zuzuschreiben. Die kontrollierte Oxidation von sputterabgeschiedenen amorphen Al_xZr_{1-x}-Schichten ist somit eine vielversprechende Möglichkeit für die Entwicklung einer neuen Generation von korrosionsbeständigen Beschichtungen auf Basis amorpher Legierungen.

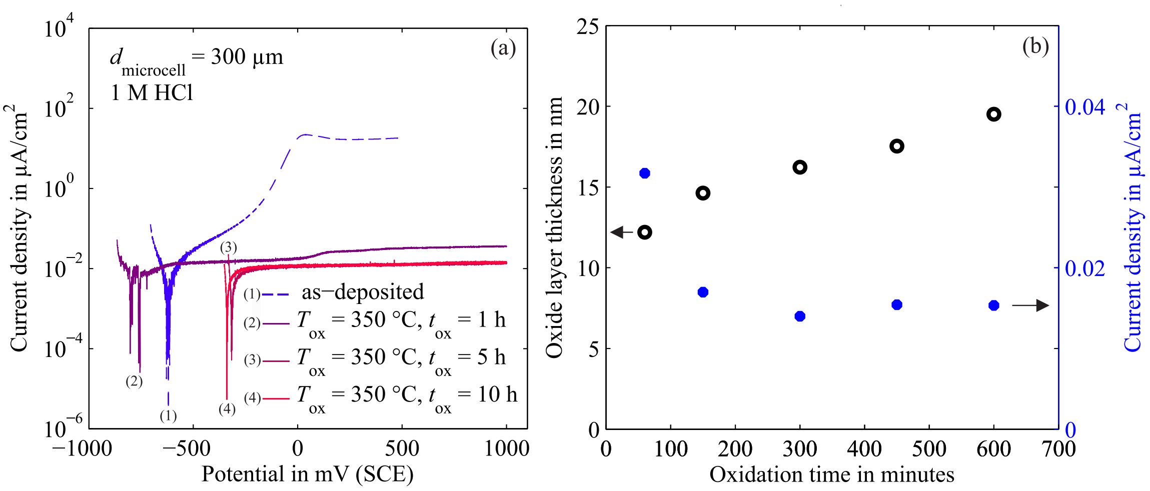

Abbildung 7.4: **(a)** Potentiodynamische Polarisationskurven von oxidierten am-$Al_{0.51}Zr_{0.49}$-Legierungen, welche durch Oxidation bei 350 °C und bei verschiedenen Oxidationszeiten (1 h, 5 h und 10 h) hergestellt wurden. Die potentiodynamische Polarisationskurve der unbehandelten am-$Al_{0.51}Zr_{0.49}$-Legierung ist zum Vergleich gegeben. **(b)** Die Schichtdicke der thermisch gewachsenen am-$(Al_{0.33}Zr_{0.67})O_{1.83}$-Phase (gebildet bei 350 °C) und die zugehörige (durchschnittliche) Stromdichte bei einem angelegten Potential von 990 – 1000 mV in der passiven Region, jeweils als Funktion der Oxidationszeit.

List of Publications

1. K. Weller, Z. Wang, L.P.H. Jeurgens and E.J. Mittemeijer: Thermodynamics controls amorphous oxide formation: Exclusive formation of a stoichiometric amorphous $(Al_{0.33}Zr_{0.67})O_{1.83}$ phase upon thermal oxidation of Al-Zr. *Acta Materialia* **94** (2015) 134-142. Chapter 2 of this thesis.

2. K. Weller, Z. Wang, L.P.H. Jeurgens and E.J. Mittemeijer: Oxidation kinetics of amorphous Al_xZr_{1-x} alloys. *Acta Materialia* **103** (2016) 311-321. Chapter 3 of this thesis.

3. K. Weller, L.P.H. Jeurgens, Z.M. Wang and E.J. Mittemeijer: Thermal oxidation of amorphous $Al_{0.44}Zr_{0.56}$ alloys. *Acta Materialia* **87** (2015) 187-200. Chapter 4 of this thesis.

4. K. Weller, T. Suter, Z. Wang, L.P.H. Jeurgens and E.J. Mittemeijer: The effect of pre-oxidation treatment on the corrosion behavior of amorphous $Al_{1-x}Zr_x$ solid-solution alloys. *Electrochimica Acta **188** (2016) 31-39.* Chapter 5 of this thesis.

5. K. Weller, N. Zotov, Z.M. Wang, L.P.H. Jeurgens and E.J. Mittemeijer: Atomic structure, electronic structure and thermal stability of amorphous Al_xZr_{1-x} ($0.26 \leq x \leq 0.75$). *Journal of Non-Crystalline Solids* **427** (2015) 104-113.

Danksagung

Die vorliegende Arbeit wurde am Max-Planck-Institut für Intelligente Systeme (ehemals Max-Planck-Institut für Metallforschung) und dem Institut für Materialwissenschaft der Universität Stuttgart angefertigt. An dieser Stelle möchte ich mich bei allen Personen bedanken, die zum Gelingen dieser Arbeit beigetragen haben.

An erster Stelle möchte ich mich bei meinem Doktorvater Herrn Prof. Dr. Ir. E. J. Mittemeijer bedanken, der es mir ermöglichte, dieses interessante Thema in seiner Abteilung zu bearbeiten. Sein stetiges Interesse an meiner Arbeit und die regelmäßigen fachlichen Diskussionen waren von sehr großer Bedeutung für den Erfolg dieser Arbeit.

Herrn Prof. Dr. J. Bill danke ich für die freundliche Übernahme des Mitberichts und Herrn Prof. Dr. T. Schleid danke ich für die Übernahme des Prüfungsvorsitzes.

Ein besonderer Dank gilt meinen täglichen Betreuern Dr. Lars Jeurgens und Dr. Zumin Wang für ihre außerordentlich gute Betreuung, die ständige Bereitschaft für wissenschaftliche Diskussionen und ihre unerschöpfliche Begeisterung für die Wissenschaft. Ihre Ideen und Anregungen haben maßgeblich zum Erfolg dieser Arbeit beigetragen.

Insbesondere möchte ich mich bei Herrn Dr. T. Suter aus der Arbeitsgruppe von Herrn Dr. L. Jeurgens an der EMPA für die Betreuung im Bereich der Elektrochemie (Kapitel 5) bedanken.

Ein großes Dankeschön auch an meine Kollegen des Max-Planck-Instituts, im Besonderen der Abteilung Mittemeijer, für die angenehme Arbeitsatmosphäre und für die Unterstützung während des gesamten Zeitraums dieser Arbeit. Besonders bedanken möchte ich mich bei Dieter Lang, Ute Salzberger, Michaela Wieland, Bernhard Siegle, Ewald Bischoff, Reinhart Völker und Frank Thiele für die experimentelle Unterstützung.

Herzlichst danken möchte ich auch meinen Freunden, sowie (ehemaligen) Doktorandenkollegen, insbesondere Bastian, Martin, Silke und Michaela, die mir immer mit Rat und Tat zur Seite standen (und stehen) und mich motiviert haben.

Der größte Dank geht an meine Eltern, meine Brüder und Bernd, für den stetigen Rückhalt, die mentale Unterstützung und den Zuspruch, den sie mir geben. Danke, dass Ihr immer für mich da seid!

Curriculum Vitae

Persönliche Angaben

Name	Katharina Weller
geboren am	08. April 1985 in Backnang
Staatsangehörigkeit	deutsch

Schulbildung

1991 – 1995	Grundschule, Althütte
1995 – 2004	Bildungszentrum Weissacher Tal, mit dem Abschluss der allgemeinen Hochschulreife

Hochschulbildung

2004 – 2011	Studium der Werkstoffwissenschaft an der Universität Stuttgart mit dem Abschluss Diplom-Ingenieur. Diplomarbeit über das Thema „Crystallization of amorphous layers on Mg-B basis“ bei Prof. Dr. Ir. E. J. Mittemeijer am Institut für Materialwissenschaft der Universität Stuttgart

Promotion

2011 – 2015	Promotion am Max-Planck-Institut für Intelligente Systeme (ehemals Max-Planck-Institut für Metallforschung), Stuttgart, und Institut für Materialwissenschaft der Universität Stuttgart. Thema der Dissertation: „Thermodynamics and kinetics of the oxidation of amorphous Al-Zr alloys“ in der Abteilung von Prof. Dr. Ir. E. J. Mittemeijer

Erklärung über die Eigenständigkeit der Dissertation

Hiermit versichere ich, dass ich die vorliegende Arbeit selbstständig verfasst und keine anderen als die angegebenen Quellen und Hilfsmittel benutzt habe; aus fremden Quellen entnommene Passagen und Gedanken sind als solche kenntlich gemacht.

Name: ____________________________

Unterschrift: ____________________________

Datum: ____________________________